AN EXPERIMENTAL STUDY OF DRYING IN POROUS MEDIA IN NOVEL 2D MICROMODELS WITH DUAL POROSITY

by

Md Ahsan Habib

A thesis submitted in partial fulfillment
of the requirements for the degree

of

Master of Science

in

Mechanical Engineering

MONTANA STATE UNIVERSITY
Bozeman, Montana

January 2024

©COPYRIGHT

by

Md Ahsan Habib

2024

All Rights Reserved

ACKNOWLEDGEMENTS

I would like to express my gratitude to my advisor Dr. Yaofa Li for the invaluable guidance and support provided throughout my study at Montana State University, without which the completion of this work would not have been feasible.

I would like to extend my sincere appreciation to Dr. Erick Johnson and Dr. Sarah Morris, members of my thesis reading committee, for their diligent review of this work and the valuable advice and remarks offered.

I would like to thank Mr. Diego Armstrong for helping me with the fabrication and machining parts. I extend special thanks to my colleagues in the Microfluidics Lab for Energy and Fluid Transport (M-LEFT), Mr. Razin Sazzad Molla, Mr. Rafid Musabbir Rahman, Ms. Arpan Ghimire Bohara, Mr. Zeeshan Ahmad Khan, Mr. Nishagar Raventhiran, Mr. Mahedi Hassan, Mr. Garrett Kennedy, Ms. Deanna Reynolds, Ms. Irais Guymon and Mr. Carson Kocmick, for their collaborative efforts, insightful ideas, and assistance in establishing the experimental apparatus.

Furthermore, I express gratitude to the Montana Microfabrication Facility (MMF) and its esteemed staff members, Dr. Andrew Lingley, Dr. Joshua Heinemann, and undergraduate lab assistants, for their indispensable assistance in the fabrication of my samples. I would like to express my gratitude to NSF Grant ECCS-1542210, and the Murdock Charitable Trust. I also thank NSF Career (2144802) for partial support in this work.

Finally, I convey my heartfelt thanks to my family and friends for their unwavering support throughout this academic journey.

TABLE OF CONTENTS

1. CHAPTER 1 INTRODUCTION 1

Motivation 1
Objectives 9
Outline 11

2. CHAPTER 2 BACKGROUND AND LITERATURE REVIEW 12

Definitions and Theoretical Background 12
Porous Medium 12
Multiphase Flow in Porous Meida 12
Porosity 12
Saturation 13
Interfacial Tension 14
Contact Angle and Wettability 15
Capillary Pressure 16
Drainage and Imbibition 17
Permeability and Darcy's Equation 18
Literature Review 19
Drying in Porous Media 19
Micromodel 29
Imaging Techniques 31

3. CHAPTER 3 EXPERIMENTAL METHOD 36

Micromodel Design 36
Micromodel Fabrication 41
Experimental Setup and Procedure 46
Experimental Procedure 54
Image Acquisition and Processing 56

4. CHAPTER 4 DRYING OF POROUS MEDIA DRIVEN BY DIFFUSION 59

Drying in Porous Media for Case 1 60
Drying in Porous Media for Case 2 67

5. CHAPTER 5 FLOW-THROUGH DRYING IN HETEROGENEOUS POROUS STRUCTURE WITH DUAL POROSITY 77

TABLE OF CONTENTS – CONTINUED

6. CONCLUSIONS AND FUTURE WORK 87

Conclusions 87
Future Work Outline 88

REFERENCES CITED 89

APPENDIX: Essential Codes 101

LIST OF TABLES

Table Page

2.1 Contact angles and corresponding wettability 16

3.1 Porosity of the micromodels in Figure 3.2 37

LIST OF FIGURES

Figure Page

1.1 Applications of multiphase flow and drying in porous media. (a) Enhanced Oil Recovery(EOR) injecting CO_2 and water; (b) Illustration and schematic of the anatomy of the liver with liver lobules and other main components, reproduced from Ref. [81]; (c) Nutrient transport and the formation in soils, reproduced from Ref. [29]; (d) Schematic representation moisture movement in the porous spaces of food cells during the drying process in fruits and vegetables.; (e) Schematic illustration of tetracycline removal using porous carbon with textile wastes via calcium acetate template, reproduced from Ref. [41]; (f) Schematic representation of CO_2 sequestrations from its major sources; (g) Schematic illustration of Gas Diffusion Layer (GDL) with microporous layer in fuel cell; (h) Schematic representation of membrane distillation with a porous membrane, reproduced from Ref. [118]. 2

1.2 Conceptual illustration depicting isolated micro- and macroaggregates under dry (left) and wet (right) conditions. Wet conditions facilitate dispersal of nutrients, microorganisms, viruses, and metabolites. Figure was reproduced based on work in Ref. [124] 3

1.3 A conceptual picture of drying from porous media [121]. 4

1.4 An example micromodel used for porous medium flow studies. 7

1.5 Typical etching profiles for wet etching (glass, left) and dry etching (silicon, right). 8

2.1 Schematic cross-section of a porous medium with different pore types. (a) closed pores, (b)(c)(d)(e)(f) open pores, (b) and (f) blind /dead-end pores/ saccate pores, (g) surface pores, (c) through pores. Figure was reproduced based on work in Ref. [94] 13

2.2 Schematic of contact angle depending on the wettability of a liquid on a solid surface. Figure was reproduced based on work in Ref. [11] 15

LIST OF FIGURES – CONTINUED

Figure Page

2.3 Illustration of non-wetting phase advancing through throats in the pore structure as capillary pressure increases, leading to a decrease in interface curvature. Figure was reproduced based on work in Ref. [11]..... 18

2.4 (a) Schematic of evaporation curve and stages of evaporation. Figure was reproduced based on work in Ref. [50]. (b) Actual three periods or stages of evaporative drying in the Relative Drying Rate - Saturation curve of drying of a single square capillary tube saturated with heptane. Solid Black line in the figure was achieved by applying a polynomial curve fitting of the actual data(red circular points). Figure was reproduced based on work in Ref. [17]..... 22

2.5 (a) Illustration of corner liquid films for square capillary tube at the tube entrance, with the camera aligned along the tube's diagonal axis [indicated by a dashed line in (b)] (b) Sketch of the cross-sectional view of the tube in the corner film region. Here, r_0 represents the curvature radius of the rounded corner, R denotes the in-plane curvature radius of corner menisci, and w is the thickness of the corner film (c) Computed representation of the shape of the gas-liquid interface within the tube. Figure was reproduced based on work in Ref. [17]..... 23

2.6 Transformation of bulk meniscus position (z_o) over time (t). The thick solid line and dashed line represent data from the square tube, while the thin solid line and dashed line at the bottom correspond to a circular tube. Inset plot shows z_o evolution over $\sqrt{t}$ in the square tube with heptane. The position of corner liquid film detachment from the tube entrance (depinning) is marked. Notably, depinning does not occur simultaneously in all four corners during the 2-propanol experiment. The two dashed lines indicate the initial depinning and the point when depinning has occurred in all four corners, respectively. Figure was reproduced based on work in Ref. [17]..... 25

LIST OF FIGURES – CONTINUED

Figure Page

2.7 Illustration of the jump of the liquid meniscus from the surface, leading to the formation of the secondary drying front (vaporization plane) at the end of CRP. (a) Detachment of the liquid meniscus from the surface and its pinning to a level below during the transition from CRP to RFP. (b) Formation of the secondary drying front leading to diffusion-controlled drying. Figure was reproduced based on work in Ref. [103]. 26

2.8 SEM images of (a) Wet etched glass micromodel channel bonded at room temperature having curved walls (Figure was reproduced based on work in Ref. [53]), (b) Silicon micromoel channel dry etched with Oxford ICP Showing the high quality, smoothness and verticality of the etch (Figure was reproduced based on work in Ref. [25]). 32

3.1 Schemactic structure of three layer glass-silicon-glass micromodel. 36

3.2 Illustration of (a) 2D photo-mask pattern of Case 1 and Case 2 micromodels with inlet and outlet on the opposite side of the porous region. The porous region is replaced with b and c to make distinct micromodel patterns for Case 1 and Case 2 respectively; (b) Porous region of photo-mask pattern for homogeneous micromodel with circles of 200 μm diameter. This design is marked as 'Case 1' ; (c) Photo-mask pattern for dual-porosity micromodel having smaller 40 μm circle sets in the middle of larger 200 μm circles. The pattern in c is named 'Case 2'; (d) and (e) are the SolidWorks designs with the required dimensions of photo-mask porous region patterns in b and c respectively. All the dimensions in d and e are in μm. 38

3.3 Pore size distribution and corresponding pores for different micromodel patterns; (a) and (c) are Pore size distributions for Case 1 and Case 2 respectively, where the number of the pores shown with the pore diameter (μm); (b) and (d) are corresponding pores for Case 1 and Case 2 respectively. 39

LIST OF FIGURES – CONTINUED

Figure Page

3.4 (a) 2D photo-mask pattern of the heterogeneous microcro-model (Case 3) with inlet and outlet. The circular cutout is the zoomed portion of the heterogeneous photo-mask showing the micro and macro pores; (b) Porous region of Case 3 micromodel photo-mask with the dimensions of the whole porous region; (c) Pore size distribution of Case 3 micromodel, where the number of the pores shown with the pore diameter in micro-meter. 40

3.5 Image of the wafer after dry etch. The transparency of the micromodel can be noticed because of the thorough etching of silicon. 43

3.6 Isometric view of the customized nanoport used to flow the fluid through the channel. It was customized to fit within smaller focal length of the higher magnification objective without blocking the view of the whole porous region. 44

3.7 Actual images of (a) Case 3 (heterogeneous and dual-porosity) micromodel sample without the attached nanoports; (b) Micromodel fabricated with the pattern mentioned in Figure 3.2 without attached nanoports. 45

3.8 SEM image of the Case 3 heterogeneous micromodel sample showing the smaller and larger pores. 46

LIST OF FIGURES – CONTINUED

Figure Page

3.9 Schematic of the step-by-step procedure to fabricate three layers of glass-silicon-glass microfluidic device. Here different colors are defined for different materials at the bottom. (a) Anodically bond of 4-inch glass and 4-inch silicon wafers; (b) Reduction of silicon wafer thickness with KOH wet etching; (c) Spin coating of photoresist over the silicon wafer as one of the steps of photolithography; (e) UV exposing with the photomask to print the pattern on the silicon wafer; (e) Development of the photomask pattern on the silicon wafer with developer solution; (f) Dry etching of silicon to make channels and pores in the silicon wafer. Etching needs to continue to make the thorough etching of the silicon; (g) Drilling through holes with drill machine on the designated places to make the inlet and outlets; (h) Cleaning of the bonded wafers and another new glass wafer with Piranha solution to remove residue photoresist and other organic products. This step also transforms the silicon from hydrophobic to hydrophilic; (i) 2^{nd} anodic bonding to blend previously bonded glass-silicon wafer with another glass wafer to form glass-silicon-glass three-layer structure; (j) Attachment of nanoports at the inlet and outlet to connect the delivery lines firmly and provide flow through the micromodel. 47

3.10 Schematic of the experimental setup for dual-magnification imaging. 48

3.11 Actual image of the experimental setup with dual-magnification imaging capability. 49

3.12 Optical setup for dual-magnification imaging applying epi-fluorescence microscopy and imaging technique. 50

3.13 Isometric view of the custom-designed bottom mount to attach the top microscope and other parts with the bottom microscope with dimensions in mm..... 51

3.14 Top view of the custom-designed bottom mount to attach the top microscope and other parts with the bottom microscope with dimensions in mm..... 51

LIST OF FIGURES – CONTINUED

Figure Page

3.15 Isometric view of the custom-designed intermediate plate mount to attach the top microscope and other parts with the bottom mount (Figure 3.13) microscope with dimensions in mm. 52

3.16 Top view of the custom-designed intermediate plate mount to attach the top microscope and other parts with the bottom mount (Figure 3.13) microscope with dimensions in mm. 53

3.17 Isometric view of the custom-designed top mount to hold the top microscope and connect it with the translation stages and other bottom parts with the dimensions in mm. 54

3.18 Top view of the custom-designed top mount to hold the top microscope and connect it with the translation stages and other bottom parts with the dimensions in mm. 55

3.19 (a) A raw image captured with the lower magnification camera; (b) Processed segmented image of the image captured with the lower magnification camera. Blue, white, and grey in the figure correspond to the water, air, and solid grains, respectively. 57

4.1 Saturation Distribution during drying of Case 1 homogeneous micromodel at (a) $t = 0$ min; (b) $t = 33.33$ min; (c) $t = 56.67$ min; (d) $t = 67.33$ min ; (e) $t = 88.0$ min; (f) $t = 95.83$ min. Blue, white, and grey in the figure correspond to the water, air, and grain respectively. 60

4.2 (Continued from Figure 4.1) Saturation Distribution during drying of Case 1 homogeneous micromodel at (g) $t = 117.50$ min; (h) $t = 146.50$ min; (i) $t = 155.0$ min; (j) $t = 176.67$ min; (k) $t = 185.83$ min; (l) $t = 196.0$ min. Blue, white, and grey in the figure correspond to the water, air, and grain respectively. 61

4.3 Water saturation variation over time in the drying process of Case 1 homogeneous micromodel. Time is presented in minutes on the x-axis. 63

LIST OF FIGURES – CONTINUED

Figure Page

4.4 Water drying rate variation over time in the drying process of Case 1 homogeneous micromodel. Water drying rate is presented in the unit of s^{-1} and Time is presented in minutes. 64

4.5 Water drying rate variation with relative average leading front distance in the drying process of Case 1 homogeneous micromodel. Water drying rate is presented in the unit of s^{-1} and the relative average leading front distance is measured from the top edge of the micromodel porous region..... 65

4.6 Leading or dry front location for Case 1 homogeneous micromodel during drying at (a) $t = 95.83$ min; (b) $t = 176.67$ min. The leading front boundaries are marked with red lines. Water and film layers are identified in the figure as deep black and grey respectively..... 66

4.7 Saturation Distribution during drying of Case 2 dual-porosity micromodel at (a) $t = 0$ min; (b) $t = 16.40$ min; (c) $t = 33.33$ min; (d) $t = 73.20$ min ; (e) $t = 105.93$ min; (f) $t = 117.20$ min. Blue, white, and grey in the figure correspond to the water, air, and grain respectively. 68

4.8 (Continued from Figure 4.1) Saturation Distribution during drying of Case 2 dual-porosity micromodel at (g) $t = 128.47$ min; (h) $t = 149.50$ min; (i) $t = 153.53$ min; (j) $t = 166.83$ min; (k) $t = 227.20$ min; (l) $t = 280.27$ min. Blue, white, and grey in the figure correspond to the water, air, and grain respectively..... 69

4.9 Water saturation variation over time in the drying process of Case 2 dual-porosity micromodel. Time is presented in minutes on the x-axis. 70

4.10 Water drying rate variation over time in the drying process of Case 2 dual-porosity micromodel. Water drying rate is presented in the unit of s^{-1} and Time is presented in minutes. 71

4.11 Water drying rate variation with relative average leading front distance in the drying process of Case 2 dual-porosity micromodel. Water drying rate is presented in the unit of s^{-1} and the relative average leading front distance is measured from the top edge of the micromodel porous region..... 72

LIST OF FIGURES – CONTINUED

Figure Page

4.12 Drying front location for Case 2 micromodel during drying at (a) t = 73.20 min; (b) t = 117.20 min; (c) t = 166.83 min; (d) t = 183.33 min. The leading front boundaries are marked with red lines. Water and film layers are identified in the figure as deep black and grey respectively. 73

4.13 Water saturation variation for whole micromodel, micropores, and macropores with time during the drying process of Case 2 dual-porosity micromodel. Time is presented in minutes on the x-axis. Blue, green, and red lines in the plot correspond to water in whole porous region, micropores, and macropores respectively. 74

4.14 Water drying rate variation for the entire micromodel, micropores, and macropores with time during the drying process of Case 2 dual-porosity micromodel. Water drying rate is presented in the unit of s^{-1} and time is presented in minutes. Blue, green, and red lines in the plot correspond to water in the whole porous region, micropores, and macropores respectively. 75

4.15 Velocity field obtained with PIV illustrating the capillary pumping effect from macropores to micropores, and the continuous water supply to the drying front. Here the FOV is 0.96 mm×0.7 mm, and the velocity scale is in μm/s. 76

5.1 Saturation Distribution during drying of Case 3 heterogeneous dual-porosity micromodel at (a) t = 0 min; (b) t = 3.58 min; (c) t = 8.20 min; (d) t = 11.50 min. Blue, white, and grey in the figure correspond to the water, air, and grain respectively. 79

5.2 (Continued from Figure 5.1) Saturation Distribution during drying of Case 3 heterogeneous dual-porosity micromodel at (e) t = 12.28 min; (f) t = 18.41 min; (g) t = 26.33 min; (h) t = 44.06 min. Blue, white, and grey in the figure correspond to the water, air, and grain respectively. 80

LIST OF FIGURES – CONTINUED

Figure Page

5.3 Water saturation variation over time in the drying process of Case 3 heterogeneous dual-porosity micromodel. Time is presented in minutes on the x-axis..... 81

5.4 Water displacement rate variation over time in the drying process of Case 3 heterogeneous dual-porosity micromodel. Water displacement rate is presented in the unit of s^{-1} and Time is presented in minutes. 82

5.5 Water depletion rate variation with interfacial length during the drying in Case 3 micromodel. Water displacement rate is presented in the unit of s^{-1} and interfacial length is presented in pixels. 83

5.6 Water saturation variation for whole micromodel, micropores, and macropores with time during the drying process of Case 3 heterogeneous dual-porosity micromodel. Time is presented in minutes on the x-axis. Blue, green, and red lines in the plot correspond to water in whole porous region, micropores, and macropores respectively. 84

5.7 Water displacement rate variation for whole micromodel, micropores, and macropores with time during the drying process of Case 3 heterogeneous dual-porosity micromodel. Water displacement rate is presented in the unit of s^{-1} and time is presented in minutes. Blue, green, and red lines in the plot correspond to water in the whole porous region, micropores, and macropores respectively. Negative displacement rate means refill in this graph. 85

5.8 Water refilling incident of micropores between the time $t =$ 12.28 min and $t = 18.41$ min. Blue, white, and grey in the figure correspond to the water, air, and grain respectively. (a) Water saturation distribution of Case 3 micromodel at $t = 12.28$ min with a red marked box; (b) and (c) Water saturation distribution for the red marked box of Figure 5.8a at $t = 12.28$ min and $t = 18.41$ min respectively. 86

ABSTRACT

Drying of porous media is pervasive in numerous natural and engineering processes, such as oil recovery, CO_2 storage, and critical zone science. Drying is essentially a multiphase flow process, where the liquid phase evaporates and is displaced/replaced by the gaseous phases, as vapor diffuses out of the porous structure. In terms of pore structure and other physical characteristics like porosity and permeability, many porous matrices exhibit multi-scale heterogeneity. For instance, in critical zone, soil is often viewed as a hierarchical organization: primary particles form aggregates, which in turn form macroaggregates, effectively leading to a dual-porosity medium. Numerous activities, including gases and water transport, are known to be controlled by the resultant multiscale flow dynamics and inter-/intra-aggregate interaction during drying. However, the fundamental physics underlying drying of porous media with dual porosity is not well understood from a fluid mechanics perspective.

In this work, a novel 2D microfluidic device fabrication technique has been developed. To study the multi-phase flow of air and water, emphasizing the multi-scale interaction, pore structure, and role of film flows, three distinct types of microfluidic devices have been fabricated, which bear the innovative three-layer glass-silicon- glass architecture, providing precise structural control and excellent optical access from both top and bottom. An innovative dual-magnification imaging technique has been introduced adapted for micro-PIV and epi-fluorescent microscopy which offers insightful information about the flow dynamics at both the micro- and macro-scales concurrently.

In this thesis, two distinct types of experiments are outlined, focusing on diffusion-driven drying and flow-through drying, utilizing three diverse micromodels characterized by varying porous structures and distributions. The experimental results have presented the overall drying dynamics observed in different micromodels, each featuring unique porous configurations. The impact of porous geometry and external flow conditions on drying rate and associated pore-scale physics is thoroughly examined. The findings encompass a comprehensive overview of micro-macro pore interactions, as evidenced by separated saturation distribution, displacement rates, and other pertinent flow parameters. The findings have reflected the influence of pore geometry, distribution, hydraulic connectivity, and film flow on the observed effects.

CHAPTER 1 INTRODUCTION

Motivation

Drying in porous media holds great significance across a wide range of natural and engineering processes. As shown in Figure 1.1, notable applications include the food processing [33, 56, 82, 91], pharmaceutical industries [72, 80, 85], porous building materials [29], soil drying, and its application in hydrological modeling [10, 57, 95] and process industries [114]. Additionally, it plays a role in the nutrient transport towards the plant roots in soil [73] and accumulation of solutes near the Earth's surface [42]. A comprehensive understanding of the underlying physics in drying phenomena can contribute to cost and energy savings. Therefore, the control of drying kinetics emerges as a pivotal factor.

For instance, industrial revolution fueled unprecedented economic growth, driven by the increasing demand for energy. Fossil fuels, such as coal, natural gas, and oil, have been the primary energy sources due to their high energy density and ease of transportation. Unfortunately, their combustion leads to irreversible carbon dioxide emissions, resulting in global warming and climate change, causing devastating effects on our environment, ecosystems, and human life. Despite the existence of renewable energy sources, challenges like intermittency and storage limit their widespread adoption. The ongoing reliance on fossil fuels demands urgent action to stabilize anthropogenic CO_2 emissions. Over 374 billion metric tonnes of CO_2 have been released since the industrial revolution, with about half occurring since the mid-1980s [39]. To mitigate the effects of carbon emission, carbon capture and storage (CCS) emerges as a crucial technology, involving injection and long-term storage of CO_2 in geological formations. During CO_2 injection, salt precipitation due to drying reduces permeability, posing a threat to sequestration by obstructing pores. This

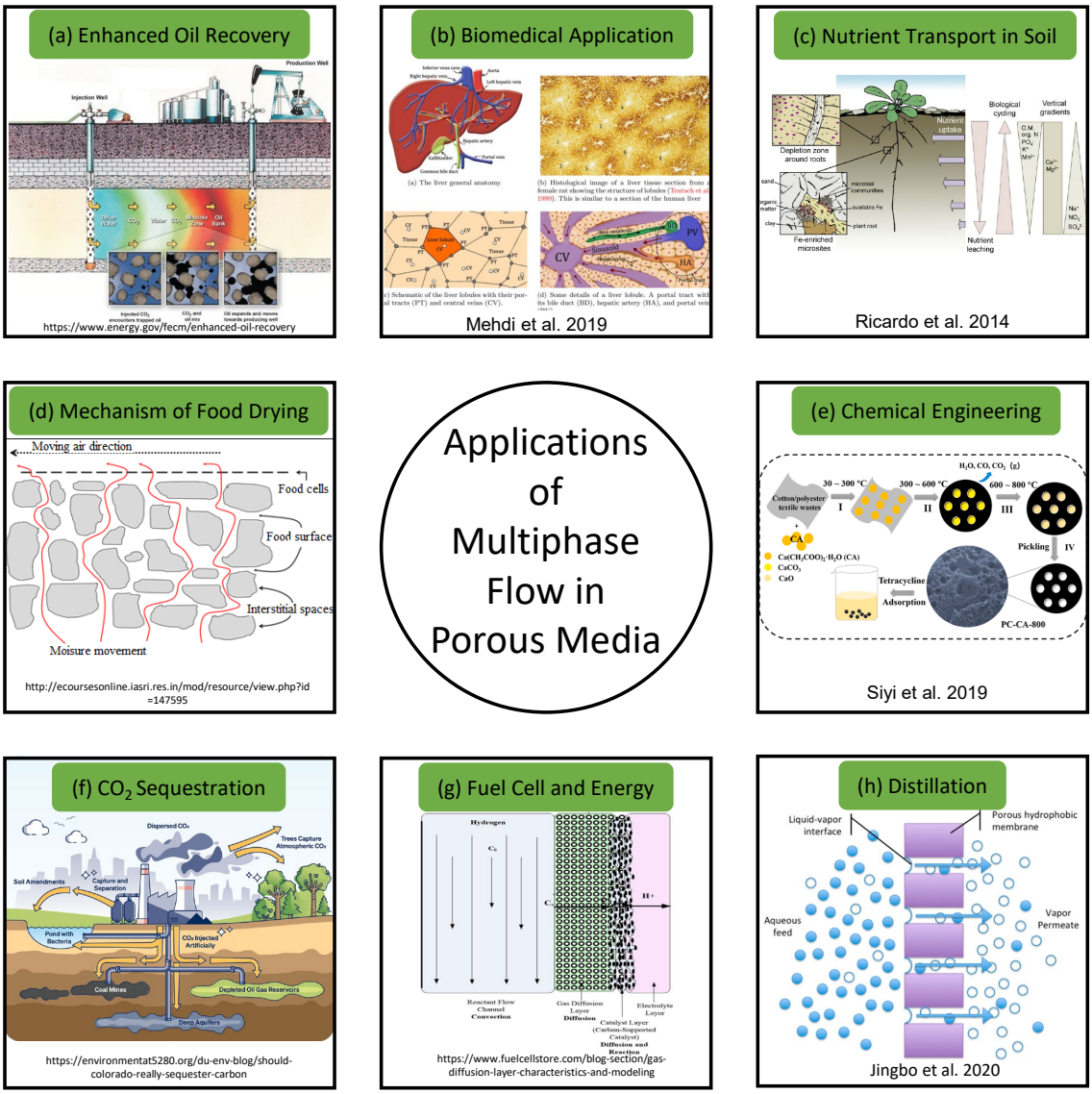


Figure 1.1: Applications of multiphase flow and drying in porous media. (a) Enhanced Oil Recovery(EOR) injecting CO_2 and water; (b) Illustration and schematic of the anatomy of the liver with liver lobules and other main components, reproduced from Ref. [81]; (c) Nutrient transport and the formation in soils, reproduced from Ref. [29]; (d) Schematic representation moisture movement in the porous spaces of food cells during the drying process in fruits and vegetables.; (e) Schematic illustration of tetracycline removal using porous carbon with textile wastes via calcium acetate template, reproduced from Ref. [41]; (f) Schematic representation of CO_2 sequestrations from its major sources; (g) Schematic illustration of Gas Diffusion Layer (GDL) with microporous layer in fuel cell; (h) Schematic representation of membrane distillation with a porous membrane, reproduced from Ref. [118].

wellbore dry-out hampers injectivity, increasing costs and reducing carbon efficiency and storage potential, impacting oil recovery. Understanding this pore-scale physics of drying is crucial for improving carbon sequestration in fractured reservoirs and geological formations.

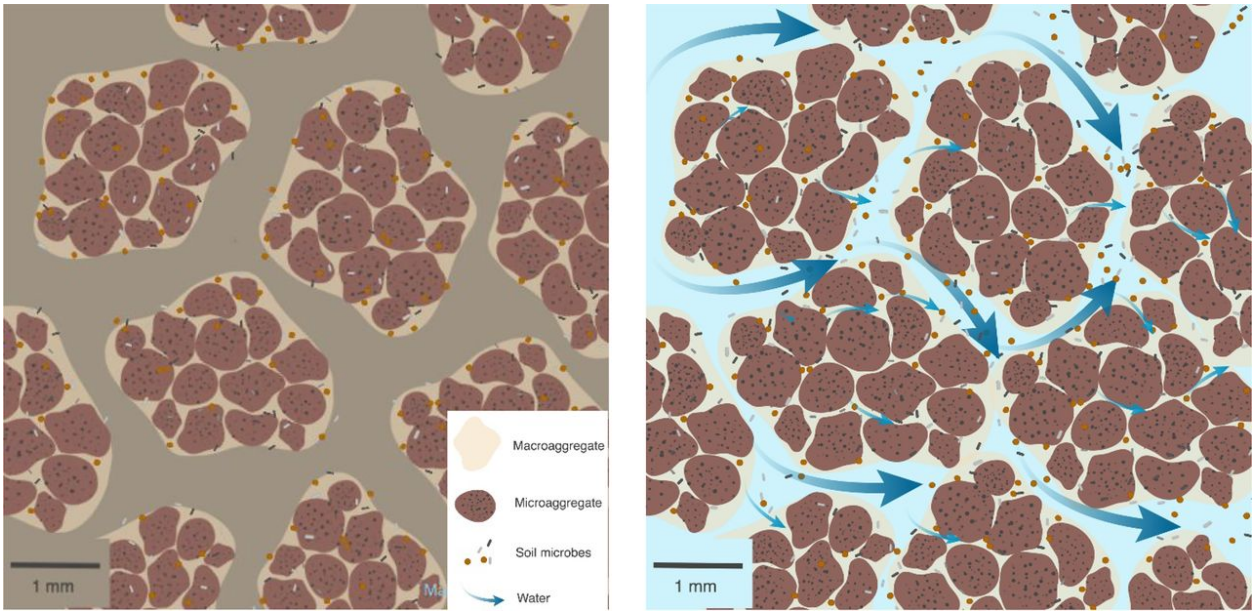


Figure 1.2: Conceptual illustration depicting isolated micro- and macroaggregates under dry (left) and wet (right) conditions. Wet conditions facilitate dispersal of nutrients, microorganisms, viruses, and metabolites. Figure was reproduced based on work in Ref. [124]

As another example, soil is an integral part of geological formation and ecosystem (Figure 1.2). The structure of soil is a crucial physical attribute that exerts a substantial impact on both the environment and agriculture. It is essential for terrestrial life, harboring microbial communities, and nutrient cycles that support the ecosystems [24]. Soils consist of structured aggregates and pore spaces, forming a three-dimensional matrix. Aggregates, including microaggregates ($<250\,\mu$m) and macroaggregates (0.25 - 2 mm), are composed of mineral particles and organic carbon held together by various forces [107]. Microaggregates, resilient to stress, persist for decades and contribute to larger macroaggregates [106]. These structures influence soil properties, including organic carbon and water content and their flow [14]. The interiors of aggregates create microenvironments with distinct properties, fostering

spatially heterogeneous niches for microorganisms. Understanding these structures and pore-scale flow dynamics is vital for comprehending soil ecology and the dynamics of terrestrial ecosystems. The presence of both microaggregates and macroaggregates of different pore sizes in the soil creates a multiscale environment referred to as dual-porosity. Numerous activities, including gases and water transport, are known to be controlled by the resultant multiscale flow dynamics and inter-/intra-aggregate interaction during drying. However, the fundamental physics underlying drying of porous media with dual porosity is not well understood from a fluid mechanics perspective.

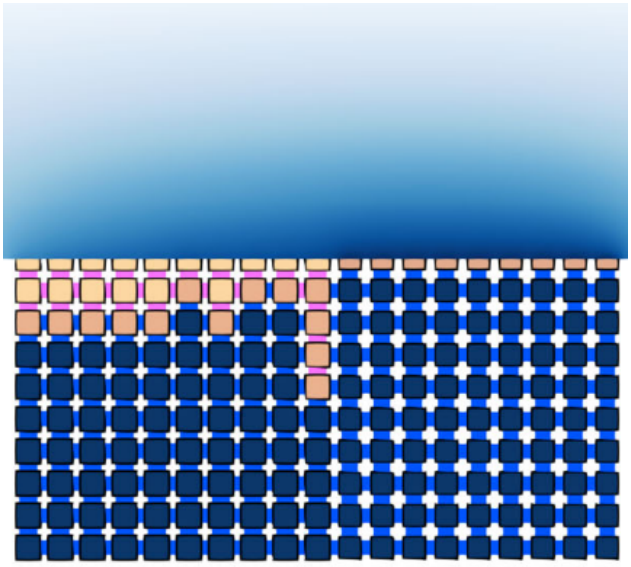


Figure 1.3: A conceptual picture of drying from porous media [121].

Drying in porous media, as in the aforementioned applications, is essentially a multiphase flow process in porous media, where the liquid phase vaporizes, causing the originally liquid-saturated pore space to be continuously displaced by the vapor phase, often referred to as the invasion-percolation process. Additionally, the evaporation at the liquid-vapor interface is governed by a series of three processes: (i) liquid supplied to the interface, (ii) liquid molecules escaping to the vapor space, and (iii) vapor molecules transported away from the interface by diffusion and/or convection. Depending on the operation conditions,

any of the three processes can be the limiting factor of evaporation. For instance, if the vapor space above the liquid-vapor interface is already quite saturated with vapor (i.e., the partial pressure of vapor is approaching the saturation pressure at the given temperature), removal of vapor from the interface (process iii) will be difficult, which will, in turn, hinder subsequent evaporation. This can be referred to as diffusion-limited or mass-limited. Alternatively, if the liquid supply is insufficient to sustain the evaporation at the interface (process i), the drying process can be also hindered.

Currently, drying in a homogeneous porous media is relatively well understood. Consider a homogeneous porous medium subject to the open atmosphere (*e.g.*, soil). Based on our current understanding, the drying process is characterized by three periods [19]: the constant-rate period (CPR), the falling-rate period (FRP), and the receding front period (RFP). During the first period (CPR), initially, the porous medium is saturated with liquid (hereafter, water) and the evaporation occurs at the top surface at a constant rate. As the top surface dries out, the porous medium becomes partially saturated. At this point, while the drying or evaporation primarily occurs at the top surface, water is continuously supplied to the surface driven by capillary effect through a network of connected pores and corner flows, effectively sustaining the evaporation at a similar level. The evaporation rate during the CRP is controlled by external environmental demands such as relative humidity, flow speed, and temperature of the air on top of the porous medium. As the drying proceeds, corner flow weakens and the water-saturated regions may become disconnected, at this point, capillary flow becomes insufficient to sustain the evaporation at the interface, leading to a transition to a second period, the FRP. The period features an imbalance between capillary pumping, the driving force, and the opposing forces such as gravity and viscous dissipation. Finally, the RFP is characterized by the existence of a fully dry region between the liquid front and the top surface of the porous medium. During this period, the evaporation takes place inside the porous medium and it is limited by the diffusion process of the vapor phase.

These drying periods and processes have been observed and demonstrated by numerous experiments and simulations [12, 17, 50, 65, 87, 90, 98, 102, 115]. Since the CRP offers high and well-controlled evaporation rate, in many engineering applications, a prolonged CRP is often desired. However, the mechanisms that govern the transition from the CRP to the FRP still remain unclear, and accurate prediction of this transition is thus challenging [116]. This challenge is likely due to some overlooked physics at the microscopic scale and a lack of quantification of the pore-scale processes such as the corner flow and liquid bridges that are crucial to sustain the hydraulic connectivity for water supply. Therefore, a thorough understanding of the fundamental flow physics at the pore scale is essential for engineering systems and predicting larger-scale phenomena. Developing micro-scale models capable of accurately representing pore-scale processes is crucial for improving the accuracy of continuum-scale predictive tools. While translating pore-scale results directly into large-scale predictions may not always be practical, the knowledge gained from pore-scale investigations enhances our ability to advance these efforts.

In addition, the drying of porous media can be further complicated by the multi-scale structures of many porous media. For instance, the soil structure as shown in Figure 1.2 features dual porosity. While the pore size in macroaggregates can be on the order of tens or hundreds of micrometers, the microscale pores in the microaggregates can be sub-micrometers. The pore size plays a crucial role in the multiphase phase in porous as it determines the capillary effect. According to the Young-Laplace equation, the capillary pressure is defined as,

$$p_c = \frac{2\gamma\cos\theta}{r} \tag{1.1}$$

where γ is the surface tension, θ is the contact angle and r is the effective radius of the pore. As a result of this well-known law, the capillary pressure is higher at smaller pores

compared to larger ones. Assuming a constant pressure in the vapor phase with negligible viscous dissipation, the pore pressure within the smaller pores ends up being lower, which draws water to flow from larger pores to smaller pores, called capillary pumping [32]. When this capillary pumping effect is coupled with drying in porous media, water in the large pores will preferentially dry first than that in the smaller pores. It is worth noting that this does not mean that evaporation only occurs at large pores initially. Instead, capillary effects keep pumping water from large pores to small pores so that small pores stay saturated until large pores are completely depleted, whereas in theory evaporation should occur at all liquid-vapor surfaces. However, such flow interaction between small and large pores is not well characterized. Specifically, how does capillary pumping quantitatively happen? What is the role of corner flows? What is the role of disconnected pores? All these questions are crucial to our understanding of drying in porous media but yet still to be answered.

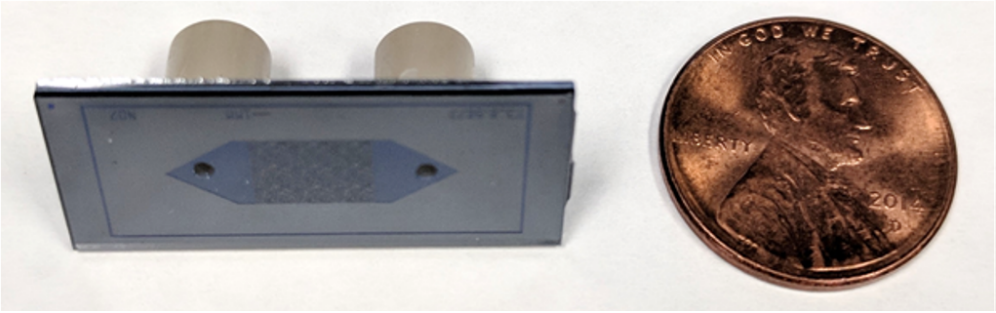


Figure 1.4: An example micromodel used for porous medium flow studies.

Moreover, characterizing the multiphase flow in dual-porosity porous media is technically challenging due to the large separation of length scales. The large pores often require large field of view (FOV) and relatively low magnification to observe, whereas the small pores require opposition (small FOV but high magnification). The imaging of both smaller and larger pores necessitates the utilization of very different optical parameters, posing a significant challenge to the imaging techniques. Essentially, an optical system that is capable

of imaging at both high and low magnifications simultaneously is needed. Another challenge is that natural porous media such as soil and the proton-exchange membranes in a fuel cell are often opaque, essentially eliminating the possibility of direct observation of the flow using any optical-based techniques, adding another layer of complexity to the problem. Nevertheless, effectively addressing these challenges is paramount for a comprehensive understanding of pore-scale physics in larger systems and the successful integration of such knowledge into broader-scale applications. The understanding of these challenges not only enriches our comprehension of micro-scale phenomena but also facilitates the seamless application of these insights to large-scale systems.

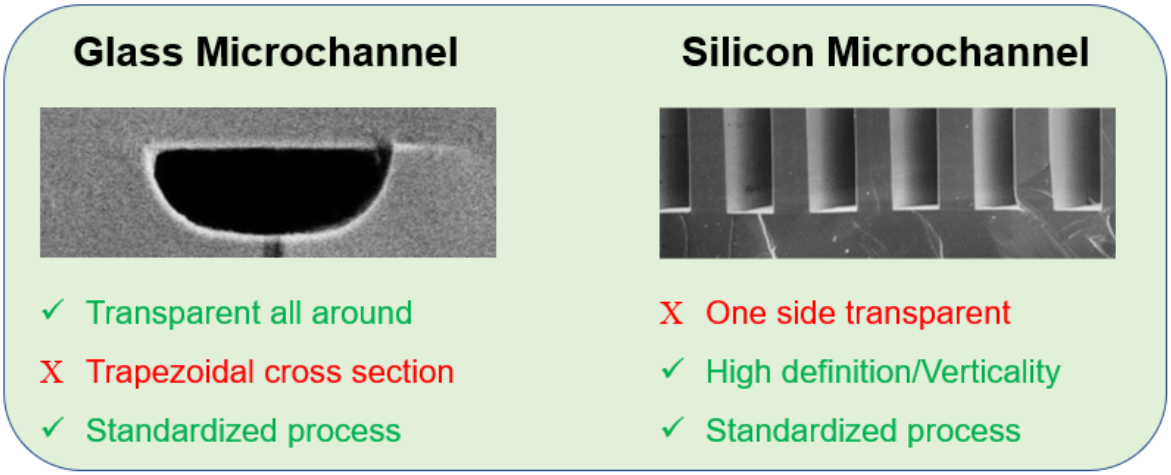


Figure 1.5: Typical etching profiles for wet etching (glass, left) and dry etching (silicon, right).

To overcome these challenges, microfluidic devices have served as a power tool. Microfluidic devices of porous media, commonly referred to as micro-models, are devices that contain fabricated model porous media inside and are transparent at least on one side to directly visualize the flow (Figure 1.4) [16, 23, 34, 36, 43, 52, 70, 79, 105, 109]. Researchers have effectively developed various micron-scale features to study and investigate the flow of fluids, particles, and solute transport phenomena. These microscale features

are designed to study a particular phenomenon by enabling them to utilize advanced imaging techniques. Conventionally, there are two common approaches to fabricating a micromodel: with glass and with silicon. The fabrication of a glass micromodel involves standard photolithography, wetting etching, and thermal-assisted bonding. While glass-based micromodels are transparent all around, thus offering excellent optical access, wetting etching is however isotropic, leading to curved and variable etching profiles as shown in Figure 1.5. The variation in the vertical direction creates strong 3D effect in the microchannels, impeding flow characterization using microscopy. On the other hand, the fabrication of a silicon-based micromodel involves standard photolithography and dry etching. Drying etching is based on the inductively coupled plasma reactive ion etching process (ICP-RIE), which is directional and capable of creating straight and vertical walls as shown in Figure 1.5. Once etched, the silicon is bonded to a glass wafer typically with an anodic bonding process to create a closed microchannel. However, although the silicon micromodel offers perfectly vertical walls and essentially 2D microchannels, a big disadvantage it is that is only transparent on one side (*i.e.*, the glass side), which significantly limits its optical access, creating challenges to current imaging techniques.

Taken together, in order to further our understanding of drying in single and dual-porosity porous media for better prediction and engineering designs, it is critical to investigate the pore-scale flow and physics using innovative approaches. To facilitate such investigations, it is desirable to develop novel micromodels that feature both vertical walls and two-sided optical access, as well as an imaging system that enables simultaneous imaging at both low and high magnifications.

Objectives

To effectively tackle the aforementioned challenges and thus answer relevant scientific questions, the following objectives are developed for this thesis:

- Develop a novel fabrication technique to create 2D dual-porosity micromodels with precise porous structures and excellent optical access for the simultaneous observation of the flow in both microscale and macroscale pores.

- Develop an innovative dual-magnification imaging system coupled with microscopic particle image velocimetry (micro-PIV) and epi-fluorescent microscopy to study the flow dynamics at both micro- and macro-scales concurrently.

- Investigate and gain insight into the pore-scale physics during drying in porous micromodels employing the aforementioned methodology.

Outline

The rest of the thesis is organized as follows:

- Chapter 2 presents essential concepts, theories, and definitions pertinent to multiphase flow in porous media. Subsequently, it provides a short literature review on micromodels, and their various types, as well as imaging techniques, and two-phase flow in porous media, with a specific focus on topics such as drying.

- Chapter 3 presents a detailed description of the experimental methodology including micromodel design and fabrication, dual-magnification imaging technique, image acquisition, experimental procedure, image processing, and data analyses.

- Chapter 4 presents the results of the overall drying behavior during convective drying in different micromodels featuring various porous structures. The effect of porous geometry on drying rate and relevant pore-scale physics are discussed.

- Chapter 5 presents the results of the overall drying behavior during flow-through drying in heterogeneous dual-porosity micromodel. The effect of porous geometry on drying rate and relevant pore-scale physics are discussed.

- Chapter 6 concludes the thesis with major conclusions and recommendations for future work.

CHAPTER 2 BACKGROUND AND LITERATURE REVIEW

Definitions and Theoretical Background

To facilitate the description and discussion in the later sections, a few important definitions and relevant theoretical background are provided in the current section.

Porous Medium

A porous medium herein is defined as a permeable solid structure characterized by interconnected pores that facilitate the flow of distinct phases (Figure 2.1) Examples of porous media include natural materials such as reservoir rocks and soil, as well as man-made materials like cement and ceramics [11]. A porous medium is often characterized by several intrinsic properties, such as porosity, connectivity, pore size distribution, and throat size distribution.

Multiphase Flow in Porous Meida

In a porous medium, the occurrence of simultaneous movement involving more than one fluid phase is referred to as multiphase flow where the phases are distinguished by visible boundaries (*i.e.*, interfaces) featuring distinct discontinuities in composition and properties. The flowing phases can be either fluids (*e.g.*, water) and/or solids (*e.g.*, solid suspensions). In the presence of more than two fluid phases, they can be miscible or immiscible, and potential fluid-fluid and fluid-solid reactions may occur. Because of the complexity of the multiphase flow, this thesis specifically focuses on the discussion of the flow of two immiscible fluid phases (*e.g.*, water and its vapor) through a rigid and nonreactive solid porous matrix.

Porosity

Porosity, denoted by the symbol ϕ, represents the fraction of the total volume of a porous medium that is occupied by void space [11]. Mathematically, it is expressed as the

ratio of the volume of void space (V_v) to the total or bulk volume (V_b) of the soil or rock. Alternatively, porosity can be determined by recognizing that the bulk volume of the porous structure consists of both void space and the space occupied by the solid structure (V_s). Thus, porosity can be defined as [8]:

$$\phi = \frac{\text{void volume}}{\text{total bulk volume}} = \frac{V_v}{V_b} = \frac{V_v}{V_s + V_v} = \frac{V_b - V_s}{V_b} \tag{2.1}$$

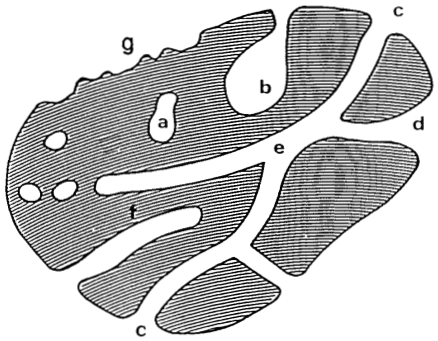


Figure 2.1: Schematic cross-section of a porous medium with different pore types. (a) closed pores, (b)(c)(d)(e)(f) open pores, (b) and (f) blind /dead-end pores/ saccate pores, (g) surface pores, (c) through pores. Figure was reproduced based on work in Ref. [94]

Figure 2.1 shows the schematic cross-section of a porous solid, illustrating different types of pores within porous media depending on their position. Porosity is classified into two types: total porosity and effective porosity [11]. Effective porosity excludes closed pores from void volume calculations in Equation 2.1, as these closed pores do not contribute to fluid flow. When there are no void pores, both effective and total porosity are equal.

Saturation

Saturation (S) is defined as the fraction or percentage of the pore volume occupied by a specific fluid or phase (*i.e.*, oil, gas, or water). This property is mathematically articulated

by the following relationship:

$$S = \frac{\text{Total volume of the fluid or phase}}{\text{Pore volume}} \tag{2.2}$$

All saturations are determined based on the pore volume rather than the gross volume of the porous medium. The saturation of each phase ranges between 0 to 1 [11]. In a two-phase system, there are two distinct phases: the wetting phase and the non-wetting phase along with the solid phase. According to the definition in Equation 2.2,

$$\sum_{\alpha=\text{w,nw}} S_\alpha = 1 \tag{2.3}$$

where 'w' and 'nw' denote wetting and nonwetting phases, respectively, for a two-phase flow system.

Interfacial Tension

In multiphase flow, phases are identified by visible boundaries, or interfaces, which exhibit noticeable discontinuities in composition and properties. At the interface of phases in multiphase flow, the interaction between molecules occurs through adhesive forces, which attract molecules of different phases to each other, and cohesive forces, which bind molecules within the same phase together. These collective interactions result in the phenomenon known as interfacial tension (γ). Interfacial tension is the manifestation of the cohesive forces within each phase contrasting with the adhesive forces between phases, creating a dynamic equilibrium at the boundary. This tension plays a crucial role in shaping the behavior of the interface and influencing the overall dynamics of multiphase systems.

Contact Angle and Wettability

Wettability refers to the affinity of a liquid for a solid surface and plays a crucial role in understanding the interaction between two phases, mostly fluid and solid. Essentially, wettability depends on the adhesive and cohesive forces of liquid and solid. The contact angle, a key parameter in wettability, is defined as the angle formed between the tangent of the liquid-vapor interface and the tangent of the solid-liquid interface where they intersect [11] (shown in Figure 2.2). It characterizes the degree of wetting or non-wetting behavior (Table 2.1).

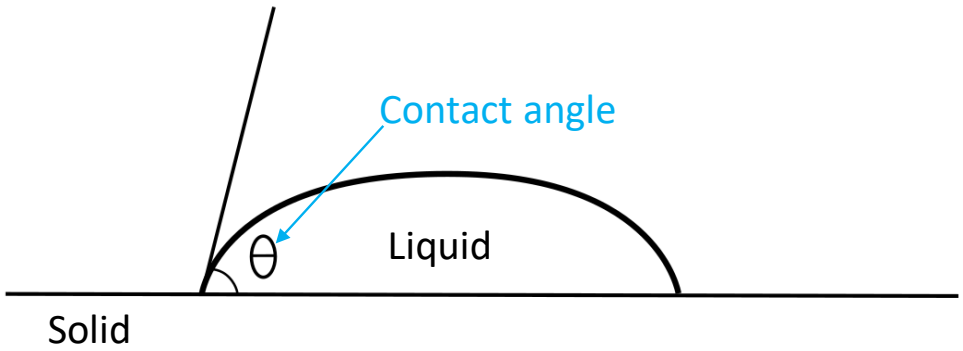


Figure 2.2: Schematic of contact angle depending on the wettability of a liquid on a solid surface. Figure was reproduced based on work in Ref. [11].

The importance of wettability and contact angle lies in their influence on various processes, such as fluid displacement in porous media, adhesion, and interfacial tension. In porous media studies, wettability impacts capillary pressure, fluid distribution, and overall flow behavior [31]. Understanding these concepts is essential in diverse fields, including oil recovery, material science, and biological applications, where surface interactions profoundly affect outcomes [11].

Real-world scenarios involve multiple fluids flowing in porous media, creating distinct interfaces between immiscible phases, resulting in a pressure difference if the interfaces are curved. The interfacial tension between these phases is measured as a force per unit length

Table 2.1: Contact angles and corresponding wettability

Contact angles	**Wettability**
$\theta = 0°$	Completely wetting liquid
$0° < \theta < 90°$	Wetting liquid
$\theta = 90°$	Neutrally wetting liquid
$90° < \theta < 180°$	Non-wetting liquid
$\theta = 180°$	Completely non-wetting liquid

or energy per unit area. At equilibrium, the contact angle (θ) indicates the wettability. For instance, when $\theta < 90°$, the fluid is wetting (water-wet), $\theta > 90°$ implies non-wetting, $\theta = 0°$ indicates complete wetting, and $\theta = 90°$ suggests neutral wettability.

In simpler terms, a strongly water-wet solid surface makes a hydrophilic fluid 'wetting,' causing it to spread over the solid surface with a small contact angle. Conversely, a hydrophobic fluid, on a water-wet surface, will have a large contact angle, indicating that it prefers not to spread over the surface, with the angle exceeding 90° .

Capillary Pressure

In the presence of multiple phases within a porous medium, each marked by interfaces between different phases, a pressure difference emerges due to the interfacial tension (γ) at these separating surfaces. The direct outcome of the presence of more than one fluid phase and interfacial tension is capillary pressure P_c. Capillary pressure is defined as the pressure difference across the interface of two immiscible phases [30].

$$P_c = P_{NW} - P_W \tag{2.4}$$

where, P_{c} represents the capillary pressure, whereas P_{NW} and P_{W} denote the pressures of

the non-wetting and wetting phases, respectively. In a real porous material, the inside of a pore has a curved interface to reduce surface energy. This curvature is defined by two main radii, r_1 and r_2, measured at right angles to each other. These radii are linked to capillary pressure and can be written as [8]:

$$P_c = \gamma(\frac{1}{r_1} + \frac{1}{r_2}) \tag{2.5}$$

Here, γ denotes the interfacial tension between the two phases. The units of γ are either force per unit length (N/m) or energy per unit area (J/m^2). This Equation 2.5 is another form of the Young-Laplace Equation. Oftentimes, defining pore size precisely for a given porous medium is challenging due to the irregular and variable shapes of pores [94]. To simplify, a cylindrical capillary tube is commonly used as a model to calculate the capillary pressure of a single pore in a porous medium. For a cylindrical tube with a radius r containing two fluids and a contact angle θ, the radius of curvature of the fluid interface is $r_1 = r_2 = r/\cos\theta$. The capillary pressure (P_c) in this case can be determined with Equation 1.1 as mentioned previously [11]:

Drainage and Imbibition

Drainage, in general, refers to the displacement of a wetting phase by a nonwetting phase [11]. During drainage, at the initial state, the non-wetting phase surrounds a wetting phase-filled porous medium. The pressure in the non-wetting phase is then gradually increased. According to the Young-Laplace equation (Equation 2.5), the non-wetting phase will initially invade the widest portions of the pore space (pore body), where the interface's radius of curvature is maximized, and subsequently fill smaller regions (pore throat) which is shown in Figure 2.3 [11].

Imbition is the inverse of the drainage process, where the wetting phase now invades the non-wetting phase. Primary imbibition refers to the invasion of a wetting phase into

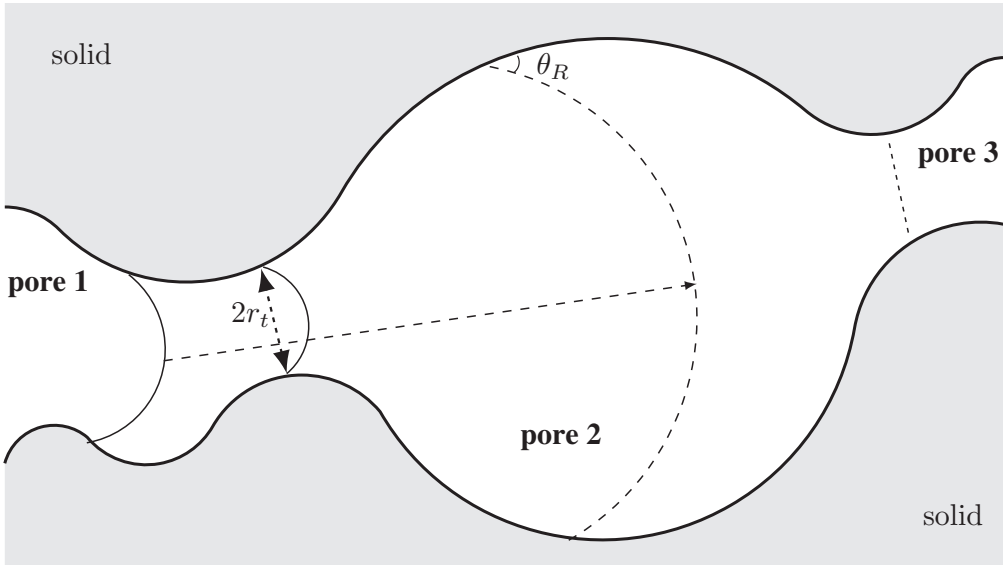


Figure 2.3: Illustration of non-wetting phase advancing through throats in the pore structure as capillary pressure increases, leading to a decrease in interface curvature. Figure was reproduced based on work in Ref. [11].

a porous medium initially fully saturated with the non-wetting phase. In contrast to the drainage process, imbibition can occur either through external forces, such as a pressure gradient or spontaneously driven by capillary forces[11].

Permeability and Darcy's Equation

Permeability, a fundamental property of porous media, is defined as the ratio of flow rate to pressure gradient within the medium, with characteristics determined by pore structure and size. It is a key parameter in scientific studies of porous media. Proposed by Henry Darcy in 1856 who established a linear relationship between the flow rate of water and the hydrostatic pressure in the phenomena of water flow in sand filters for fountains [26]. Later this relationship was used to relate flow rate (Q) to absolute permeability (κ), cross-sectional area (A), dynamic viscosity (μ), fluid density (ρ), gravitational vector (g), and pressure gradient (∇P), which can be written as[83, 125],

$$Q = -\frac{\kappa A}{\mu}(\nabla P - \rho g) \tag{2.6}$$

This law can be derived from the steady-state Stokes equation, suggesting the validity of Darcy's observation [11]. When extending Darcy's law from single-phase flow to multiphase flow, the effective permeability of the respective phase replaces the actual permeability of the porous medium. Relative permeability ($K_{r\alpha}$) becomes a dimensionless measure of the conductance of the porous medium for the fluid phase when saturated with more than one fluid, calculated as the ratio of effective permeability (K_α) to intrinsic permeability (K).

Literature Review

Drying in Porous Media

Drying is a fundamental process, in which the liquid phase undergoes a transformation into vapor at the surface or interface. Subsequently, the vapor phase is displaced and replaced by another gaseous phase that is not saturated with the evaporating substance. This natural phenomenon occurs below the boiling temperature of the liquid and is reliant on the input of latent heat energy from the surrounding environment or the atmosphere to facilitate the phase transition from liquid to vapor. Numerous factors influence the drying rate, including the temperature and humidity of the drying gas displacing the evaporating substance, the surface area of the interface or surface, and the flow rate of the drying gas [104].

The molecules of liquid phase exist closely, separated by just over one molecular diameter. At such distances, the subatomic particles constituting the molecules interact in a way that attracts them to each other, resulting in a short-range force between them. This force diminishes rapidly as the separation increases. In the vapor phase, molecules are significantly more distant than in the liquid phase, resulting in smaller intermolecular forces. The transition from liquid to vapor phase requires an increase in the separation

between molecules, necessitating a specific amount of energy. The energy required is directly proportional to the number of molecules involved. Additionally, the movement of water vapor molecules away from the evaporating water surface indicates the transfer of energy from the surface in the form of latent heat. A significant factor influencing the drying process is the temperature difference between the liquid phase and drying gas; higher temperature differences correspond to increased energy exchange rates. Additionally, the vapor pressure at the interface plays a crucial role. Freely diffusing vapor molecules result in low vapor pressure, facilitating the flow of molecules from liquid to vapor along with an equivalent flow of latent heat. In contrast, if the volume of drying gas above the liquid is sealed off, the unrestrained diffusion of liquid molecules from the surface becomes restricted due to the limiting vapor pressure [104].

The significance of understanding the drying process in porous media cannot be overstated. Its applications span a wide range, encompassing various fields, including but not limited to nutrient transport in soil and underground water [113], food industries [20, 22, 37], biomedical applications [60], chemical engineering [1, 41, 68], Pharmaceutical industries [108, 117], groundwater contamination and remediation [47, 99], wastewater treatment [13], CO_2 sequestration [49, 69, 71, 129], liquid water management in fuel cells [7, 63], extraction of materials and distillation and desalination [61, 62, 97]. In agriculture, knowledge of drying processes aids in optimizing crop drying techniques, ensuring better quality and longer shelf life. In food processing, it contributes to the development of efficient methods for drying food products, preserving their nutritional value. In material science, understanding drying in porous media is crucial for manufacturing processes involving porous materials and membranes. Furthermore, environmental studies, play a key role in comprehending water movement and evaporation in natural porous environments, influencing ecological systems. Hence, understanding and controlling the drying factors are essential in optimizing the drying process for various applications. Considerable progress has been achieved in comprehending

the drying process, particularly in porous media. Despite this, further clarity is needed for the flow dynamics, evaporation stages, and their transitions as a part of pore-scale physics.

In the study of porous media drying, two primary types of boundary conditions are commonly considered; flow-through drying and diffusion-driven drying. During flow-through drying, direct injection of gas is introduced into the porous media partially filled with wetting liquid to dry the region [3, 75]. On the other hand, during diffusive-driven drying, unsaturated gas flows across the porous media interface which dries out the porous region by vapor diffusion [86]. Example includes drying of wet soil at atmospheric conditions. The investigation of porous media drying kinetics has yielded significant progress in measuring evaporative fluxes for different kinds of porous media where different stages of drying period were observed. However, as mentioned in the previous section, the precise nature and dynamics of the transition from these stages of evaporation remain somewhat unclear.

Due to the involvement of external mass and energy transfers, coupled with various influencing factors such as temperature, humidity, surface area, capillary pressure, and the velocity of the drying gas, along with internal mass transfers encompassing vapor diffusion and the geometric characteristics of pore space, the process of drying emerges as a complex phenomenon. Consequently, the rate of evaporation from porous media finds itself typically constrained by atmospheric conditions and pore transport properties [101, 112]. Moreover, relative humidity (vapor pressure of evaporating substance) at the interface of the porous medium has a substantial influence on the evaporation rate. The dynamic interactions of these factors give rise to three distinct stages during the drying of initially saturated, wet porous media undergoing isothermal and non-isothermal drying [17, 17, 65, 87, 90, 112, 115].

During drying of a wet porous media, the initial stage of evaporation, known as CRP, has considerably high evaporation rate because of its elevated liquid saturation at the interface, as illustrated in Figure 2.4 [100]. The driving force behind this accelerated evaporation lies in the capillary pressure-driven transport of water molecules along the pore walls. This

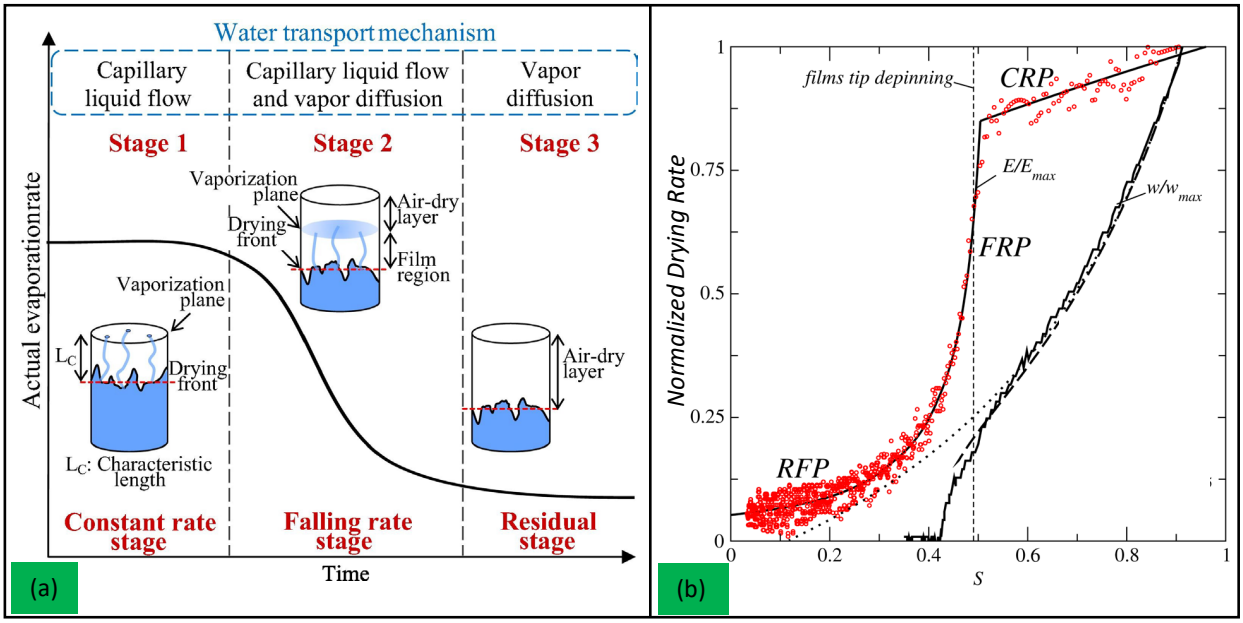


Figure 2.4: (a) Schematic of evaporation curve and stages of evaporation. Figure was reproduced based on work in Ref. [50]. (b) Actual three periods or stages of evaporative drying in the Relative Drying Rate - Saturation curve of drying of a single square capillary tube saturated with heptane. Solid Black line in the figure was achieved by applying a polynomial curve fitting of the actual data(red circular points). Figure was reproduced based on work in Ref. [17].

transport is made possible by the stronger adhesion of water molecules to the pore wall compared to the cohesive forces between water molecules. As water is transported via capillarity in the film region leading up to the interface, gas-filled pore spaces become saturated with water vapor. Consequently, evaporation can only occur on the exposed evaporating interface, leading to the drying period regulated by flow rate of the drying gas and relative humidity of the atmosphere or the surrounding drying gas [17, 18].

The main driving force sustaining CRP is capillary action, ensuring a consistent rate of evaporation. Despite the name suggesting a constant drying rate, it is more accurately described as pseudo-constant, as the drying rate exhibits a decreasing trend with the thinning of pore corner films responsible for capillary-driven evaporation [17]. The eventual disruption of hydraulic continuity with the surface occurs when downward viscous forces (and gravity)

surpass the upward capillary driving force at a specific depth of the drying front. This disruption signifies the conclusion of CRP. Subsequently, liquid menisci retract from the surface to a level below, establishing a new vaporization plane known as the secondary drying front [102].

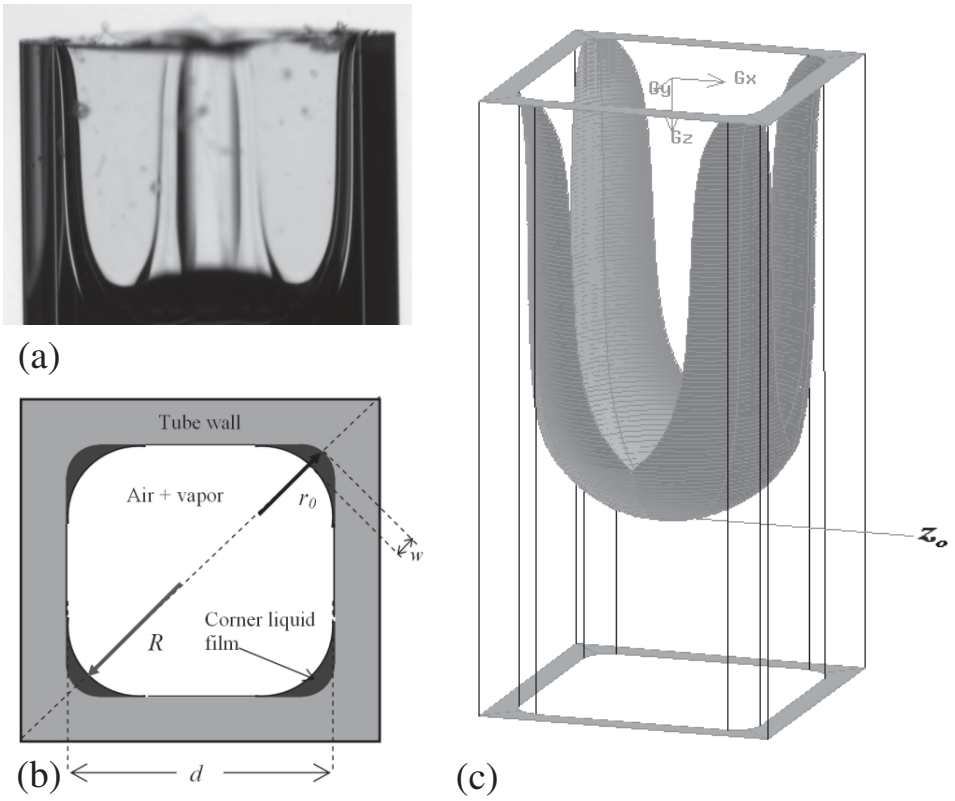


Figure 2.5: (a) Illustration of corner liquid films for square capillary tube at the tube entrance, with the camera aligned along the tube's diagonal axis [indicated by a dashed line in (b)] (b) Sketch of the cross-sectional view of the tube in the corner film region. Here, r_0 represents the curvature radius of the rounded corner, R denotes the in-plane curvature radius of corner menisci, and w is the thickness of the corner film (c) Computed representation of the shape of the gas-liquid interface within the tube. Figure was reproduced based on work in Ref. [17].

The transition from CRP to RFP occurred through the intermediary phase of FRP, marked by a notable transition to substantially lower drying rates governed by diffusion rather than advection. During FRP, the drying rate is constrained by mass (vapor) transfer

through the viscous air film at the surface. The dominance of diffusion arises as the drying front recedes, and the film region no longer reaches the surface, referred to as "depinning". In RFP stage, evaporating substance diffuses slowly toward the surface which makes it a completely diffusion-dominant process [17, 100]. This process contributes to the significantly slower drying rate compared to CRP which can be found in Figure 2.4.

Although these stages can be observed in various drying experiments, the drying rates may differ due to the geometry of the drying medium. For instance, the drying rate is notably higher in a square tube compared to a circular one [9, 17]. This disparity is attributed to the corner films in the square tube, providing a pathway for transporting the liquid from the receding bulk meniscus up to the film tips. Three primary drying stages can be easily distinguished in the drying process within a square tube but these stages are not easily distinguishable in the drying process within a circular tube (Figure 2.6). It can be seen that an initial phase where (z_o) appears to vary linearly with time, followed by a crossover period where the bulk meniscus experiences a significant drop, and ultimately shifted to third phase, as illustrated in the inset of Figure 2.6, where $z_o \propto \sqrt{t}$.

Though single capillary tube are used to gain insights of transport phenomena in drying for simplicity, it is important to understand the pore-scale physics with the porous media having real pore structures of varying pore sizes and properties. Shokri et al. [103] used real porous structures made with sand and glass beads to observe the drying stages and find the corresponding reasons behind those. A noncontinuous retreat, or jump, of the capillary-held liquid front was observed after the Constant Rate Period (CRP), establishing a new secondary vaporization plane at a predictable depth below the surface (Figure 2.7). This creation of the secondary vaporization plane resulted in a notable reduction in drying rate, transforming the system into a diffusion-controlled evaporation process [103], which is similar to the observations in the single capillary tube drying experiments [17]. The jump length of the vaporization plane is a function of the dimensionless Bond number, which is derived

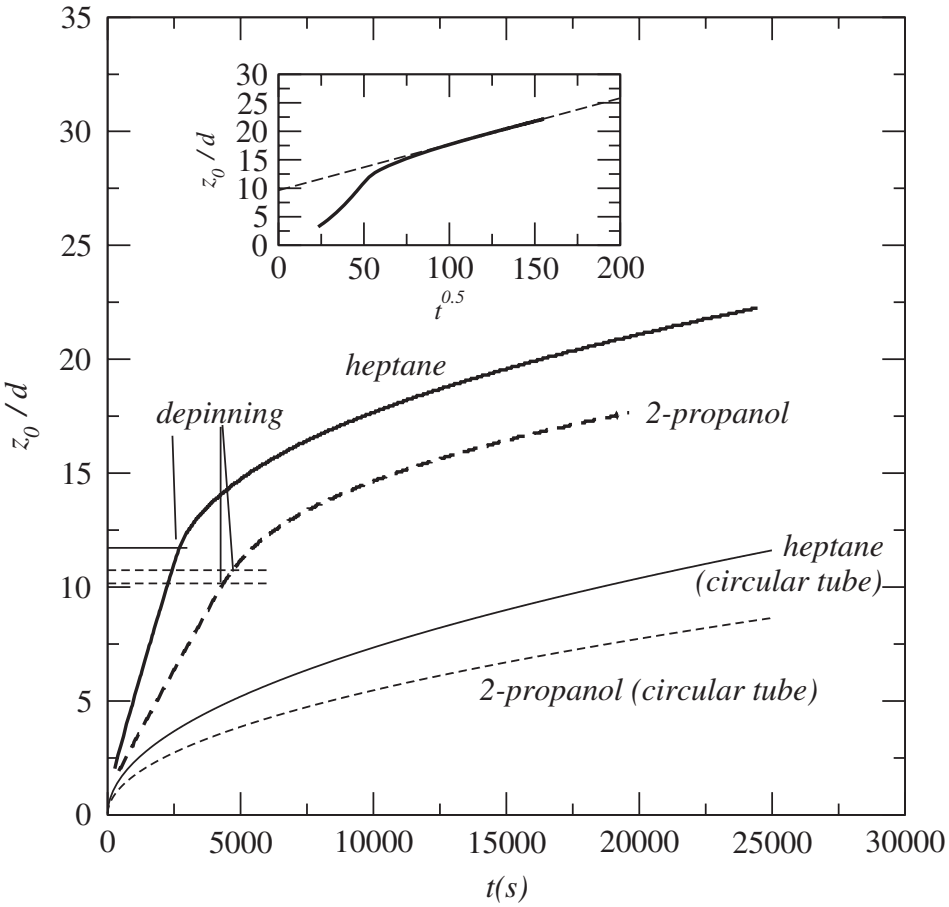


Figure 2.6: Transformation of bulk meniscus position (z_o) over time (t). The thick solid line and dashed line represent data from the square tube, while the thin solid line and dashed line at the bottom correspond to a circular tube. Inset plot shows z_o evolution over $\sqrt{t}$ in the square tube with heptane. The position of corner liquid film detachment from the tube entrance (depinning) is marked. Notably, depinning does not occur simultaneously in all four corners during the 2-propanol experiment. The two dashed lines indicate the initial depinning and the point when depinning has occurred in all four corners, respectively. Figure was reproduced based on work in Ref. [17].

from the ratio of gravity forces to capillary forces [123].

In industries focusing on drying processes in porous media, extending the constant rate period (CRP) is crucial for optimizing their efficiency. On the other hand, to mitigate overall drying-induced drought and maintain soil moisture, it is imperative to implement strategies to reduce drying, especially CRP. Understanding the CRP is key to achieving controlled

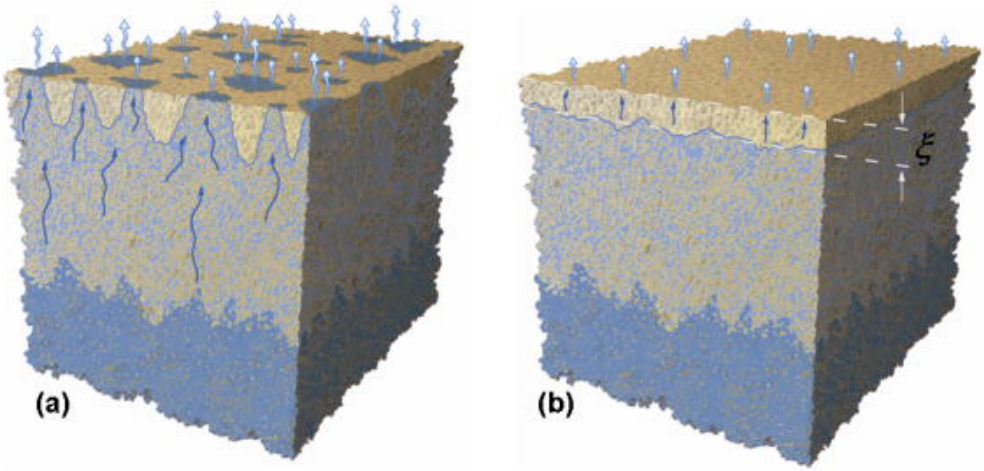


Figure 2.7: Illustration of the jump of the liquid meniscus from the surface, leading to the formation of the secondary drying front (vaporization plane) at the end of CRP. (a) Detachment of the liquid meniscus from the surface and its pinning to a level below during the transition from CRP to RFP. (b) Formation of the secondary drying front leading to diffusion-controlled drying. Figure was reproduced based on work in Ref. [103].

drying processes. Previous research at the pore scale mainly explored mass transport mechanisms within the porous medium, neglecting mass transfer over the surface. However, recent work by Hussary et al. (2022) [50] considered both surface and internal mass transfer. Their study demonstrated that the drying rate remains nearly constant as long as liquid films are present in the pore network, ensuring hydraulic connectivity between the bulk liquid and the evaporating surface. This condition holds true for lower wetting phase saturation. It contrasts with Suzuki et al.'s (1968) [110] findings, which only considered external mass transfer and found this occurs only in sufficiently wet conditions. Two additional drying periods, the falling rate period (FRP) and the receding front period (RFP), were identified. In the FRP, drying is controlled by mass transport mechanisms within the porous material [17].

Alternatively, a flow-through drying process, known as advective drying, is another type of drying that may occur when a gas passes (dry or saturated) through a partially saturated porous medium containing liquids [3, 75, 76]. In contrast to diffusive drying

processes, advective drying processes exhibit distinctive characteristics. Notably, the drying rates in advective drying are no longer governed by the diffusion of gas in porous media. Instead, the key determinant becomes the compressibility of gas and the capillary properties of the porous medium [64, 75]. Mahadevan et al. (2007) [76] observed that saturated and unsaturated injected gas had different characteristics on the saturation profiles during advection drying of water-saturated sandstone and limestone. For saturated gas injection, advective drying primarily occurs due to gas expansion and capillary-driven flow from regions of high saturation to regions of low saturation resulting in more uniform saturation profiles. Conversely, during the injection of dry gas, a drying front forms at the inlet and progresses through the porous medium with the gas expansion effect on the outlet [76]. It was observed that the expansion of gas played a pivotal role in the advection drying with saturated or wet gas to remove water blocks from gas-producing wells [54, 74]. Mahadevan et al. (2005) [74] also mentioned the influence of high-pressure drops, hydrophobicity of the porous medium, and the addition of solvents in enhancing the efficiency of advection drying.

The heat field is another factor influencing drying in porous media. When taking the heat field boundary condition into account, the drying process can be either isothermal or non-isothermal. Non-isothermal porous media drying differs from isothermal drying mainly due to the significant impact of temperature gradient on phase distribution. In the isothermal system, gas displaces liquid in a classical invasion percolation pattern [89], resulting in a two-region phase distribution where a dry zone continuously expands next to the side exposed to the atmosphere, while a two-phase zone steadily contracts, with both liquid and gas present [115]. In contrast, the non-isothermal system follows a stabilized invasion pattern [88], leading to a three-region phase distribution with a growing dry zone next to the open side, a diminishing liquid-saturated zone near the sealed bottom, and a finite traveling two-phase zone between them [115]. This pattern emerges due to the temperature-dependent surface tension, making it easier for gas to displace the liquid phase from warmer throats

[87].

In recent decades, global warming has significantly impacted the world's climate, leading to a rise in average global temperatures and alterations in rainfall patterns. Many regions across the globe are experiencing prolonged and intense heat waves, impacting freshwater resources, and groundwater availability. Consequently, agriculture and ecosystems are significantly affected by severe soil degradation and drought conditions due to the disparity between precipitation and evaporation rates. These anticipated changes contribute to the aggravation of desertification, posing one of the most significant environmental challenges of the current century. Addressing these environmental issues requires a comprehensive understanding of pore-scale physics within soil. Soil has distinct property mechanism inside to control nutrient transport and ecological balance which is controlled by the drying of soil. Existing studies predominantly examine the evaporation process from a macroscale perspective, estimating evaporation rates based on atmospheric conditions [17, 98, 102]. However, only a limited number of studies take into account the crucial role of soil properties in drying considering fluid dynamics perspective [38, 65, 103].

Soil structural form refers to the heterogeneous arrangement of solid and void spaces existing at a given time, impacting various aspects such as water movement, storage, aeration, erosion, biological activity, and crop growth [111]. It is a hierarchical system of aggregates (unity of solids and pores), which perform a broader range of functions compared to pores alone [84]. Aggregates form a three-dimensional matrix with microaggregates ($<250\,\mu$m) and macroaggregates (0.25-2 mm), which are in turn composed of mineral particles and organic carbon. They play a defining role in soil properties such as organic carbon and water content, as well as their flow dynamics [14, 106, 107]. The interiors of these aggregates create microenvironments with distinct properties, providing spatially heterogeneous niches for microorganisms. Understanding these structures and the dynamics of pore-scale flow is essential for comprehending soil ecology and the dynamics of terrestrial ecosystems.

The presence of microaggregates and macroaggregates with different pore sizes creates a multiscale environment known as dual-porosity. This dual-porosity environment influences various activities, including gases and water transport, through multiscale flow dynamics and inter/intra-aggregate interactions during drying. However, the fundamental physics underlying the drying of porous media with dual porosity is not well understood from a fluid mechanics perspective.

Micromodel

The study of flow and transport of phases and components through porous media holds significant importance in various fields such as subsurface engineering, biological engineering technologies, and energy-related research. A comprehensive understanding of the physiochemical mechanisms operating at the micrometer length scale is crucial to the success of these technologies. As real porous media in nature are not transparent, surrogate porous media that are artificially fabricated using microfabrication techniques can be handy to visualize complex fluid flow, transport phenomena, and fluid-solid interaction in porous media. Microfluidic devices of porous media, commonly referred to as micro-models, are devices that have connected porous structures inside and are transparent at least on one side to directly visualize the flow. Since the emergence of the first micromodel, dating back to the 1950s [16], researchers have effectively developed various artificial micron-scale features inspired from natural systems to study and investigate the flow of fluids, particles, and solute transport phenomena. Experiments with porous media are typically fast, as the sample volume is substantially low due to the use of miniaturized microfluidic devices. Indeed, microfluidics provides an ideal platform for visually observing flow with both high temporal and spatial resolutions. Micromodels are designed in diverse ways to investigate specific phenomena, utilizing advanced imaging techniques for thorough analysis. Various materials are currently being utilized to fabricate micromodels, depending on specific

requirements and material properties. Silicon, glass, and polymeric materials, including polymethylmethacrylate (PMMA), polystyrene (PS), polycarbonate (PC), and the widely used polydimethylsiloxane (PDMS), are among the options.

To fabricate microfluidic devices, optically transparent materials must be utilized at least on one side to observe the pore-level flow with microscope and camera under transient conditions. Common transparent material options are glass and some polymers such as polydimethyl siloxane (PDMS) and polymethyl methacrylate (PMMA). These materials have distinct mechanical, thermal, and chemical properties, and also need different fabrication processes from other materials. Within these materials, some micro-models possess flexibility, while others are characterized by their rigidity. For instance, micromodels constructed from glass exhibit a rigid nature, whereas PDMS micromodels are deformable to some extent. The selection of material for micromodel fabrication is crucial because the decision is vastly influenced by the unique advantages and disadvantages of each material. The choice of material ultimately depends on the specific demands of the intended application, research goals, budget considerations, and compatibility constraints.

Considering the flexibility of micromodel, ease of fabrication, and cost-effectiveness, well-defined channel geometries, such as straight walls, flat bottoms, optical transparency, and biocompatibility, PDMS is a good option as a polymer [66]. Dynamic deformation under pressure makes PDMS ideal for developing pressure sensors on microscale [92]. On the other hand, permeability to gases, limited compatibility with certain solvents, oils, and chemicals, hydrophobic surface properties, and vulnerability under high pressure can pose challenges in specific experimental scenarios. Unlike PDMS, PMMA has higher rigidity and chemical resistance for various solvents and chemicals. However, fabrication cost, reduced biocompatibility, and lower gas permeability potentially affect certain experiments.

Due to their inherent rigidity, glass micromodels may be more susceptible to fragility and entail higher fabrication costs, often necessitating intricate fabrication techniques.

However, glass stands out as the predominant material for micromodel fabrication for its extensive compatibility with gases, chemicals, solvents, and inert surface properties. The exceptional transparency of glass facilitates a clear visualization of fluid and particle dynamics. Furthermore, glass micromodels exhibit heightened durability, enabling their resilience under extreme pressure conditions, as observed in experiments such as CO_2 sequestration. Glass thus remains the prevalent choice for crafting robust and transparent micromodels.

Among the various types of micromodels, non-flexible and harder micromodels demonstrate versatility in their applications. Traditionally, two distinct approaches exist for the fabrication of robust micro-models, as outlined in [40]. The first method relies entirely on glass, while the second integrates both glass and silicon components. In the case of micromodels exclusively composed of glass, the verticality is compromised due to the wet etching process which is isotropic, although it maintains transparency on all sides [51]. On the other hand, micro-models made with glass and silicon exhibit enhanced verticality of the feature walls [44]. However, this advantage is counterbalanced by a reduction in transparency, attributable to the inherent non-translucent properties of silicon. Consequently, silicon-glass micromodel permits optical measurements solely from one side concurrently [35].

Imaging Techniques

Visualizing fluid flow at the pore scale is essential for the success of microfluidic experiments, serving as a versatile tool for both qualitative and quantitative analysis. Researchers have innovatively developed diverse imaging techniques to address the dynamic requirements of experiments, considering factors such as resolution, speed, and the inherent characteristics of the samples involved. Notable methods in this realm include X-ray micro-computed tomography (X-ray μ-CT), nuclear magnetic resonance (NMR), confocal microscopy, transmitted and reflected microscopy, fluorescent microscopy, and particle image

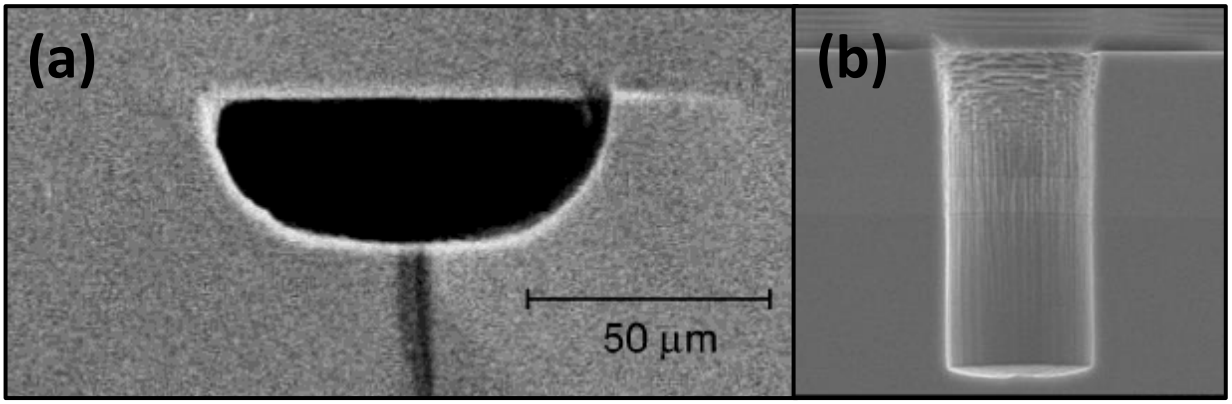


Figure 2.8: SEM images of (a) Wet etched glass micromodel channel bonded at room temperature having curved walls (Figure was reproduced based on work in Ref. [53]), (b) Silicon micromoel channel dry etched with Oxford ICP Showing the high quality, smoothness and verticality of the etch (Figure was reproduced based on work in Ref. [25]).

velocimetry (PIV). Each of these techniques offers unique advantages and disadvantages addressing distinct aspects of flow analysis.

Among the imaging techniques, X-ray μ-CT stands out for its non-destructive nature, allowing for detailed three-dimensional visualization of internal structures without compromising sample integrity. Flow visualization utilizing real rock samples posed a significant challenge before the introduction of X-ray μ-CT [5, 28, 45]. The application of X-ray μ-CT in the study of fluid flow in porous media is important, as it allows for the direct imaging of the actual pore space in real rock because of its high spatial resolution compared to NMR. However, X-ray μ-CT faces challenges in imaging dense materials due to limited X-ray penetration, restricting its applicability in samples with high-density packed components. Additionally, the slower image acquisition nature of X-ray μ-CT scans restricts its usage in experiments with rapid events which would require high-speed data acquisition. Furthermore, the high cost of equipment poses a barrier to widespread adoption, limiting accessibility for research facilities with budget constraints.

Confocal microscopy is another image acquisition technique for high-resolution ($<1\,\mu m$)

three-dimensional (3D) imaging in microfluidic samples with a maximum depth of around 250 µm but adepts at capturing relatively lower temporal resolution within the optical diffraction limit [55]. This image acquisition technique has been utilized to monitor colloids and investigate single-phase and two-phase fluid flow in microfluidic and porous media [27, 128], to measure the water meniscus shape and film thickness on sand grains [127]. Furthermore, confocal laser scanning microscopy (CLSM) has been utilized for the investigation of biofilm development in microfluidic devices study of bacteria producing a green fluorescent protein [67, 93].

For transmitted and reflected microscopy, visualization of the flow inside microfluidic devices involves the use of a camera coupled to a microscope which enables high-resolution image acquisition of specified porous regions during the experiments. The image acquisition technique can be utilized in experiments with the microfluidic device having at least one transparent side for optical access. This acquisition technique can be used to capture rapid events in the experiment with a higher spatial resolution. Acquired images from experiments can be utilized to interpret different parameters, such as interfacial curvature and length, Haines jumps, contact angles, fluid saturation, salt deposition, corner film flow, and different pressure measurements [6, 70, 77, 78, 79]. Additionally, for the experiments requiring a larger FOV, non-standard microscopy has been used to record rapid event experiments [4, 46, 77]. In such configurations, cameras, placed at flexible distances and orientations from the micromodel, capture images and videos of the flow generally at lower resolution because of the absence of a coupled microscope.

Fluorescent microscopy is key to differentiating fluid phases in flow. To differentiate between fluid phases in flow, various methods are employed, such as mixing the fluid with dye [126], introducing fluorescent particles into the flow [59], monitoring light intensity changes [15]. For fluorescent visualization, a fluorescent dye or particle is added to the solution, and a light source excites the fluorescent molecules. The resulting higher wavelength

fluorescence signal is captured by a digital camera through long-pass filter. Epifluorescence microscopy, a special kind of fluorescence microscopy, involves passing a parallel beam of light directly through the sample to maximize illumination. This technique utilizes a high-intensity light source, and both the illuminated and emitted light travel through the same objective lens. This technique is suitable for various fluorescent microscopy applications including experiments with thicker samples [119].

Microscopic particle image velocimetry (micro-PIV) emerges as a particle-based, nondestructive technique for fluid velocity measurement. This approach involves tagging fluid with tracer particles, illuminated by volume illumination. Factors such as illumination method, particle properties, chemical interactions, camera speed, and camera sensor resolution influence the accuracy of velocity measurements in micro-PIV [21, 58, 96, 122].

In summary, a variety of microscopy and imaging techniques are employed in microfluidic experiments, each offering unique advantages and applications in studying fluid dynamics and transport phenomena in porous media.

In the case of dual porosity samples, such as micromodel inspired from soil, the presence of two distinct porous regions characterized by varying pore sizes introduces complexity in analyzing the system. These regions exhibit divergent properties and activities, necessitating concurrent data acquisition at different magnifications due to their inherent scale differences. The challenge lies in the fact that a single magnification can only capture data relevant to that specific scale. When it comes to imaging, the limitation arises from the fact that a single camera or microscope operates at a fixed magnification. To overcome this constraint and obtain images at dual magnifications, a setup involving two cameras or microscopes becomes imperative [48]. In the context of entirely glass micromodels, while a camera can be utilized on different sides, the presence of curved walls poses a challenge in interpreting the acquired data. The intricacies introduced by the curved surface complicate the data analysis process. On the other hand, glass-silicon-based micromodels offer a different set of

considerations. While they possess desirable properties, such as compatibility with multiple magnifications, the inherent non-transparency of silicon restricts the simultaneous use of multiple magnifications. This limitation underscores the need for a thoughtful trade-off between desired properties and the constraints imposed by the material's transparency characteristics. Heshmati et al. (2018) [48] utilized a PDMS-glass-based micromodel to take the benefits of the dual-magnification imaging system. However, wettability considerations can create issues with many pore-scale experiments.

CHAPTER 3 EXPERIMENTAL METHOD

Micromodel Design

The micromodels employed in this study featured a three-layer architecture. These micromodels were constructed using a combination of silicon and glass, with silicon sandwiched between two glass wafers as schematically shown in Figure 3.1. Each micromodel consisted of three main components: a porous region, an inlet, and an outlet situated on opposite sides. This micromodel has glass layers both at the top and bottom and because of through etching of silicon, this micromodel is transparent on both sides, which facilitates imaging from two different sides with two different magnifications.



Figure 3.1: Schemactic structure of three layer glass-silicon-glass micromodel.

The micromodel fabrication process initiates with the design of the photomask, containing the intricate porous patterns intended for etching onto a silicon wafer. In this research, three distinct types of micromodel, each characterized by unique porous regions, were utilized and named 'Case 1', 'Case 2', and 'Case 3' (illustrated in Figure 3.2 and 3.4). These micromodels were meticulously designed to investigate various flow properties within porous media, taking into account diverse porous characteristics. All of the patterns for micromodel fabrication were designed in SolidWorks and made for photo-mask print-ready in Adobe Illustrator.

The micromodel pattern Case 1 (shown in Figures 3.2 a,b,d) consists of only homogeneous circles of 200 μm diameter. In contrast, the micromodel pattern for Case 2 (shown in Figure 3.2 a,c,e) is composed of two distinct circular patterns: a larger circle with a diameter

Table 3.1: Porosity of the micromodels in Figure 3.2

Case Name	Case 1	Case 2
Porosity	42.19%	48.48%

of 200 μm and smaller circles with diameters of 40 μm. These patterns for these cases follow specific designs with defined parameters (shown in Figure 3.2 d,e). Case 2 micromodel has two different porous regions (Figure 3.2 c,e): a micro-pore region consists of 40 μm diameter pillars with a total width of 1 mm within the whole porous region; two macro-pore regions each with a span of 2 mm on either side of the micro-pore region. This combination makes the Case 2 a dual-porosity system. All these micromodels of Case 1 and Case 2 share a commonality in having porous regions spanning an area of 5mm$\times$5mm and have a flow channel of 1mm width and 50mm of length (shown in Figure 3.2 a). These micromodels have a depth of 30 μm($\pm$2μm). Because of the distinct distances among the pillars in the micromodel patterns, different pore sizes form and can be identified in Figure 3.3 for each case.

Case 1 and Case 2 micromodels (shown in Figure 3.2) were employed to investigate the diffusion-driven drying process and other flow properties. Specifically, they offered insights of flow interactions between two different sizes of pores and the area concentration of deposition of particles or salt during the drying process within dual-porosity systems. Case 1 micromodel served as the baseline pattern, facilitating an understanding of the distinctions between homogeneous and dual-porosity systems. Moreover, Case 2 micromodel differ primarily in porosity because of the microporous region (shown in Figure 3.2d,e with dimensions), with specific porosity values detailed in Table 3.1. This deliberate variation in porosity allows for a comprehensive exploration of porous structure impact on the flow properties, drying characteristics, saturation distribution, and flow interactions within the

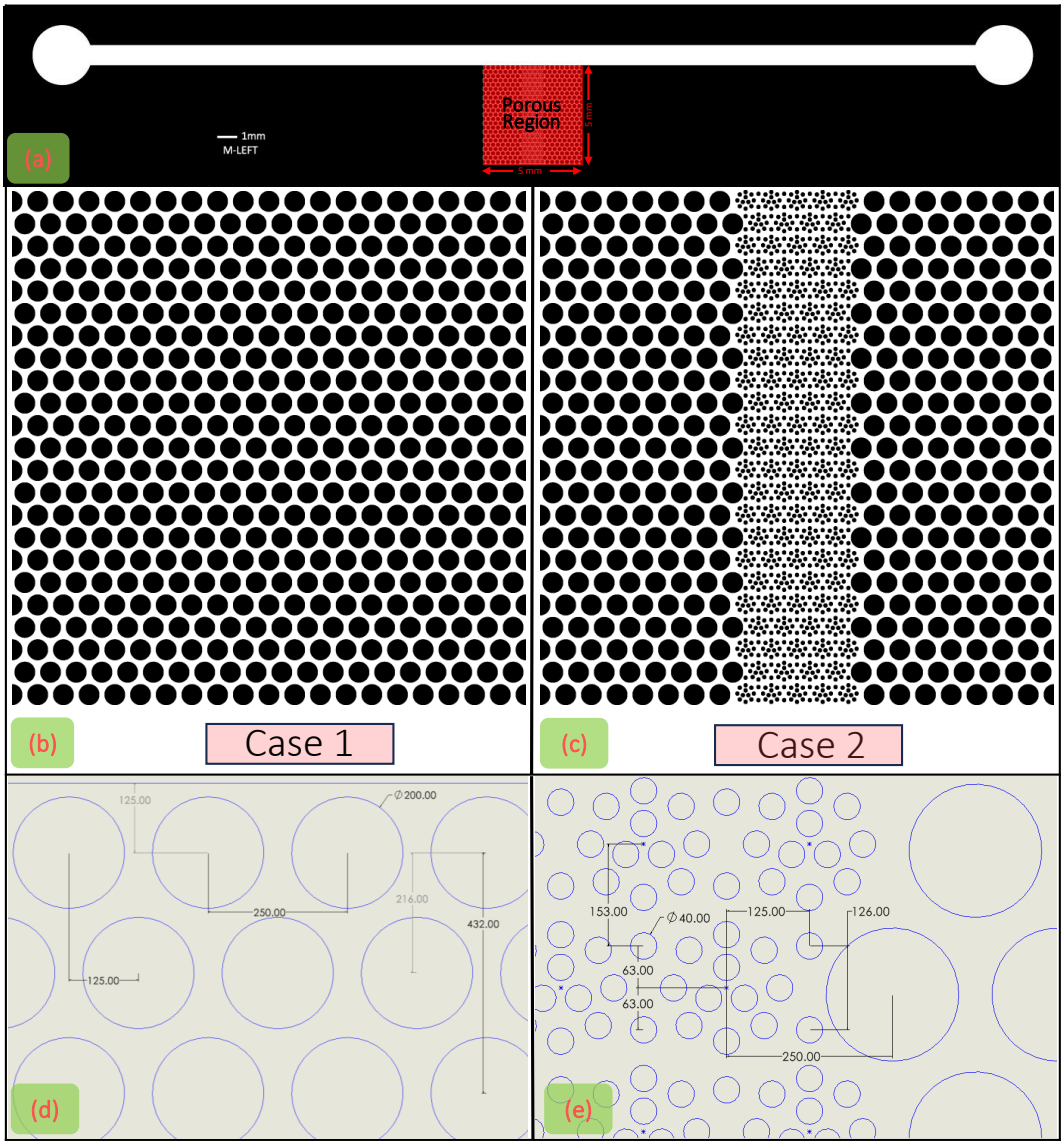


Figure 3.2: Illustration of (a) 2D photo-mask pattern of Case 1 and Case 2 micromodels with inlet and outlet on the opposite side of the porous region. The porous region is replaced with b and c to make distinct micromodel patterns for Case 1 and Case 2 respectively; (b) Porous region of photo-mask pattern for homogeneous micromodel with circles of 200 μm diameter. This design is marked as 'Case 1' ; (c) Photo-mask pattern for dual-porosity micromodel having smaller 40 μm circle sets in the middle of larger 200 μm circles. The pattern in c is named 'Case 2'; (d) and (e) are the SolidWorks designs with the required dimensions of photo-mask porous region patterns in b and c respectively. All the dimensions in d and e are in μm.

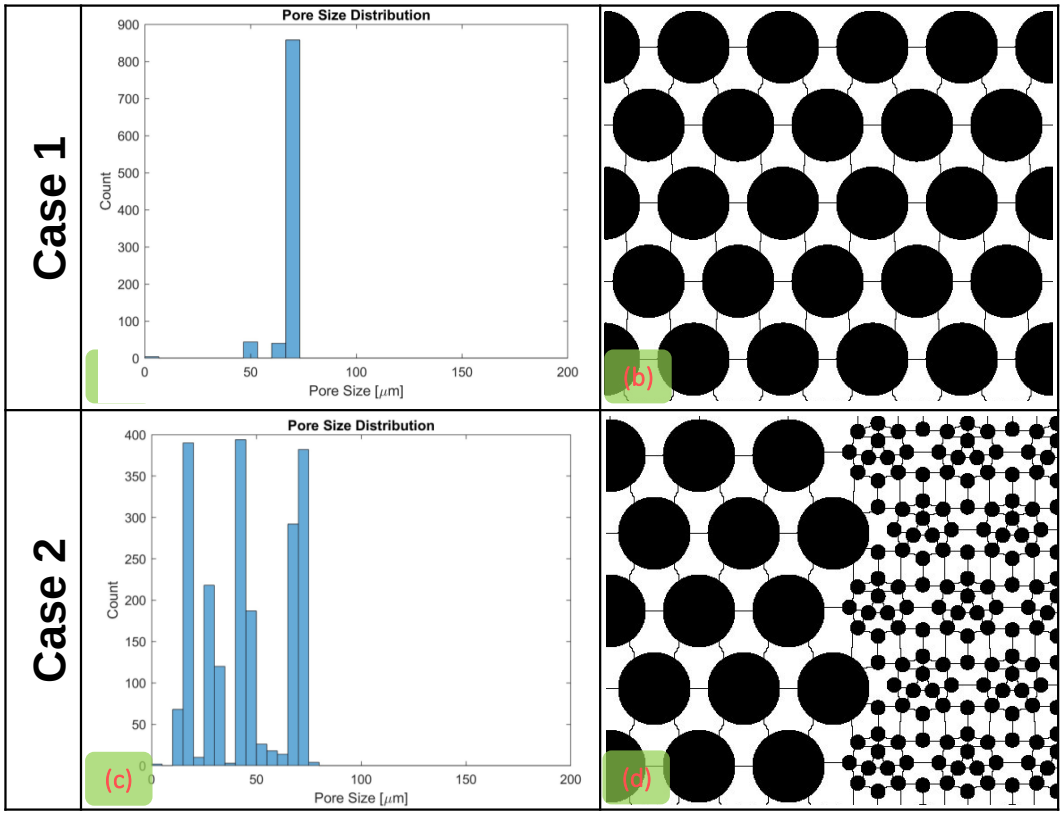


Figure 3.3: Pore size distribution and corresponding pores for different micromodel patterns; (a) and (c) are Pore size distributions for Case 1 and Case 2 respectively, where the number of the pores shown with the pore diameter (μm); (b) and (d) are corresponding pores for Case 1 and Case 2 respectively.

micromodels during drying.

In contrast, Case 3 is the heterogeneous dual-porosity micromodel pattern (shown in Figure 3.4a,b) inspired from the intricate structure of real soil. The heterogeneity within this micromodel pattern of the porous region encompasses micro and macro pores of varying sizes. This porous region spans an area of 6mm$\times$4mm, exhibiting an approximate porosity of 50%, calculated by dividing the number of pixels of pore space by the total area of the porous region. The pore size distribution graph in Figure 3.4 c reveals two distinct peaks, the left peak for smaller pores and the right peak for larger pores, indicating that the micromodel exhibits a dual-porosity porous structure. This specific micromodel pattern was chosen to

gain insights into the advection drying process within the soil and the flow interactions among the micro- and macro-pores, owing to its dual-porosity nature. Hence, the flow is directed into the micromodel via an inlet, traverses through the porous region, and exits through the outlet on the opposite side.

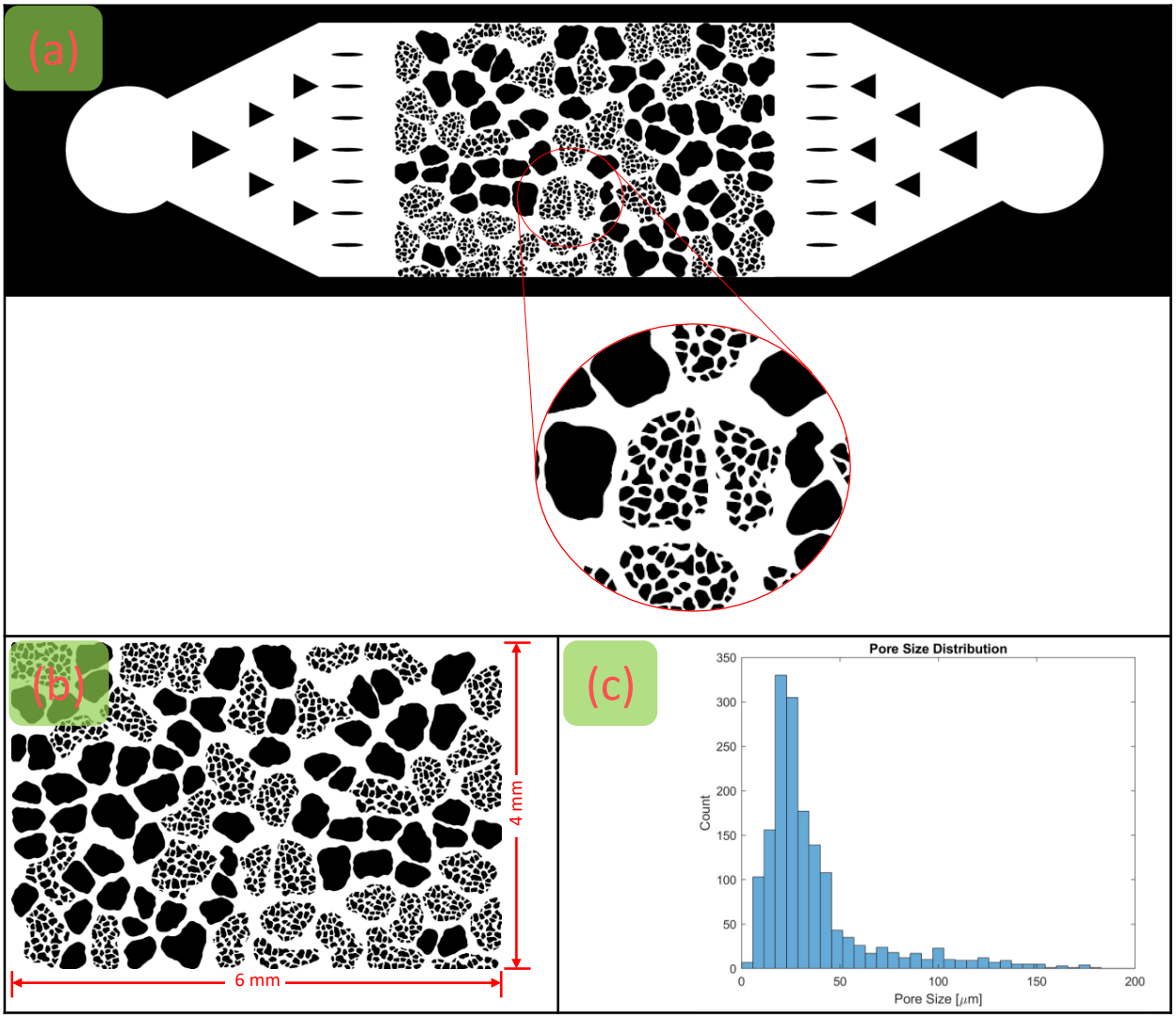


Figure 3.4: (a) 2D photo-mask pattern of the heterogeneous microcromodel (Case 3) with inlet and outlet. The circular cutout is the zoomed portion of the heterogeneous photo-mask showing the micro and macro pores; (b) Porous region of Case 3 micromodel photo-mask with the dimensions of the whole porous region; (c) Pore size distribution of Case 3 micromodel, where the number of the pores shown with the pore diameter in micro-meter.

Micromodel Fabrication

The fabrication process was carried out in Montana Microfabrication Facility (MMF) and the Microfluidics Lab for Energy and Fluid Transport (M-LEFT) at Montana State University following the step-by-step procedure illustrated in Figure 3.9. To fabricate the previously mentioned micromodels with the desired properties, the process was initiated by cleaning thoroughly a 4-inch standard double-side polished silicon wafer and and a 4-inch Borofloat 33 glass wafer. Both of the wafers were of 500 μm ($\pm$25 μm) thickness. The cleaning was completed using Piranha solution for 10 minutes to eliminate any organic residues. Here, 3:1 volume ratio of 96% Sulfuric Acid (H_2SO_4) and 30% Hydrogen Peroxide (H_2O_2) of semiconductor grade were used to make the Piranha solution. After the cleaning, the wafers were completely blown dry with high-purity nitrogen. Then the clean silicon wafer was anodically bonded to the glass wafer following the steps mentioned in Wei at el. [120]. Subsequently, the thickness of the silicon wafer was then reduced to 30 μm ($\pm$2 μm) employing a wet etching process with Potassium Hydroxide (KOH). The KOH solution at a concentration of around 35% was maintained at a temperature of 90°C during the etching process. The etch rate for silicon during wet etching varies depending on the concentration change of KOH and the temperature of the solution. During this wet etching, no significant roughness in the silicon and glass wafer was noticed. It is worth noting that the glass wafer bonded to the silicon was also measured with reduced thickness by about 10μm due to the KOH etching during the whole wet etching process.

Following the silicon wafer thinning, the standard photolithography process was carried out to imprint the two-dimensional micromodel pattern using a pre-fabricated photomask for making precise porous structure on the silicon wafer. Before starting the photolithography, the bonder wafer was plasma cleaned with PVA TePla IoN 100 plasma cleaning system. Afterward, the wafer underwent a coating process with a thin layer of Hexamethyldisilazane

(HMDS) adhesion promoter using a vapor prime oven (Yield Engineering System III Vapor Prime Oven) to enhance the adhesion of the photoresist. Following this, a positive photoresist (AZ10XT) was coated on the wafer using a spin coater (Laurell EDC-650-8B Spin Processor) operating with 2 step rotation total duration of 50 seconds; first rotation at 500 rpm (with a 250 rpm/s acceleration) for a duration of 5 seconds and second one at 5000 rpm (with a 1000 rpm/s acceleration) for a duration of 45 seconds. After the spin coating, the wafers were soft-baked on a hot plate at 110°C for 4 minutes. After this, the wafer was left in the wafer holder for drying of the photoresist for 30 minutes to improve photoresist adhesion. Following the drying step, the wafer was then exposed to UV light for 25 seconds at an intensity of 15 mW/cm^2 using a contact aligner (ABM-USA Inc.). Following exposure, the wafer was immersed in the developer (AZ300 MIF) and stirred for 10 minutes using an orbital shaker at 40 rpm to undergo the development of the pattern. Subsequently, the wafer undergoes a thorough rinsing and cleaning process with DI water, followed by drying with N_2. The features on the wafer are then scrutinized under an optical microscope to inspect for any defects. The printed silicon wafer was subsequently subjected to dry etching using Inductively Coupled Plasma-reactive Ion Etching (ICP-RIE) to etch the silicon from the printed patterns to produce porous region and other supporting structures. This dry etching was continued until all the silicon was removed from the printed pattern to get through etched porous structure. This through etching process made the micromodels transparent (shown in Figure 3.5).

After the lithography and dry etching, through holes were drilled into the previously processed silicon and glass wafer for each micromodel as inlets and outlets using a diamond drill bit-equipped drill machine. Following the drilling process, both the processed silicon-glass bonded wafer and an additional new 4-inch glass wafer underwent cleaning with a Piranha solution. This step was taken to eliminate any residual photoresist and dust and also make the silicon and glass surfaces hydrophilic. Notably, silicon is naturally hydrophobic;

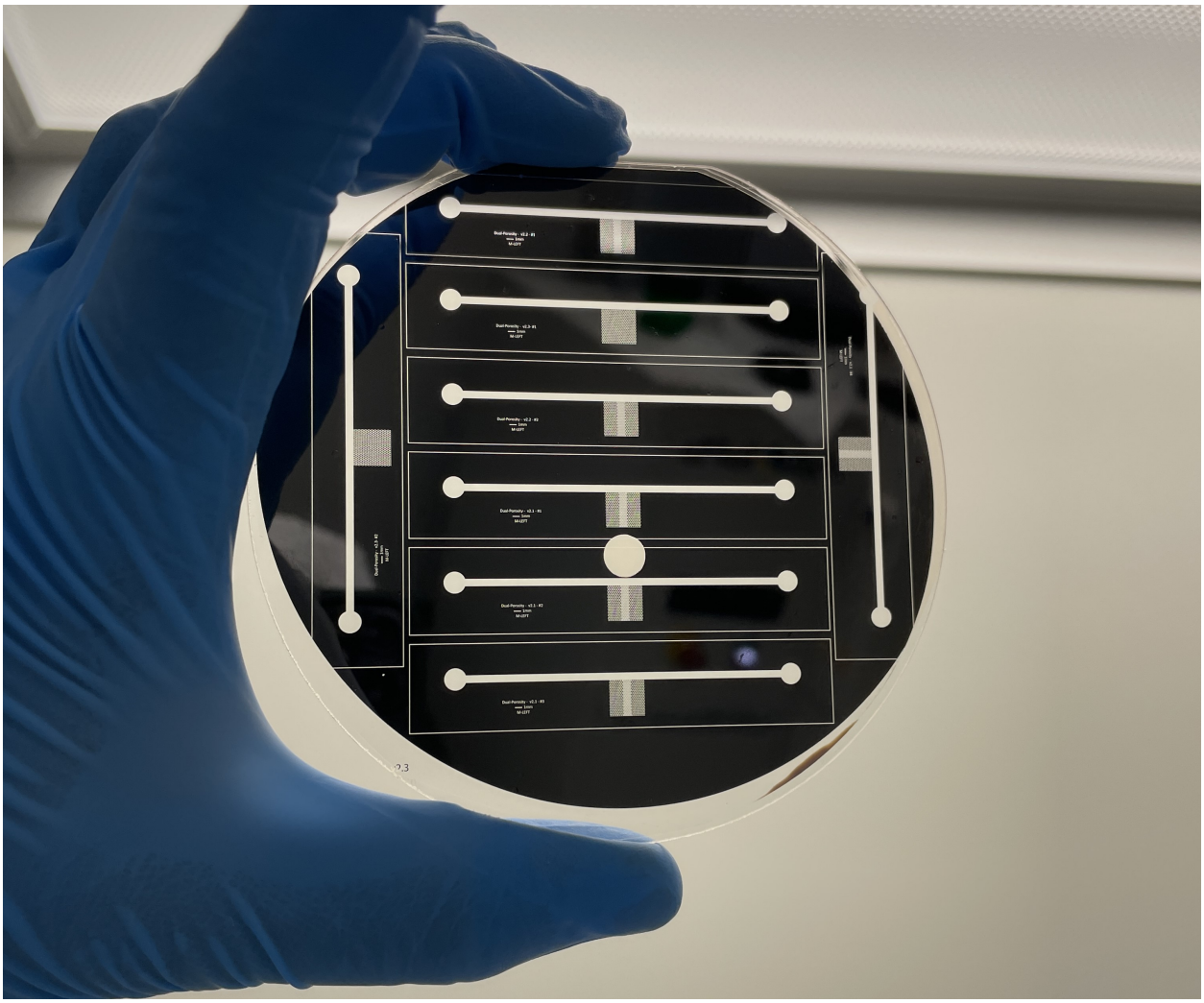


Figure 3.5: Image of the wafer after dry etch. The transparency of the micromodel can be noticed because of the thorough etching of silicon.

thus, Piranha solution was used to hydroxylate the silicon to make the silicon surfaces hydrophilic. Following the cleaning process, the etched silicon wafer with glass was anodically bonded to another glass wafer to form a three-layer glass-silicon-glass architecture. Due to the thorough etching of silicon and glass on both sides, the porous region of the micromodels remained transparent, enabling visualization of fluid flow from both the top and bottom perspectives, as demonstrated in Figure 3.7. The individual micromodels were then separated by dicing using a precision silicon and glass wafer dicing machine. Finally, two nanoports

were attached to the inlet and outlet of each micromodel for fluid delivery. For heterogeneous micromodel customized nanoports were used. These nanoports featured a custom design for easy installation aligned with the micromodel's inlet and outlet, had a reduced height to fit within the focal range of microscope objectives, and securely held the delivery lines to prevent any leakage. These nanoports were manufactured in MSU Makerspace with Resin 3D Printers.

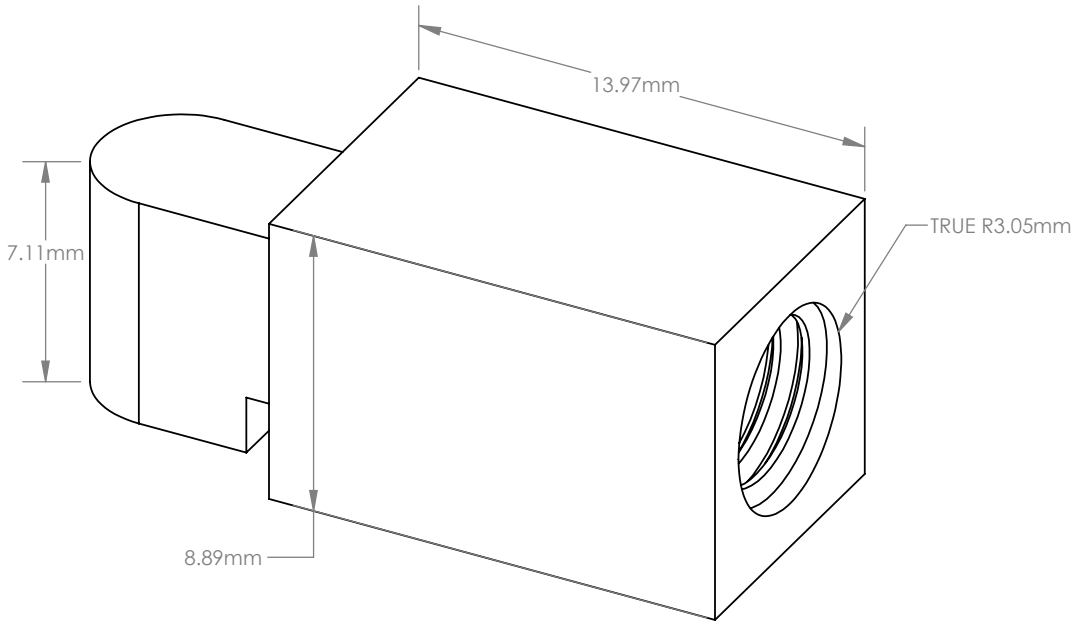


Figure 3.6: Isometric view of the customized nanoport used to flow the fluid through the channel. It was customized to fit within smaller focal length of the higher magnification objective without blocking the view of the whole porous region.

The quality assessment of the micromodels involved measuring their thickness with a stylus profilometer. Verification of the feature size, wall verticality, and surface roughness was conducted using Scanning Electron Microscopy (SEM) in the Imaging and Chemical Analysis Laboratory (ICAL) at Montana State University (Figure 3.8). The SEM imaging was performed before the second anodic bonding of wafers, and notably, no sputter coating

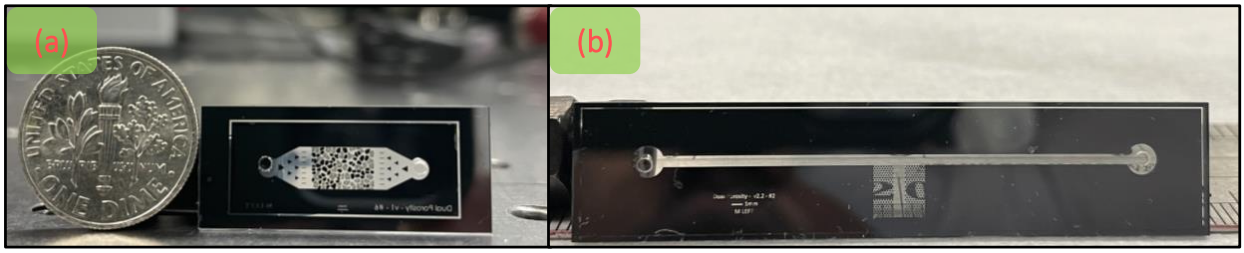


Figure 3.7: Actual images of (a) Case 3 (heterogeneous and dual-porosity) micromodel sample without the attached nanoports; (b) Micromodel fabricated with the pattern mentioned in Figure 3.2 without attached nanoports.

was applied; instead, carbon conductive adhesive tapes were utilized. In Figure 3.8, it can be seen that the fabrication steps applied here are suitable for precise porous structures with vertical walls of the silicon.

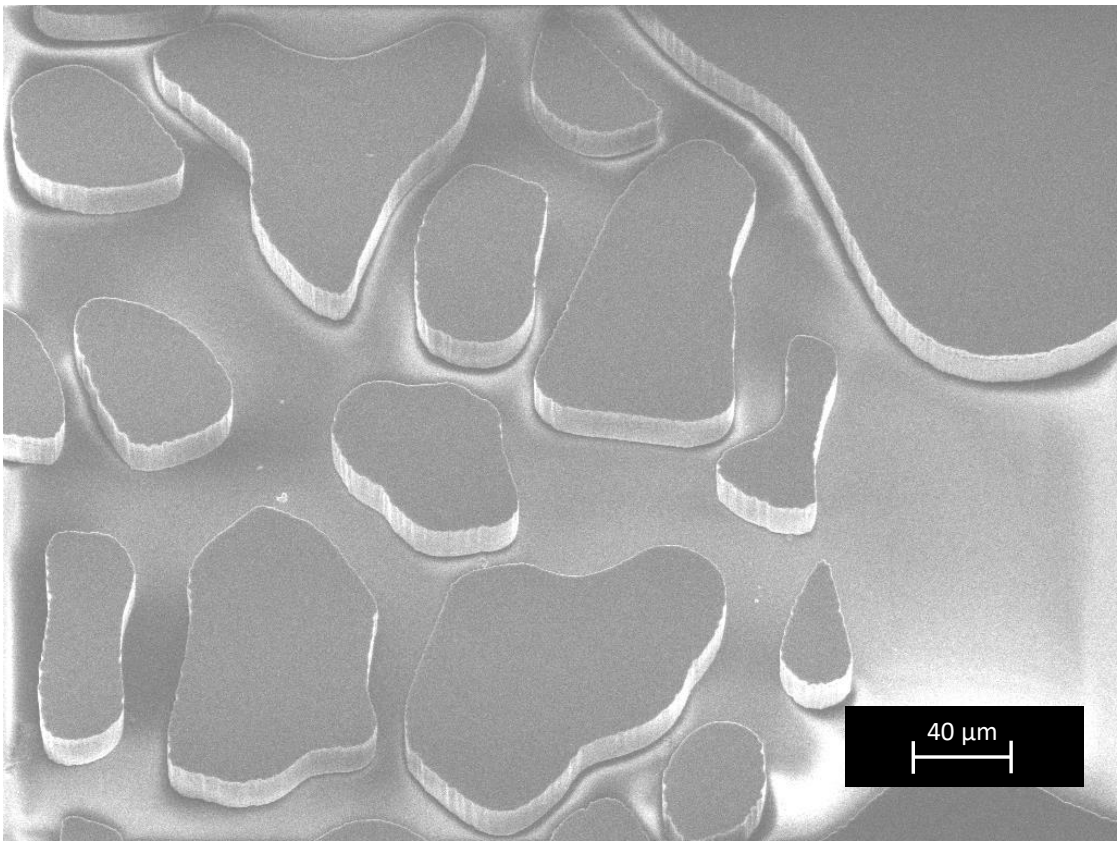


Figure 3.8: SEM image of the Case 3 heterogeneous micromodel sample showing the smaller and larger pores.

Experimental Setup and Procedure

One of the main goals of this research was to observe the drying process in different porous media and get insights of the drying characteristics, flow dynamics, and micro-macro flow interaction because of the varying pore size in the porous media.

To observe flow dynamics and track particles within the micromodel at two different levels of magnification, two separate microscopes were utilized in conjunction with the epi-fluorescence microscopy imaging technique. In the experimental setup illustrated in Figure 3.10 and 3.11, the microscope stage was positioned between the two microscopes. The lower microscope was an inverted one (Olympus IX-71), which was securely mounted on

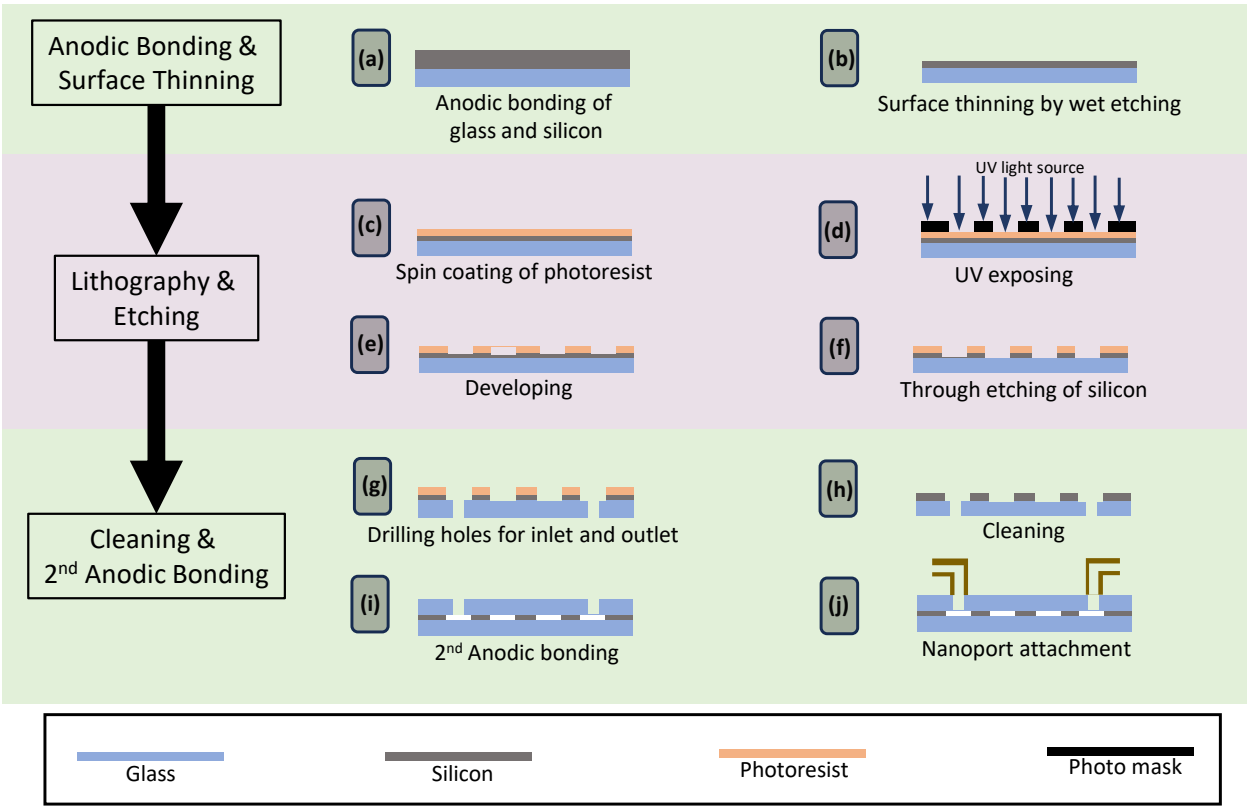


Figure 3.9: Schematic of the step-by-step procedure to fabricate three layers of glass-silicon-glass microfluidic device. Here different colors are defined for different materials at the bottom. (a) Anodically bond of 4-inch glass and 4-inch silicon wafers; (b) Reduction of silicon wafer thickness with KOH wet etching; (c) Spin coating of photoresist over the silicon wafer as one of the steps of photolithography; (e) UV exposing with the photomask to print the pattern on the silicon wafer; (e) Development of the photomask pattern on the silicon wafer with developer solution; (f) Dry etching of silicon to make channels and pores in the silicon wafer. Etching needs to continue to make the thorough etching of the silicon; (g) Drilling through holes with drill machine on the designated places to make the inlet and outlets; (h) Cleaning of the bonded wafers and another new glass wafer with Piranha solution to remove residue photoresist and other organic products. This step also transforms the silicon from hydrophobic to hydrophilic; (i) 2^{nd} anodic bonding to blend previously bonded glass-silicon wafer with another glass wafer to form glass-silicon-glass three-layer structure; (j) Attachment of nanoports at the inlet and outlet to connect the delivery lines firmly and provide flow through the micromodel.

an optical table equipped with active isolator legs. Conversely, the upper microscope was an upright variant (Olympus BX-61), and it was mounted on the lower microscope using

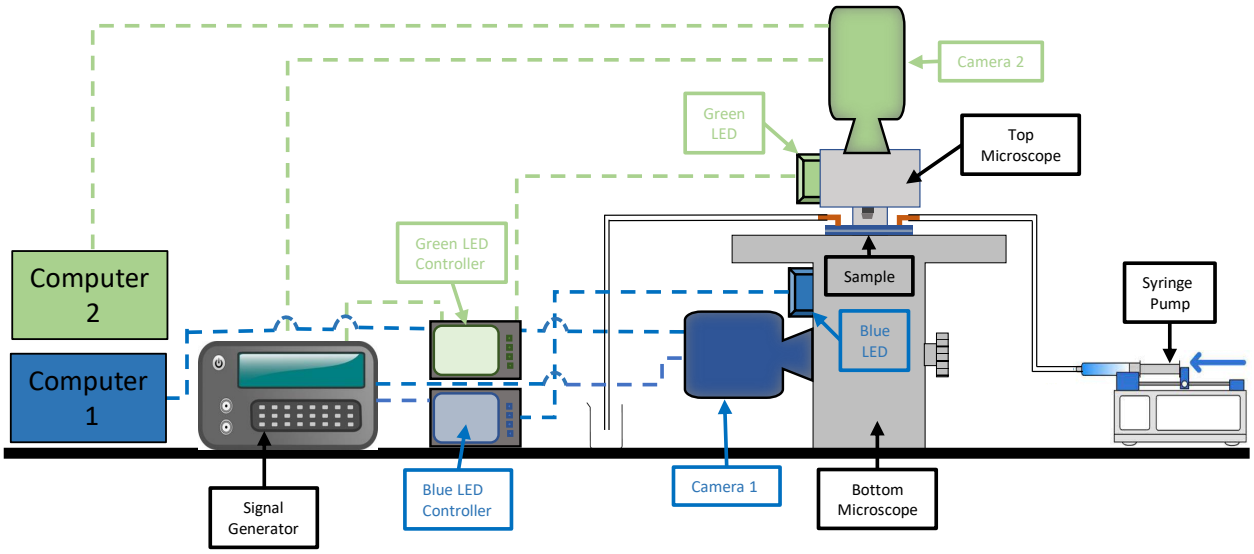


Figure 3.10: Schematic of the experimental setup for dual-magnification imaging.

custom-designed components considering various optical parameters (shown in Figure 3.13, 3.15, 3.18. Here, the components were meticulously fabricated in MSU Machine shop to ensure precise alignment of the microscopes. The primary challenge in the design lay in achieving the setup to comply with the tolerance of 5mm in each axis, adding a layer of complexity to the manufacturing process.

Each of these microscopes was equipped with its own LED light source, which was integral to the epi-fluorescence microscopy setup. The upper microscope was linked to a Complementary Metal-Oxide-Semiconductor (CMOS) scientific camera (Andor Neo 5.5), a green LED (Thorlabs SOLIS-525C M00569931), and a 2.5x objective (shown in Figure 3.12). The dynamic flow characteristics and patterns within the entire porous region were enabled to be captured by this configuration. Particle Tracking Velocimetry (PTV) technique was employed to investigate the flow interactions between micro and macro pores. For this purpose, the lower microscope was paired with a CMOS scientific camera (Phantom VEO 440), a blue LED (Thorlabs SOLIS-470C M00723531), and a 10x objective with 1.2x adaptor, which were used to track the movement of fluorescent particles within the field of view (FOV)

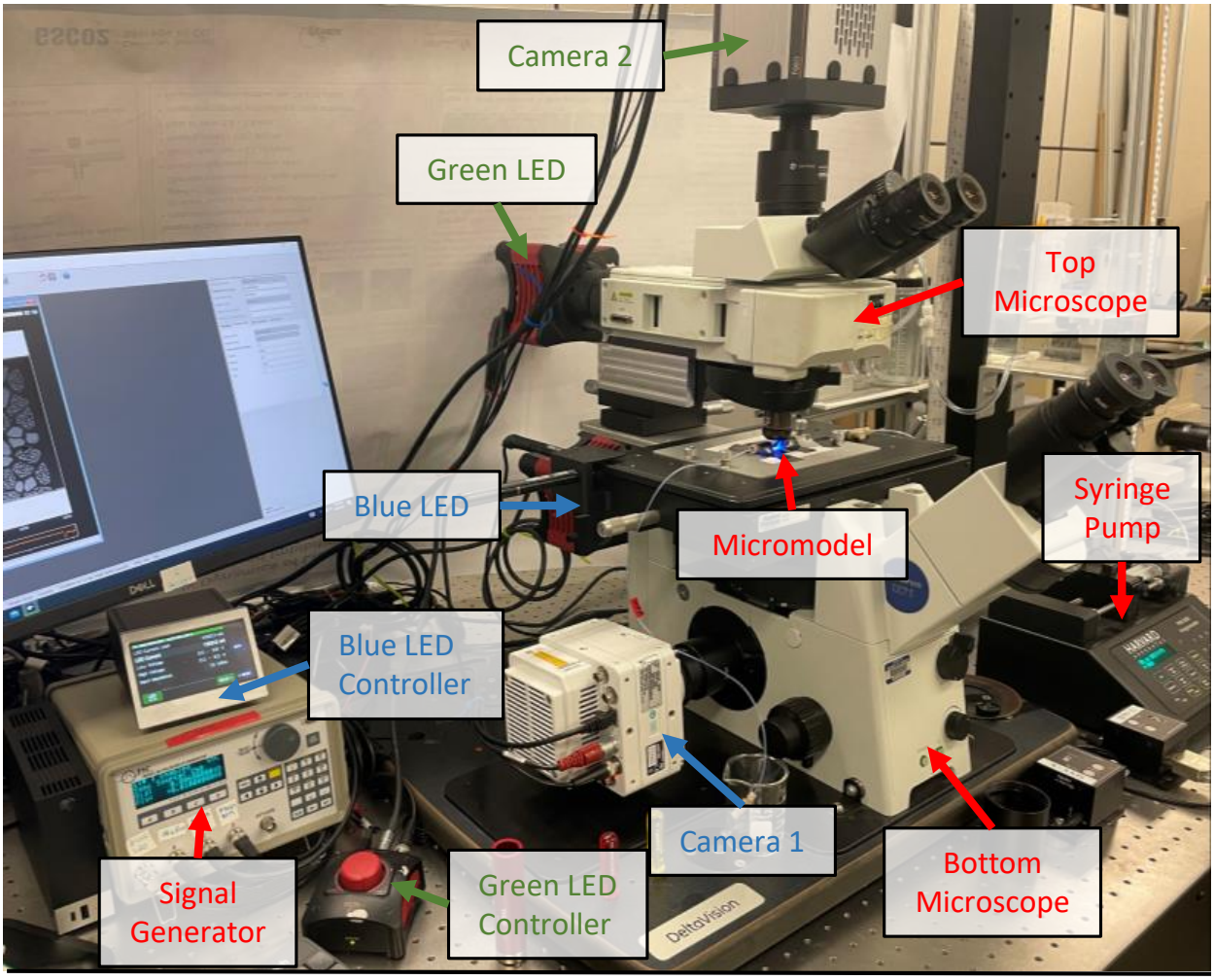


Figure 3.11: Actual image of the experimental setup with dual-magnification imaging capability.

of 1.6×1.17 mm^2. These cameras operated independently due to the incorporation of a signal generator as an external trigger within the system.

In this particular setup, two distinct LED light sources were employed, each equipped with its dedicated controller responsible for regulating both power and external triggering. Furthermore, the cameras, in conjunction with their respective light controllers, were linked to a central signal generator, as shown in Figure 3.10 and 3.11. This interconnected system ensured that all components operated seamlessly according to a predefined timeline,

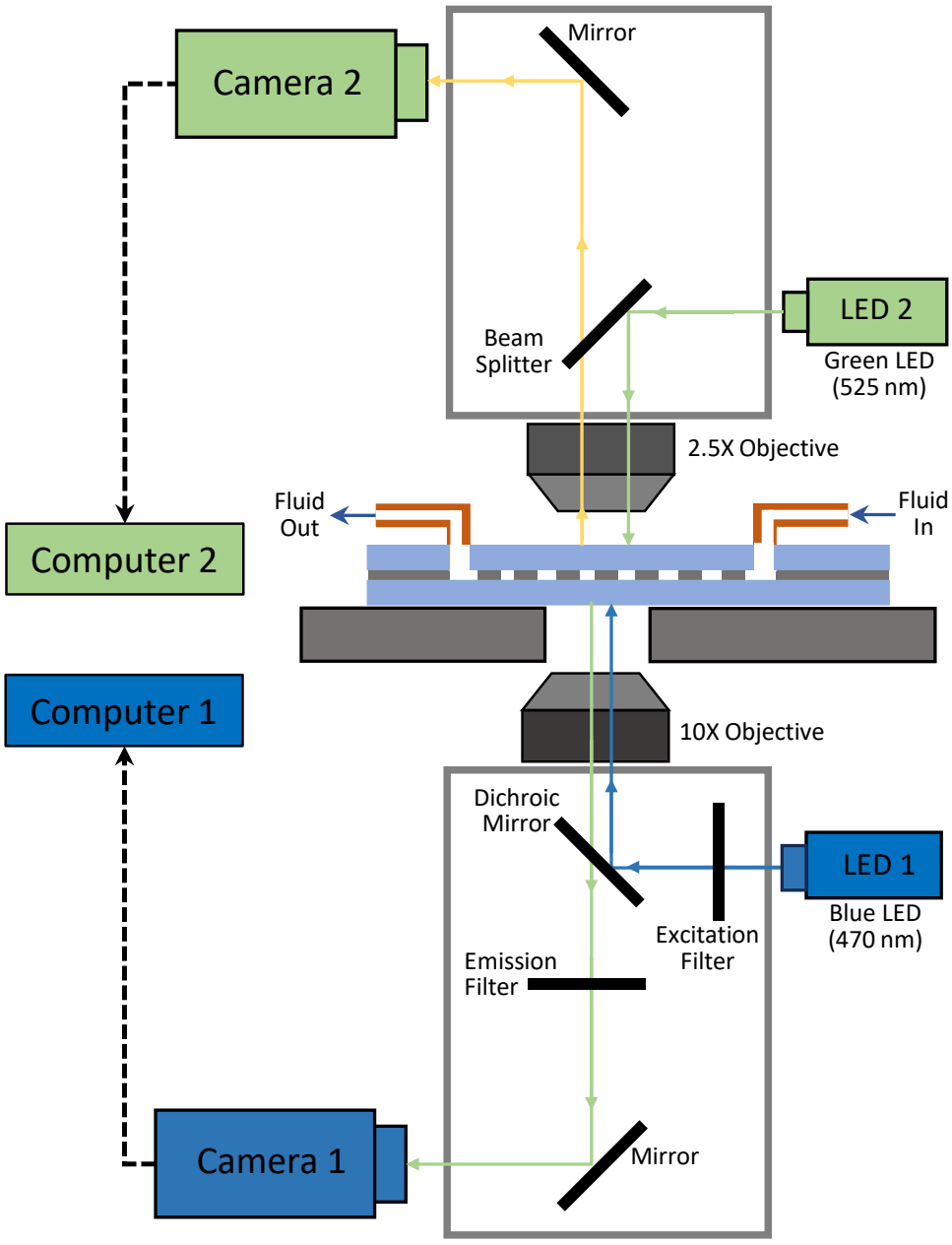


Figure 3.12: Optical setup for dual-magnification imaging applying epi-fluorescence microscopy and imaging technique.

providing assurance of synchronized operations.

To minimize the effects of photobleaching on tracer particles and dye, a sequential triggering system was implemented for each camera and LED set. This allowed for precise

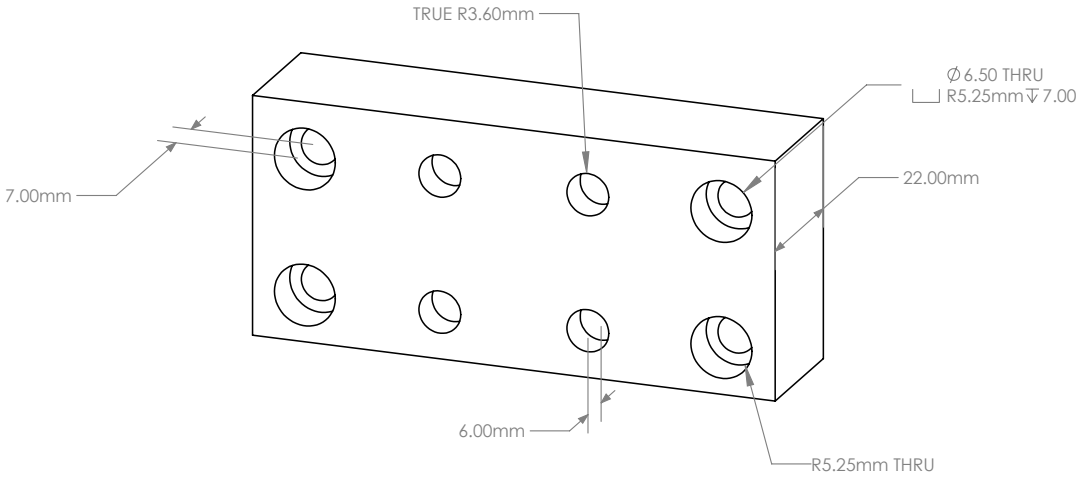


Figure 3.13: Isometric view of the custom-designed bottom mount to attach the top microscope and other parts with the bottom microscope with dimensions in mm.

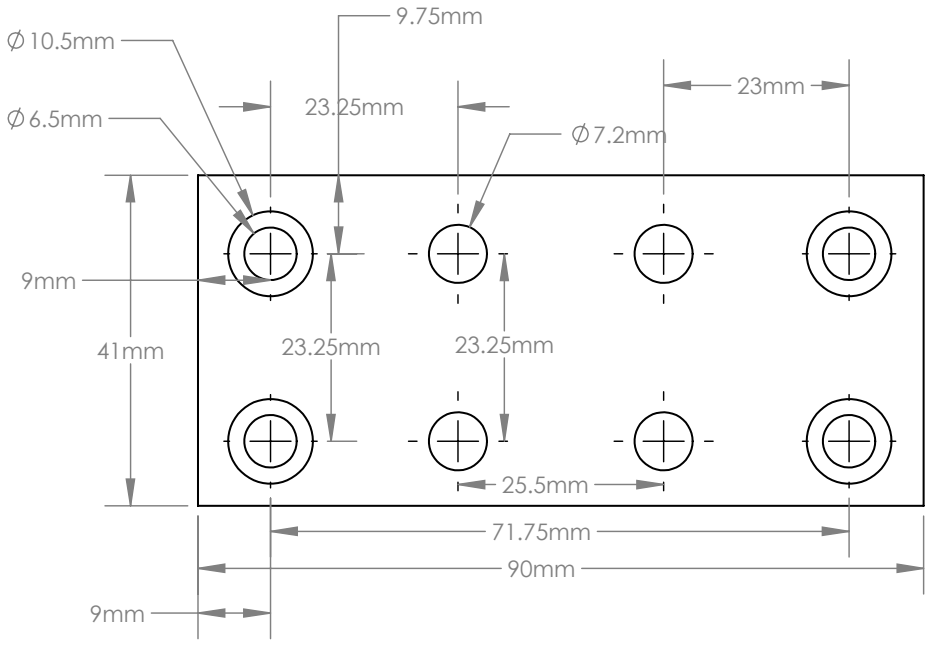


Figure 3.14: Top view of the custom-designed bottom mount to attach the top microscope and other parts with the bottom microscope with dimensions in mm.

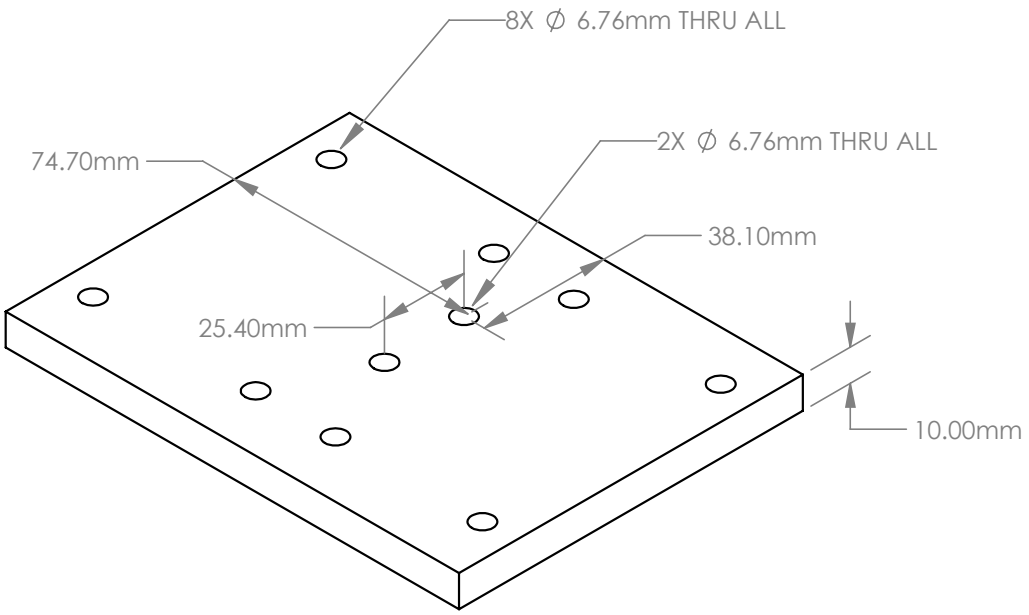


Figure 3.15: Isometric view of the custom-designed intermediate plate mount to attach the top microscope and other parts with the bottom mount (Figure 3.13) microscope with dimensions in mm.

control over the timing and pulse width of the excitation light, reducing the risk of overexposure caused by simultaneous LED activation.

The transparency of the micromodel posed a challenge as light passing through it would reach the other side of the micromodel, essentially the opposite microscope, and be reflected by the mirrors and excitation filter, leading to distorted images and unexpected shadows. To eliminate reflections originating from other side filters and mirrors, a meticulous selection of filters and dichroic mirrors was undertaken. These choices were made to ensure that the dichroic mirror would transmit the whole light coming from the other side of the micromodel to eliminate any undesired reflection.

The green LED with the top microscope emitted light with a wider field of view (FOV) because of the 2.5x objective, which passed through the micromodel and reached the bottom filter cube. However, there was a possibility of light reflecting off the bottom excitation filter

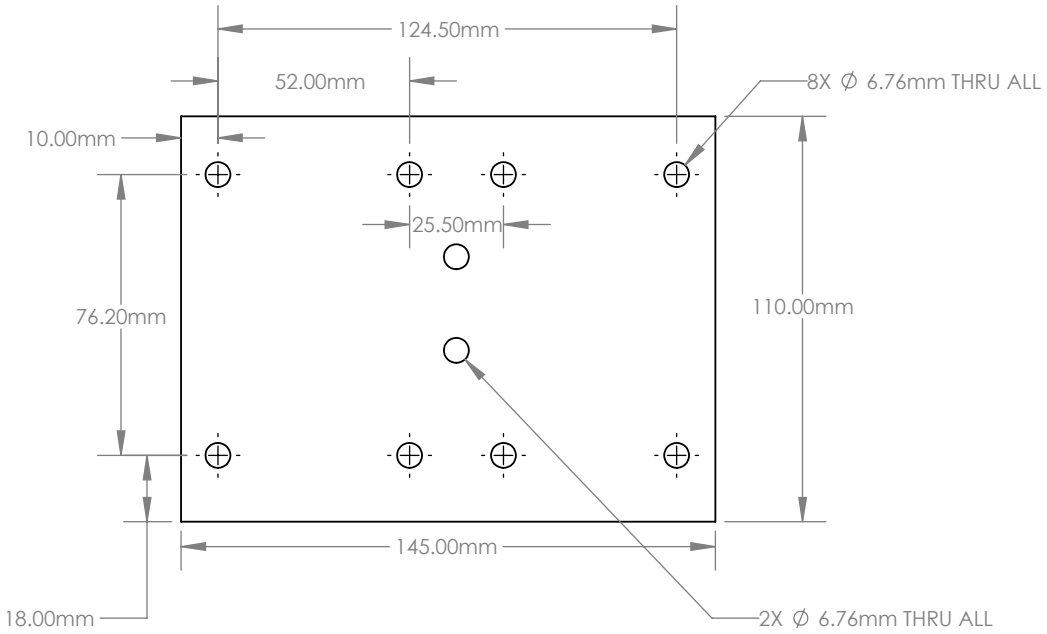


Figure 3.16: Top view of the custom-designed intermediate plate mount to attach the top microscope and other parts with the bottom mount (Figure 3.13) microscope with dimensions in mm.

because of the transmission range and interfering with the top camera. To mitigate this reflection, Fluorescein isothiocyanate (FITC) was utilized as a dichroic mirror in the bottom filter cube. This FITC mirror possessed a reflection band ranging from 470 to 490 nm and a transmission band spanning from 508 to 675 nm. As the light passing through the micromodel from the upper LED source had a wavelength of 525 ± 16 nm, it would be transmitted through the dichroic mirror of the bottom filter cube rather than reflecting. Overall, by implementing a sequential triggering system and carefully selecting filters and dichroic mirrors, the issue of overexposure and unwanted reflections was effectively addressed, enhancing the quality and reliability of the dual-magnification imaging technique used in this study.

To maintain a precise and constant flow through the micromodel, a syringe pump

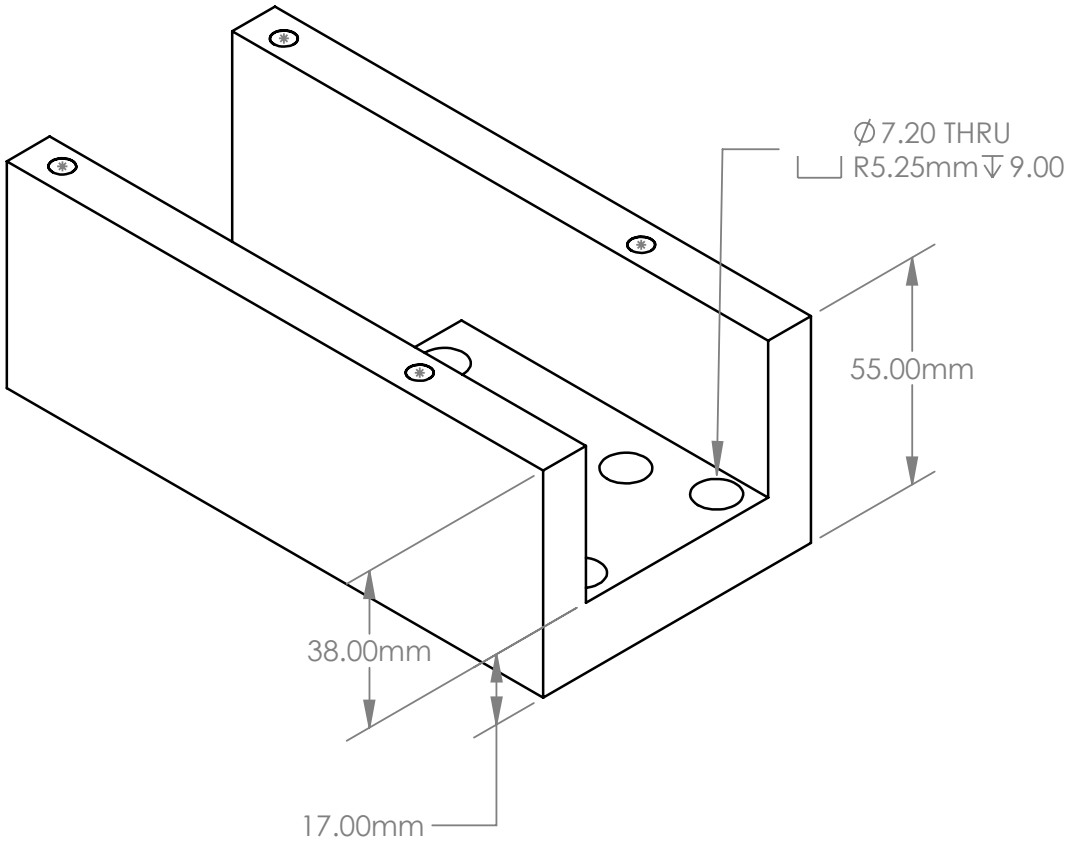


Figure 3.17: Isometric view of the custom-designed top mount to hold the top microscope and connect it with the translation stages and other bottom parts with the dimensions in mm.

(Harvard PHD 2000) was utilized. Teflon tubing was employed to establish the connection between the micromodel and the syringe. These tubing materials, known for their rigidity, facilitated accurate flow control.

Experimental Procedure

To initiate the experiment, the micromodel was initially saturated with a solution comprising a mixture of Deionized Water (DI water), Fluorescein sodium salt (Fluorescein Dye), and tracer particles. Fluorescein sodium salt, denoted as Fluorescein tracer, possesses a

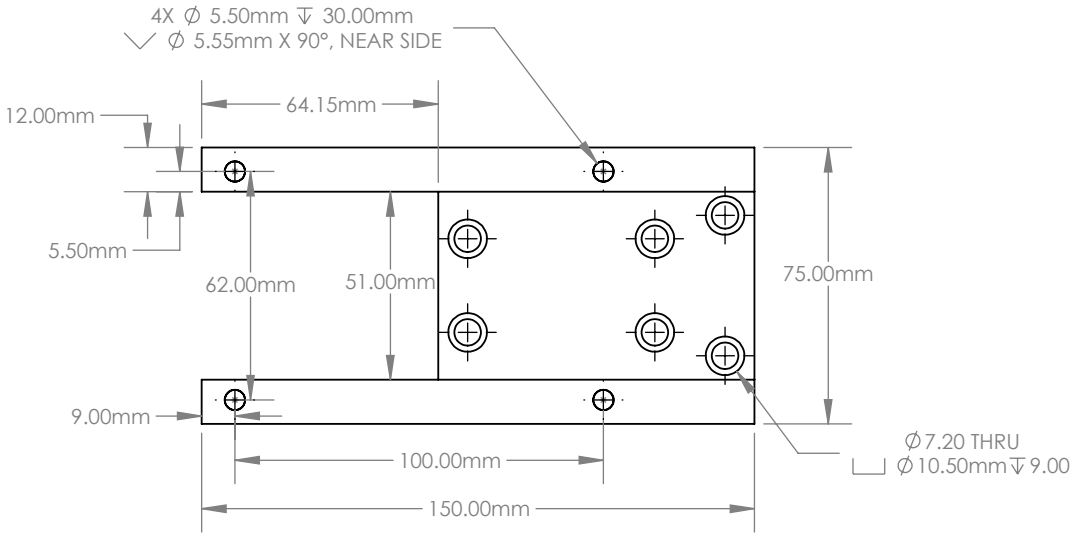


Figure 3.18: Top view of the custom-designed top mount to hold the top microscope and connect it with the translation stages and other bottom parts with the dimensions in mm.

molecular weight of 376.27. Its optical properties include an excitation wavelength of 460 nm and an emission wavelength of 515 nm. The concentration of Fluorescein dye in the solution was precisely maintained at 30 μM. The primary objective of incorporating Fluorescein dye into the solution was to facilitate the differentiation of liquid and vapor phases, as well as the identification of grains within the micromodel at the time of capturing images. To monitor fluid motion within the micromodel, FluoSpheres Carboxylate tracer particles of 2.0 μm diameter were employed. For these experiments, 4 μl of tracer particle was used for every 1 ml of DI water-dye solution because of the possibility of particle accumulation ahead of drying at the pore throats.

To conduct the experiments, the porous region and channel were initially saturated entirely with the wetting phase, (*i.e.*, DI water). Following this saturation phase, micromodels went through a drainage process utilizing the nonwetting phase (*i.e.*, ambient air) injecting through the inlet. The flow of air was meticulously controlled using a syringe connected to the inlet with Teflon tubing. The syringe injected air at a constant flow rate

set at 0.1 ml/min, facilitated by a syringe pump. This controlled airflow effectively drained water from the channel establishing a distinct phase configuration at the water-air interface, and subsequently started drying within the porous region.

The relative humidity of the air was not controlled in these experiments. Relative humidity varied during the experiments within a range of 18% to 30%. However, the humidity condition for the injected air was maintained constant throughout the experiment, as the syringe was not refilled for the second time during the drying process.

Image Acquisition and Processing

The recording of the drying process started following the drainage period, with the cameras capturing the events synchronized at a rate of 1 or 0.5 frames per second. Grayscale images were acquired by the cameras at different magnifications and were stored on two separate computers due to system requirements. The camera with lower magnification was used to capture the flow dynamics of the entire porous region, while the higher magnification camera focused on the tracer particles to track the motion in a specific area during the drying process. The images captured by the lower magnification camera were processed using ImageJ and in-house MATLAB code, enabling the extraction of valuable insights for the entire porous region. Dynamic thresholding technique was applied to account for variations in illumination and to effectively separate the phases of water, air, and grains. Finally, segmented images were utilized to calculate the saturation and determine the saturation profile at different times.

On the contrary, for the visualization of flow and comprehension of pore-scale physics, Particle Image Velocimetry (PIV), particularly the micro-PIV method, was employed. The focal plane of the microscope's objective lens served as the measurement plane, and particles were utilized to trace the flow. To minimize particle slip, careful selection of an appropriate fluorescent tracer particle was essential. In this experiment, spherical particles with a

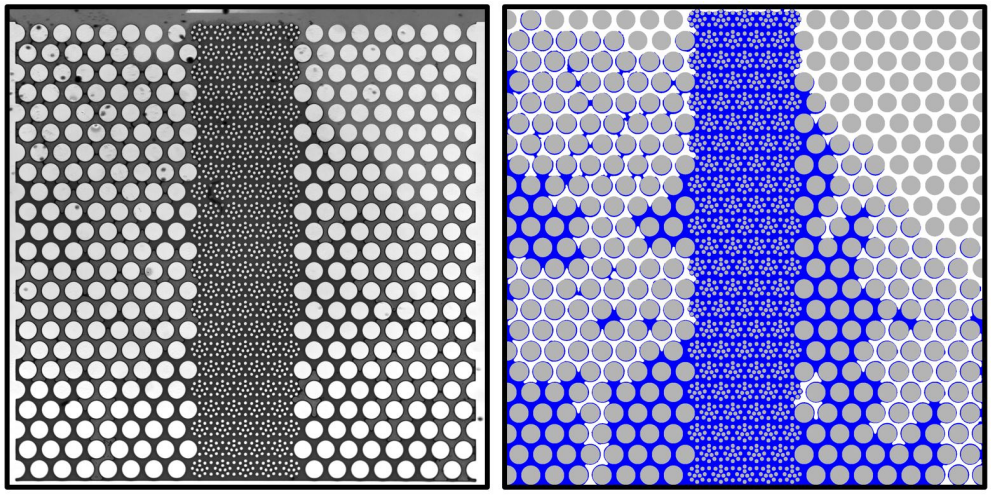


Figure 3.19: (a) A raw image captured with the lower magnification camera; (b) Processed segmented image of the image captured with the lower magnification camera. Blue, white, and grey in the figure correspond to the water, air, and solid grains, respectively.

diameter of 2 μm were used, possessing a density similar to DI water, which significantly reduced slip. The spherical shape ensured that acquired images were independent of particle rotation, and the center of the particle image corresponded to the center of mass of the particle.

In our experiments, depth of field of the objective was larger than the micromodel channel thickness which enabled all tracer particles to be focused within the Field of View (FOV). Optimized LED light intensity and camera exposure time were selected to enhance particle visibility, reduce noise, and minimize photobleaching. Lower camera exposure was applied to mitigate particle striping. It's noteworthy that, due to the low particle density, this process is also referred to as Particle Tracking Velocimetry (PTV) [2], where the mean spacing of particles surpasses their mean displacement.

Subsequently, the images underwent processing through MATLAB scripts. The fundamental purpose of these codes was to determine the displacements of numerous particles

accurately tracking the motion of the fluid over time across the entire FOV. Initially, images with particles were enhanced for visibility and noise reduction. By filtering, noises, and undesired deposited and clogged particles were removed and particles were separated from the background. Because of having sparse distribution of particles, segmentation was employed to track individual particles along with their centroids. The displacement and time increment were then calculated from the series of segmented images to determine the velocity, providing insights into the flow interaction between micro- and macro-pores during the drying process.

CHAPTER 4 DRYING OF POROUS MEDIA DRIVEN BY DIFFUSION

This chapter elucidates the outcomes derived from the investigation into drying phenomena, with a particular focus on the characterization of drying incidents in two distinct cases involving water and air as the working fluids for Case 1 and Case 2 micromodels. This result section emphasizes a comprehensive understanding of the drying characteristics across the entire porous region, utilizing a lower magnification camera for image capture.

In the experiments, the porous region and channel were initially saturated entirely with the wetting phase, (*i.e.*, DI water). Following this saturation phase, the channel and the top part of the porous region underwent a drainage process, where the water phase is instantly displaced by the nonwetting phase (*i.e.*, ambient air). The flow of air was meticulously controlled using a syringe connected to the inlet with Teflon tubing. The syringe injected air at a constant flow rate of 0.1 ml/min, facilitated by a syringe pump. This controlled airflow effectively drained water from the channel establishing a distinct phase configuration at the water-air interface, and subsequently started drying within the porous region.

The relative humidity of the air in the syringe was recorded at a range of 18% to 30%, and this condition for injected air was maintained throughout the experiment. The recording of the drying process commenced when any location within the porous region initiated drying, with cameras capturing the events at a rate of 0.5 frames per second. Greyscale images were captured with a lower magnification camera and were processed in MATLAB employing the dynamic threshold technique.

Drying in Porous Media for Case 1

Figures 4.1 and 4.2 show the evolution of the water phase (*i.e.*, blue) for Case 1 during the drying process at different times. In the figures 4.1 and 4.2, blue, white, and grey in the figure correspond to the water, air, and solid grains, respectively. Again herein, air flows from right to left in a main channel which sits right on top of the porous section.

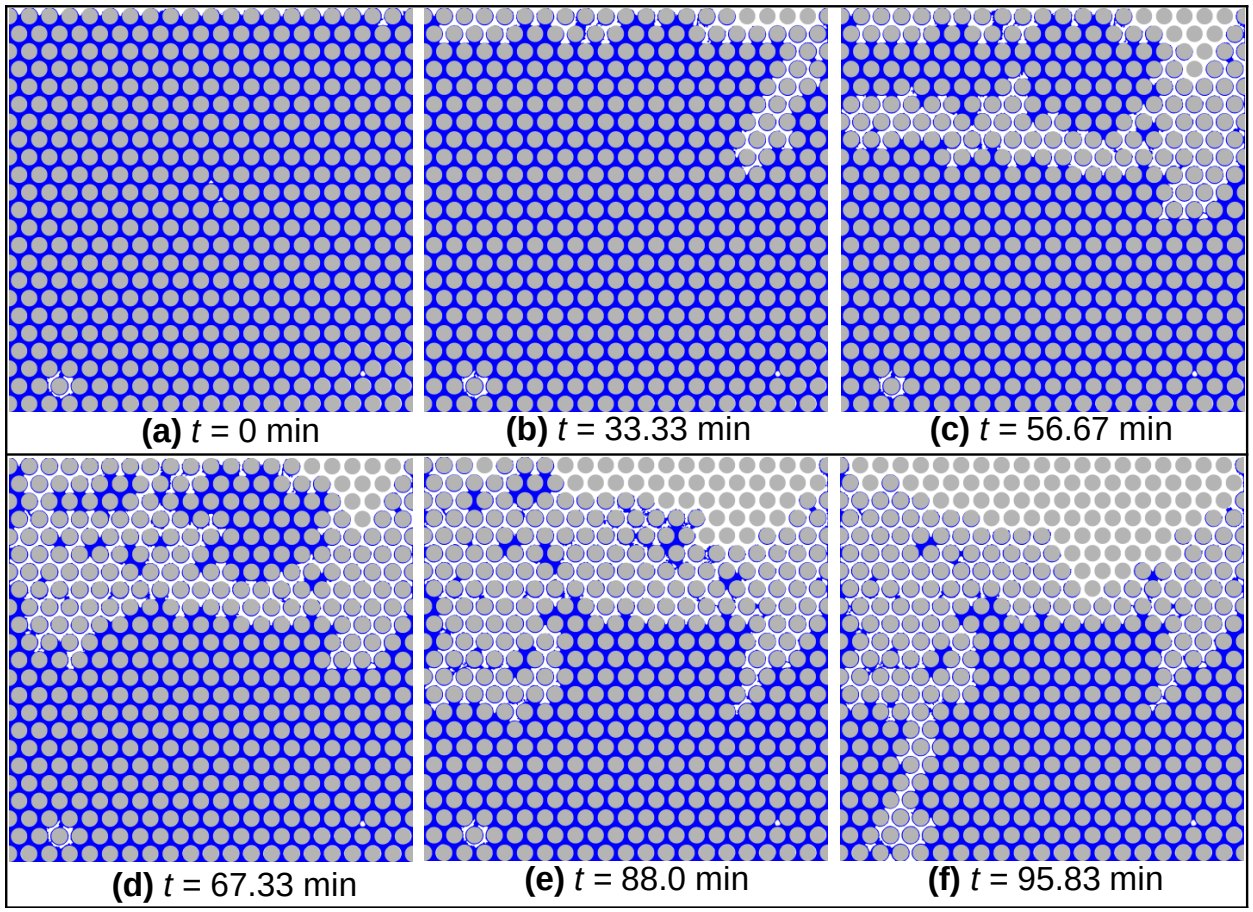


Figure 4.1: Saturation Distribution during drying of Case 1 homogeneous micromodel at (a) $t = 0$ min; (b) $t = 33.33$ min; (c) $t = 56.67$ min; (d) $t = 67.33$ min ; (e) $t = 88.0$ min; (f) $t = 95.83$ min. Blue, white, and grey in the figure correspond to the water, air, and grain respectively.

Following the initial drainage of the wetting phase from the main channel, the channel first dries due to contact with unsaturated air from the inlet. During this stage, the

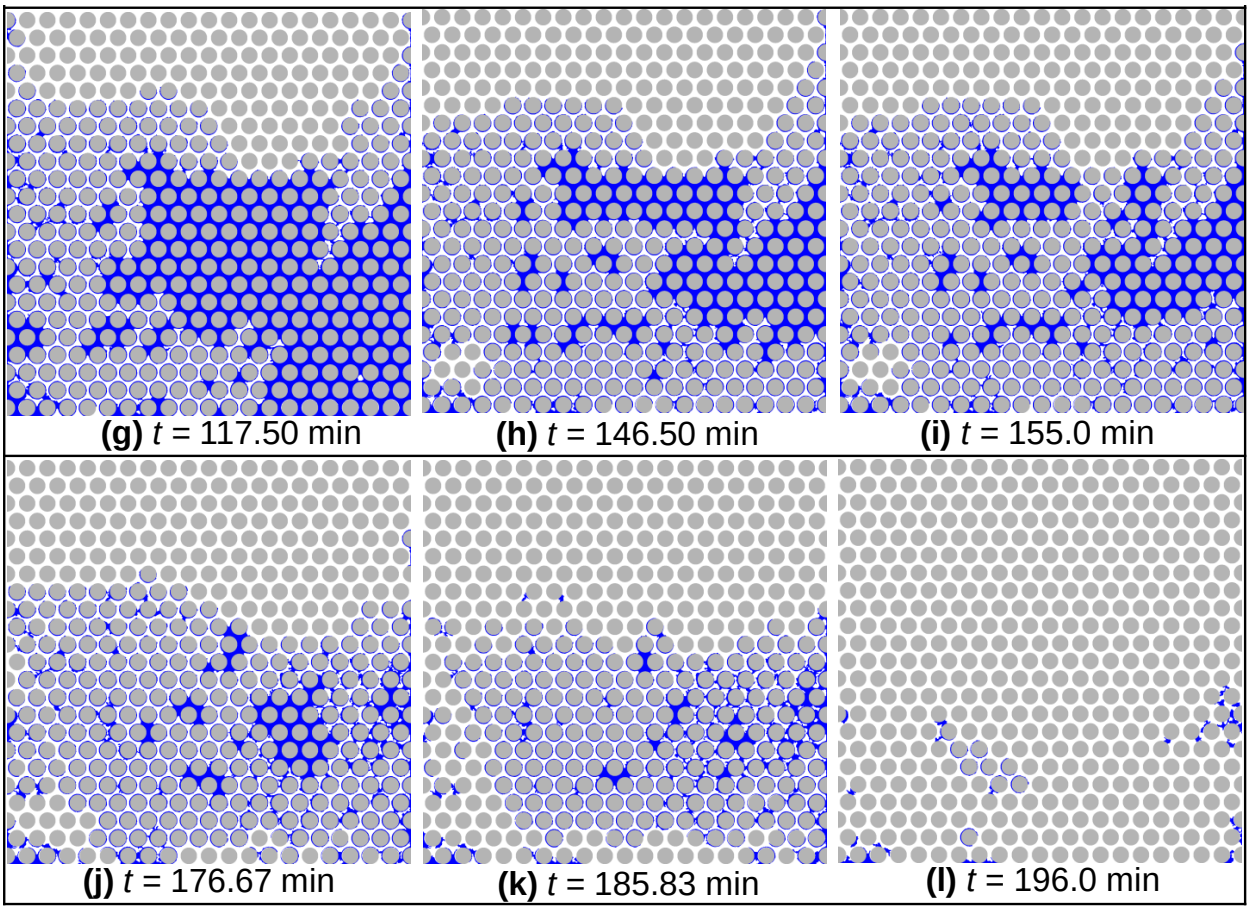


Figure 4.2: (Continued from Figure 4.1) Saturation Distribution during drying of Case 1 homogeneous micromodel at (g) $t = 117.50$ min; (h) $t = 146.50$ min; (i) $t = 155.0$ min; (j) $t = 176.67$ min; (k) $t = 185.83$ min; (l) $t = 196.0$ min. Blue, white, and grey in the figure correspond to the water, air, and grain respectively.

unsaturated air picks up moisture near the inlet first, becomes saturated, and exits through the outlet without affecting the porous region until the channel dries up completely to the right edge of the porous region. Once the dry front reached the right edge of the porous region, the gas phase started invading the top right corner. Image acquisition started at this time, which is set as time zero, $t = 0$ (Figure 4.1a).

Due to the fact that the air flow comes in from the right side of the main channel, air invasion persisted at the top-right corner of the porous region, concurrently leading to the

drying of the channel and the advancement of the drying front towards the left. As the channel dried up, numerous locations at the top of the porous region experienced invasion, continuing the drying of the pores closer to the channel. During this invasion, air invades the pore spaces at the right edge of the porous region and proceeds towards the bottom for a brief period before changing its direction to the left in the form of so-called fingers. This process is induced by inherent flow instability as the invading phase, air is much less viscous than the resident phase, water herein, which is turn governed by the combined effect of viscous and capillary forces (Figure 4.1b and c). This invasion continues until the front of the invasion reaches the left edge of the porous region, exposing the interface to the channel by trapping water in the middle region (Figure 4.1c and d). It is worth noting that at this moment, although the trapped water ganglion in the middle domain appears to be disconnected from the rest of the water regions, it in fact remains connected through corner flows and thin films. Drying continues both at the interface of the trapped water and the interface in the middle of the porous region. The upper portion completely dried, including the corner films at t= 95.83 min.

Upon the complete drying of the upper portion of the porous region and the advancement of the drying front, the invasion continued at the bottom. It is interesting to note that a corner film persists at the top right edge (Figure 4.2i). This can be attributed to two causes: 1) a stronger corner flow is expected along the side wall; 2) the air flow is directed from right to left over the porous section, effectively forming a dead space next to the right vertical wall, causing a faster invasion of the pores at the left side of the porous media compared to the right edge. The invasion continues until the very bottom of the porous region from the left edge. Due to instability, the invasion continues in different directions, and the upper region of the porous section remains dry. As the air was directed towards the left edge, that portion completely dried first (Figure 4.2k), and this drying continued for the entire bottom region. The entire micromodel completely dries after 204 minutes.

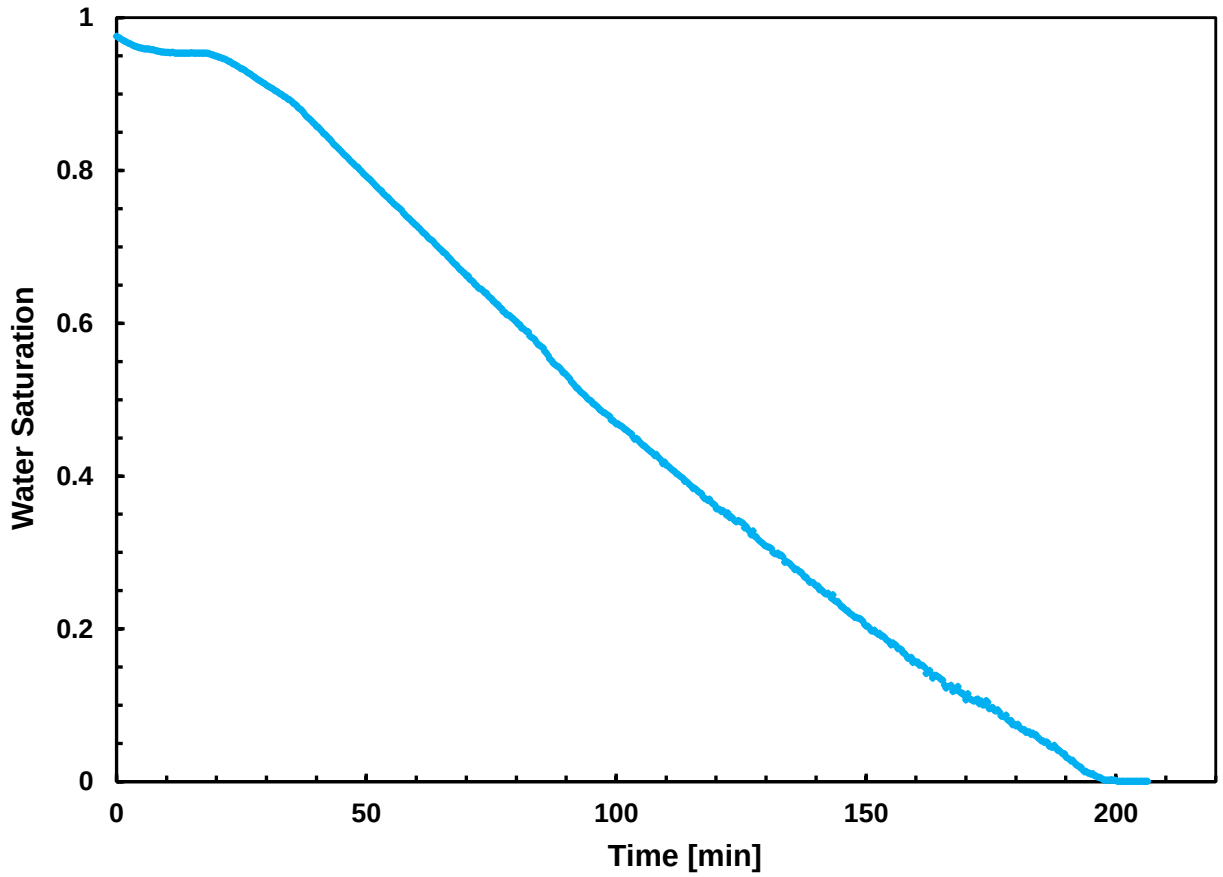


Figure 4.3: Water saturation variation over time in the drying process of Case 1 homogeneous micromodel. Time is presented in minutes on the x-axis.

Figure 4.3 presents the quantitative variation of the water saturation over time for the Case 1. As expected, after a short starting-up period, the water saturation continuously decreases with time, consistent with a drying process. The slope of this graph, presented in Figure 4.4, represents the water drying rate in units of s^{-1} as a function of time. It can be seen that the slope of the water saturation curve decreases over time, indicating a decreasing drying rate over time.

Figure 4.4 shows the drying rate of the water phase, which is calculated based on the data shown in Figure 4.3 using a simple finite difference technique. It can be seen that the drying rate is initially very low, corresponding to the starting up period, which is in turn

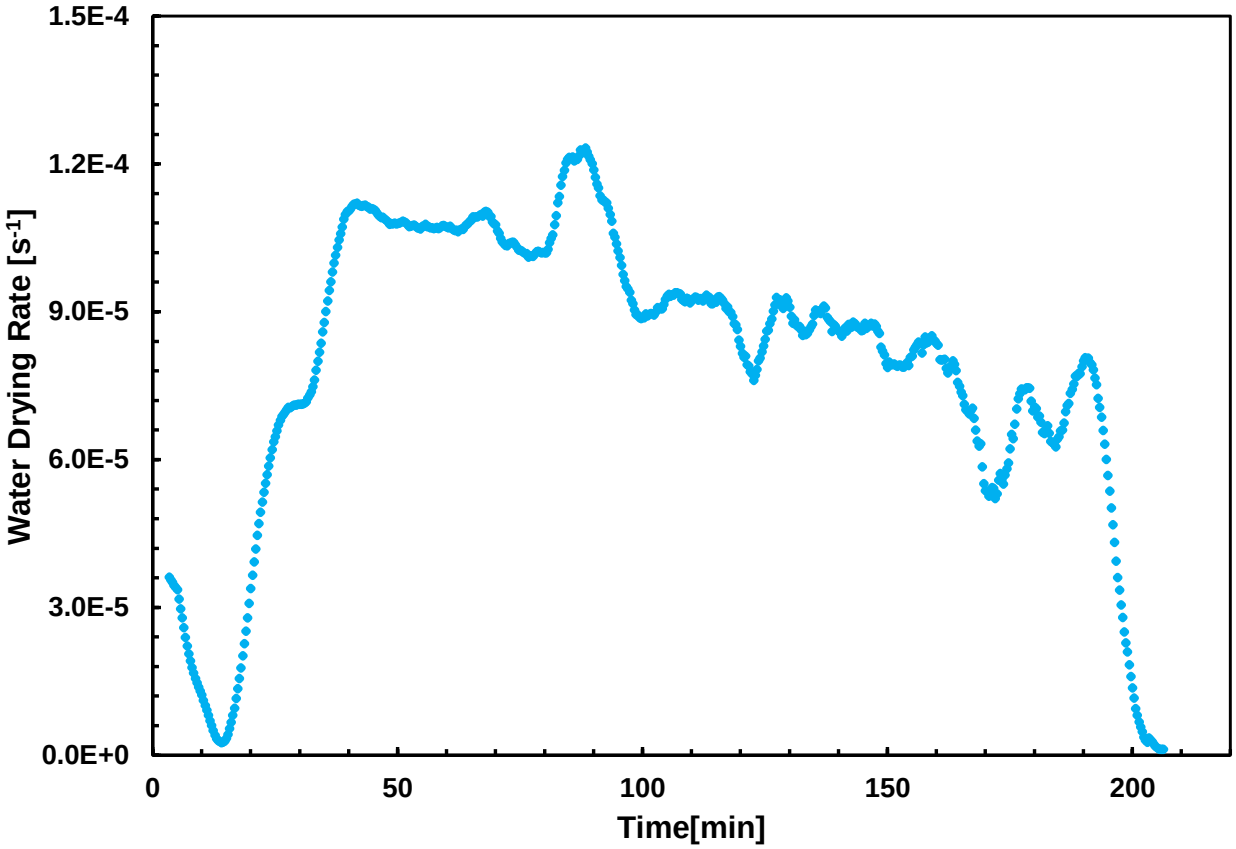


Figure 4.4: Water drying rate variation over time in the drying process of Case 1 homogeneous micromodel. Water drying rate is presented in the unit of s^{-1} and Time is presented in minutes.

because the main channel above the air-water interface is still not completely dry. As drying progresses at the interface, the drying rate increases, entering the main drying period. At this stage, despite the peaks and troughs in the curve, the overall drying rate displays a declining trend over time. This is expected. As drying progresses, the drying front moves down towards the bottom of the porous region, increasing the resistance for water vapor to diffuse upward to the main channel, where it is carried away by the flow of air, and thus the drying rate gradually decreases. This period, although with a slow decline rate, is often referred to as a constant rate period. The peaks and troughs in the curve, on the other hand, are presumably due to the sudden movements of the interfaces through the

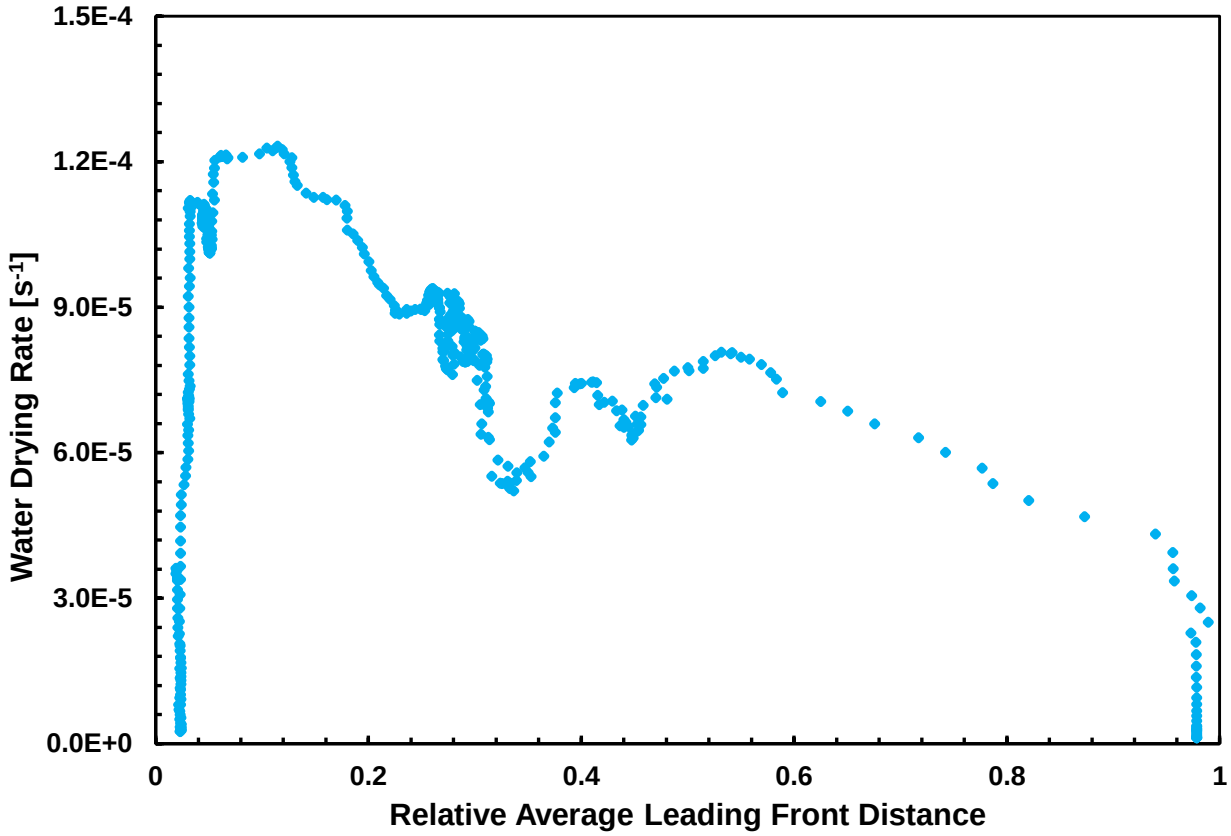


Figure 4.5: Water drying rate variation with relative average leading front distance in the drying process of Case 1 homogeneous micromodel. Water drying rate is presented in the unit of s^{-1} and the relative average leading front distance is measured from the top edge of the micromodel porous region.

pores and throat during the percolating process, causing re-distributions of the water phase and possibly inducing a water flow towards the outlet of the main channel. It is worth noting that, these abrupt interface movements, terms burst events or Haines jumps, have been observed in many previous experiments of multiphase flow in porous media. They are primarily due to the imbalance of capillary pressures in a pore throat and the open pore space. For instance, when a meniscus resides next to a pore throat, the curvature of the meniscus and thus the capillary pressure across the interface is high due to the geometrical constriction, thus storing a high level of free surface energy in the meniscus. As drying

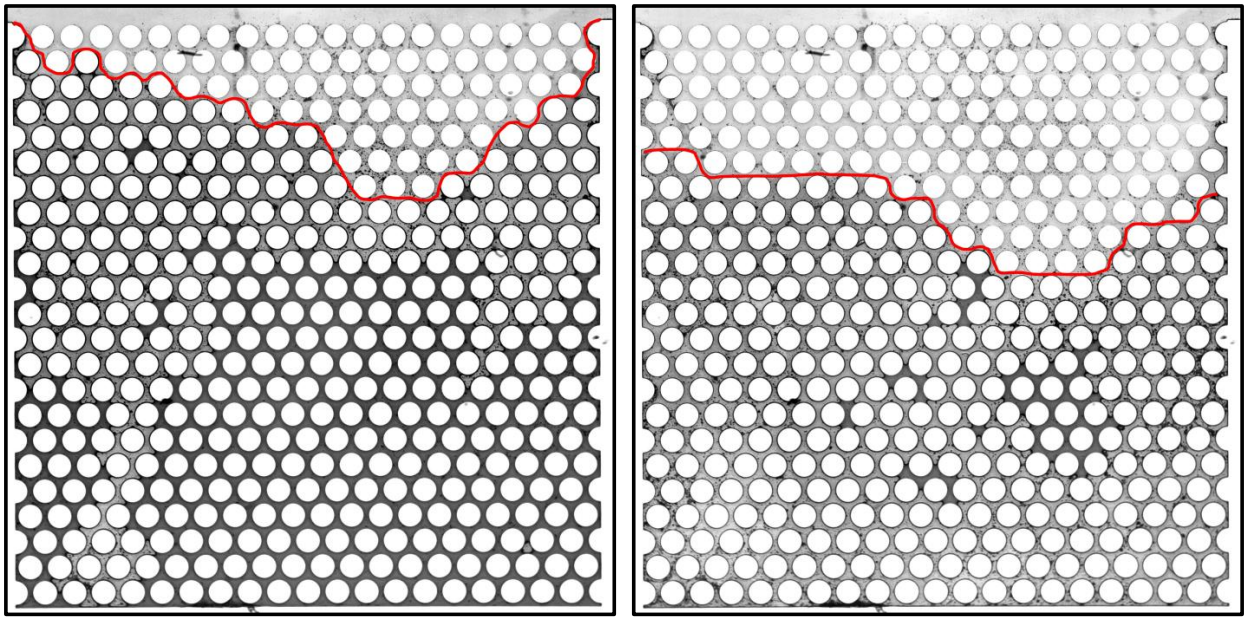


Figure 4.6: Leading or dry front location for Case 1 homogeneous micromodel during drying at (a) $t = 95.83$ min; (b) $t = 176.67$ min. The leading front boundaries are marked with red lines. Water and film layers are identified in the figure as deep black and grey respectively.

progresses, the meniscus eventually passes the throat region, entering a much open space in a pore, which causes a sudden release of the surface energy in the form of kinetic energy, leading to a rapid movement of the interface. Following this period, there is a sharp decline in the drying rate, identified as the falling rate period. In this phase, the film layer disappeared, and drying was solely controlled by the diffusion-driven mass transport process.

Figure 4.5 depicts the drying rate as a function of the location of the leading front. The relative average leading front distance was measured from the top edge of the micromodel porous region as shown in Figure 4.6. It can be seen from Figure 4.5 that the drying rate is highly correlated with the drying front location. With the exception of the starting-up period, the drying rate consistently decreases as the drying front recedes deeper into the porous section. The correlation coefficient between the drying rate and the drying front location is calculated to be 0.71. The strong dependence of the water drying rate on the

drying front location suggests the drying process in Case 1 is highly diffusion-controlled. These figures provide insights into the reasons for the variation in drying rate over time.

Drying in Porous Media for Case 2

Figures 4.7 and 4.8 show the evolution of the water phase saturation with time for Case 2, which features a micro-porosity region and two macro-porosity regions. Again, in the figures 4.7 and 4.8, blue, white, and grey in the figure correspond to the water, air, and solid grains, respectively. Similar to Case 1, the gas phase starts invading the top right corner at the initiation of recording, denoted as $t = 0$ min (Figure 4.7a). Unlike Case 1, however, while invasion of the air phase progresses in both macro-pore regions, with a more extensive penetration of fingering observed in the left macro-pores compared to the right macro-pores (Figure 4.7c), the micro-pore region in the middle remains saturated. This phenomenon is attributed to capillary pumping, which draws water from the macro-pores to the micro-pores. Another thing that is visibly different from Case 1 is that the drying rate was notably higher in the right macro-pores compared to the left ones (Figure 4.7e,f,g). This is because the micro-pore region in the middle, which is saturated with water, presumably blocks the air from flowing right to left, and significantly reduces the exposure of the left region to air. At $t = 73.20$ min, the upper portion of the right macro-pore region completely dries. At $t = 149.80$ min (Figure 4.8h), the majority of water in the macro-pore region dries out and the micro-pore region just starts to dry.

At $t = 153.53$ min, despite trapped water and corner films in macro-pores, invasion started in the top micropores region. Here, air invaded the pores between two rows of micropore, notably in the relatively larger pores of this micro-pore region (Figure 4.8h). Invasion was also initiated in the bottom row of the micropore region at $t = 153.53$ min, with the invasion continuing in micropores closer to the channel. At $t = 166.83$ min, the pores between the two micropore sets dries, and the micropores begin drying (Figure 4.8i).

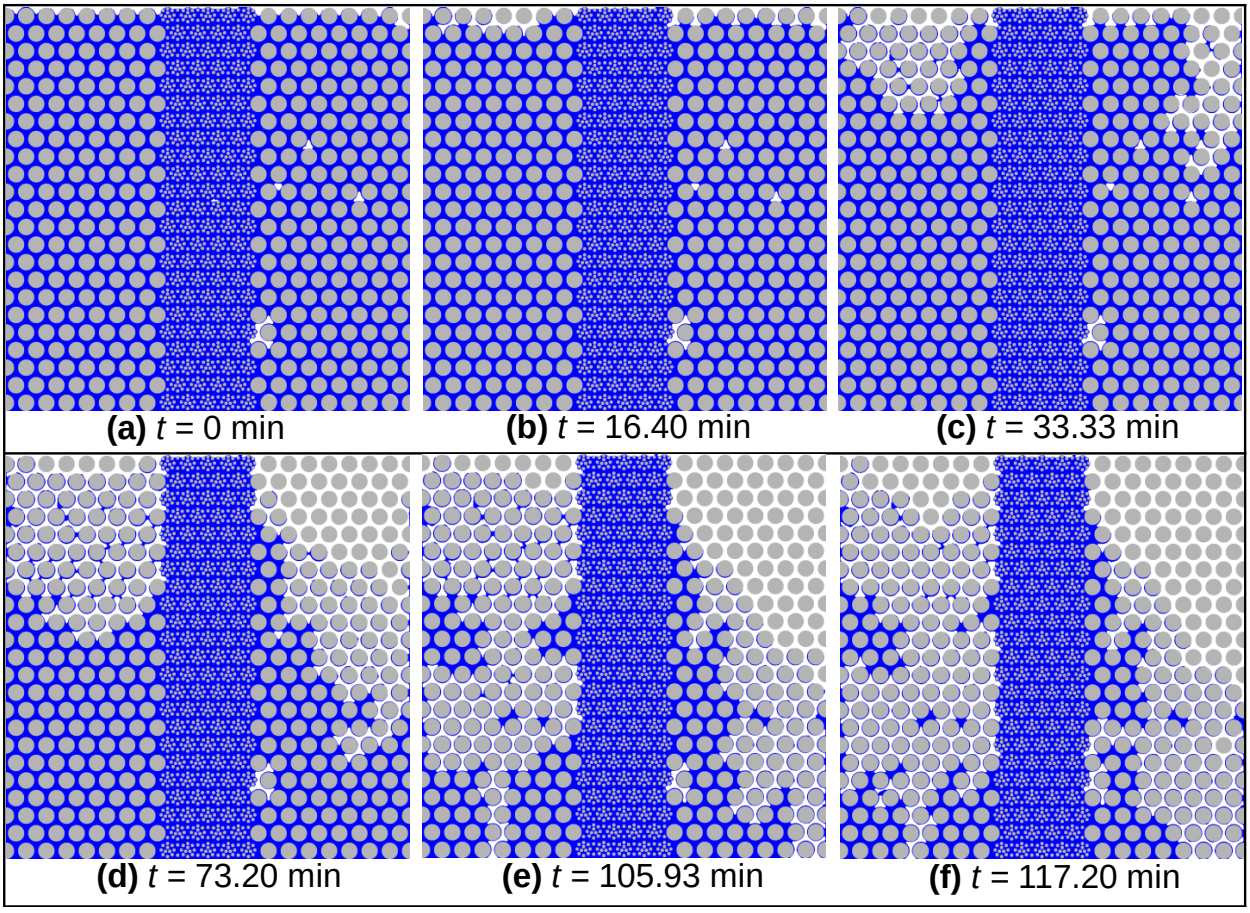


Figure 4.7: Saturation Distribution during drying of Case 2 dual-porosity micromodel at (a) $t = 0$ min; (b) $t = 16.40$ min; (c) $t = 33.33$ min; (d) $t = 73.20$ min ; (e) $t = 105.93$ min; (f) $t = 117.20$ min. Blue, white, and grey in the figure correspond to the water, air, and grain respectively.

At this stage, the surrounding macro-pores of the drying micropores completely dry, and the water films recede towards the bottom (Figure 4.8j and 4.11). Drying also occurs at the bottom alongside the top micropores, albeit at a significantly slower rate (Figure 4.8k, l).

Figure 4.9 presents the variation in water saturation over time for Case 2. Again the water saturation continuously decreases with time, as expected for a drying process. The first portion of the curve displays a largely linear relationship, whereas the second half of the curve shows some non-linear behavior with a decreasing slope. Figure 4.10 shows the

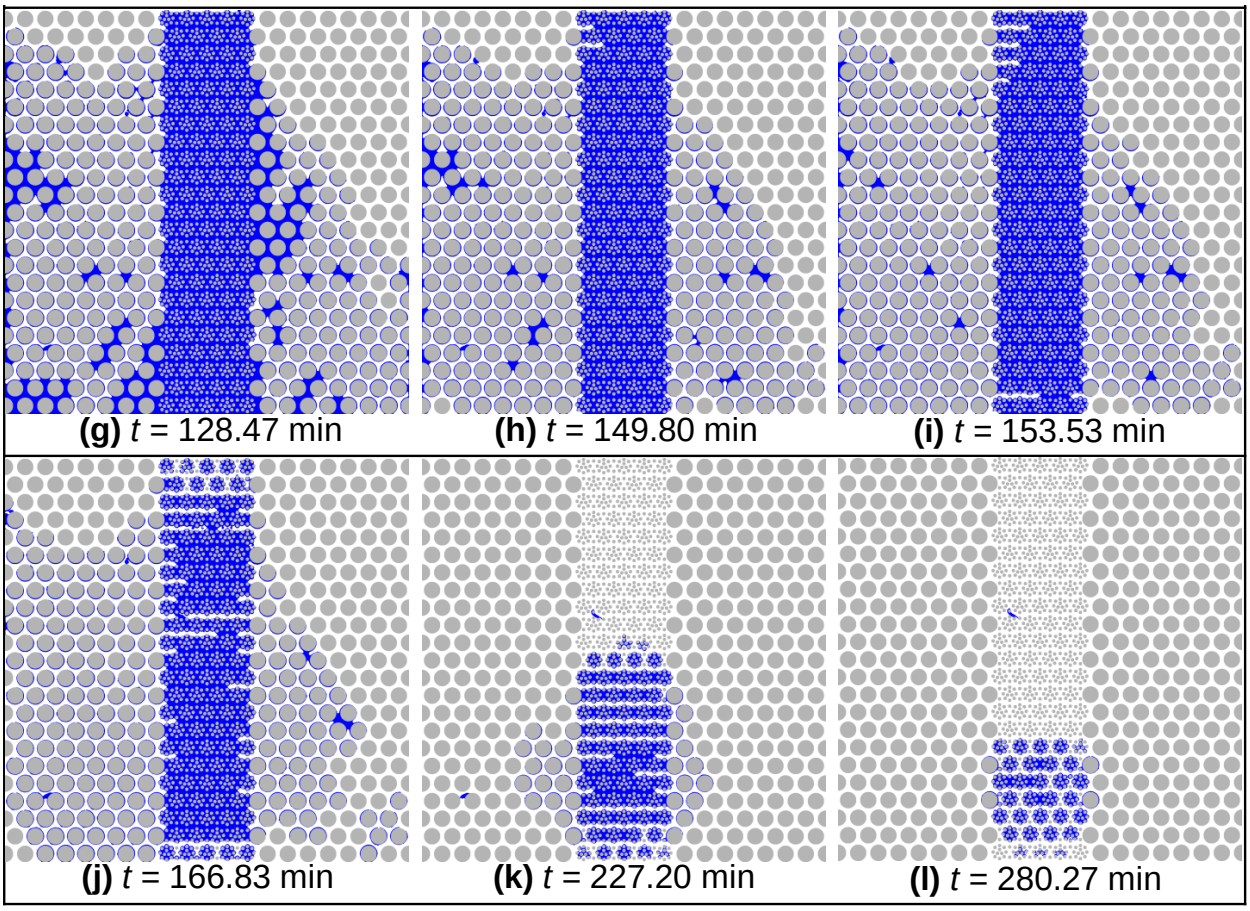


Figure 4.8: (Continued from Figure 4.1) Saturation Distribution during drying of Case 2 dual-porosity micromodel at (g) $t = 128.47$ min; (h) $t = 149.50$ min; (i) $t = 153.53$ min; (j) $t = 166.83$ min; (k) $t = 227.20$ min; (l) $t = 280.27$ min. Blue, white, and grey in the figure correspond to the water, air, and grain respectively.

water drying rate as a function of time. Again following a short startup period of about 20 minutes, the drying enters a constant rate period as evident in the drying rate curve. Despite the time-dependent fluctuations and pseudo-constant behavior, this period covers from $t =$ 20 min to $t = 170$ min, which is about 50% of the entire drying process. Compared to Case 1, the constant rate drying period in Case 2 is much longer and the drying rate is more stably maintained with no visible overall decline until about $t = 170$ min (Figure 4.8j). This is attributed to the strong capillary pumping effect of the micro-pores in the middle, which

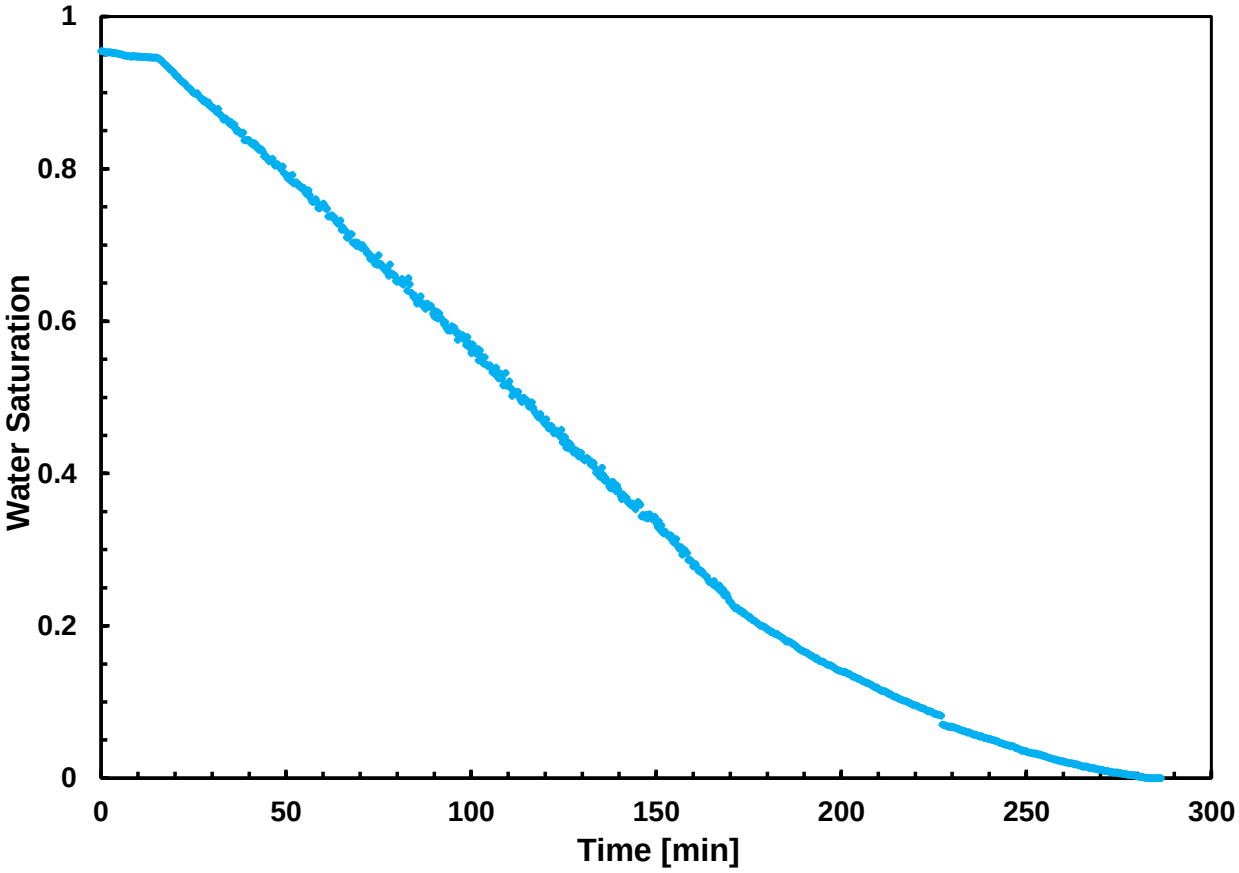


Figure 4.9: Water saturation variation over time in the drying process of Case 2 dual-porosity micromodel. Time is presented in minutes on the x-axis.

essentially serve as a wick that continuously supplies water from the bottom of the porous section to the top. Following the constant rate period, the upper portion of the micro-pore region starts to dry out, forming a gap between the drying front and the main channel, which in turn leads to a lower drying rate. In this second stage, the drying process is limited by vapor diffusion.

Figures 4.11 and 4.12 establish a correlation between the drying front location and the drying rate. Again a strong correlation between the drying front location and the drying rate is observed from Figure 4.11. The correlation coefficient was calculated to be 0.94, suggesting a strong dependence of the drying rate on the drying front location. Compared

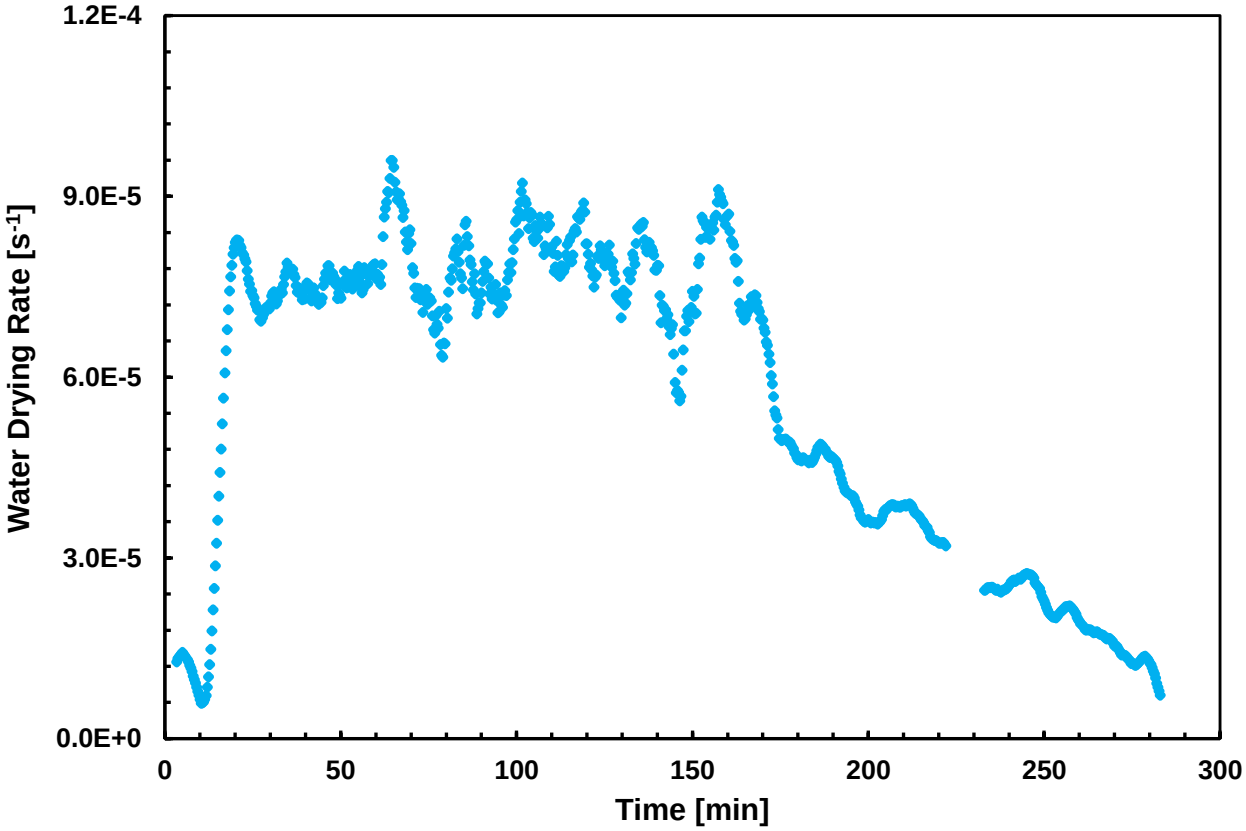


Figure 4.10: Water drying rate variation over time in the drying process of Case 2 dual-porosity micromodel. Water drying rate is presented in the unit of s^{-1} and Time is presented in minutes.

with Case 1, the drying process in Case 2 is even more diffusion limited, as the convective effect (*i.e.*, air flow within the porous section) is suppressed by the saturated micro-pore region in the middle, leading to a higher correlation coefficient.

Figures 4.13 and 4.14 show how different pore sizes impact water saturation distribution and other drying properties for a dual-porosity system, where micro- and macro-pore saturation and drying rate are plotted alongside the overall saturation and drying rate. Notably, drying in the micropores does not start until the macropores are nearly completely depleted. Despite the water-air interface being present in micropores adjacent to the channel, they do not recede due to loss of water because of the hydraulic connectivity continuously

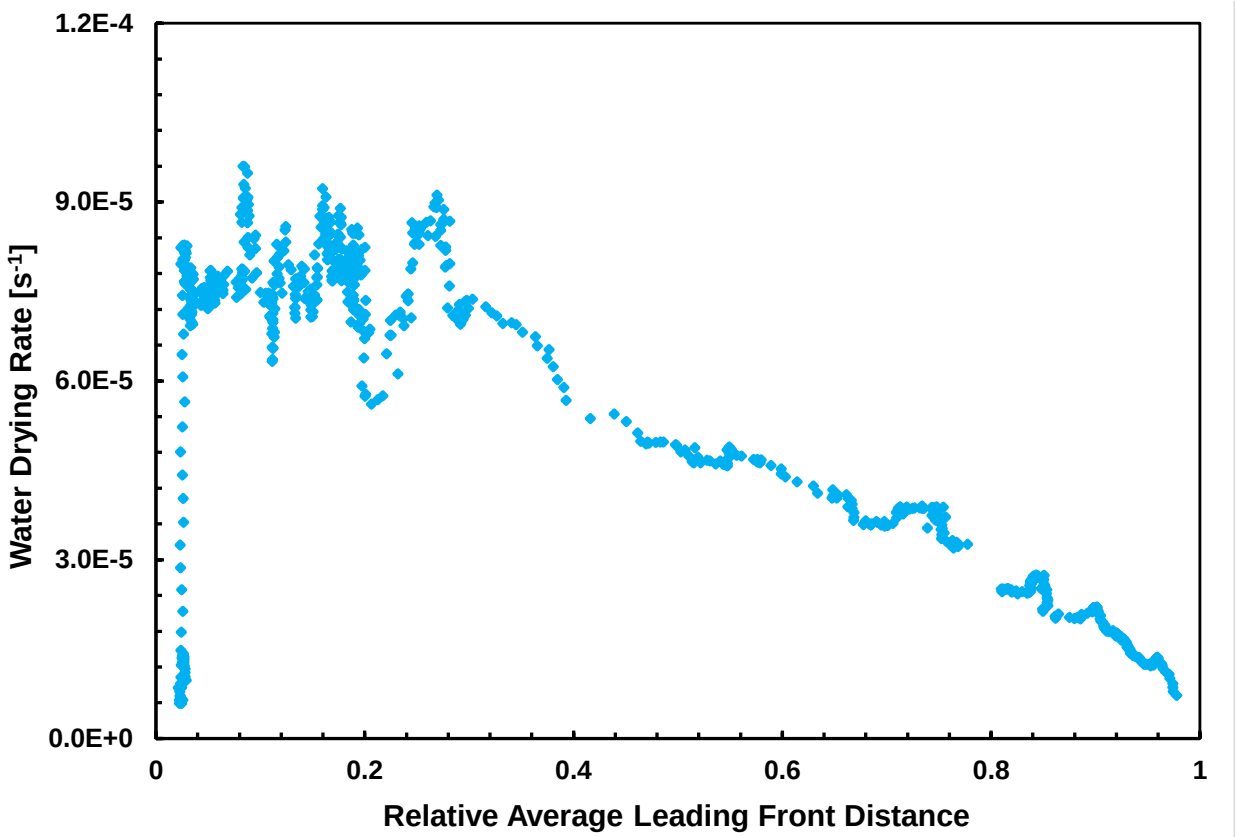


Figure 4.11: Water drying rate variation with relative average leading front distance in the drying process of Case 2 dual-porosity micromodel. Water drying rate is presented in the unit of s^{-1} and the relative average leading front distance is measured from the top edge of the micromodel porous region.

supplying water therein. This behavior is in agreement with the observations in Figure 4.8. As shown in Figures 4.8g and h, the micropore region remains saturated with water until the micropores are hydraulically disconnected from any macropores. Once the surrounding macropores are completely dried, the micropore region starts drying. The water films layer also starts descending in this region as the upper micropores dry, eventually dipping towards the bottom of the porous region, causing the complete drying of all macro- and micro-pores including the corner films. Additionally, these results show that the transition from Stage 1 (constant rate period) to Stage 2 (fall rate period) occurs when the drying just starts at the

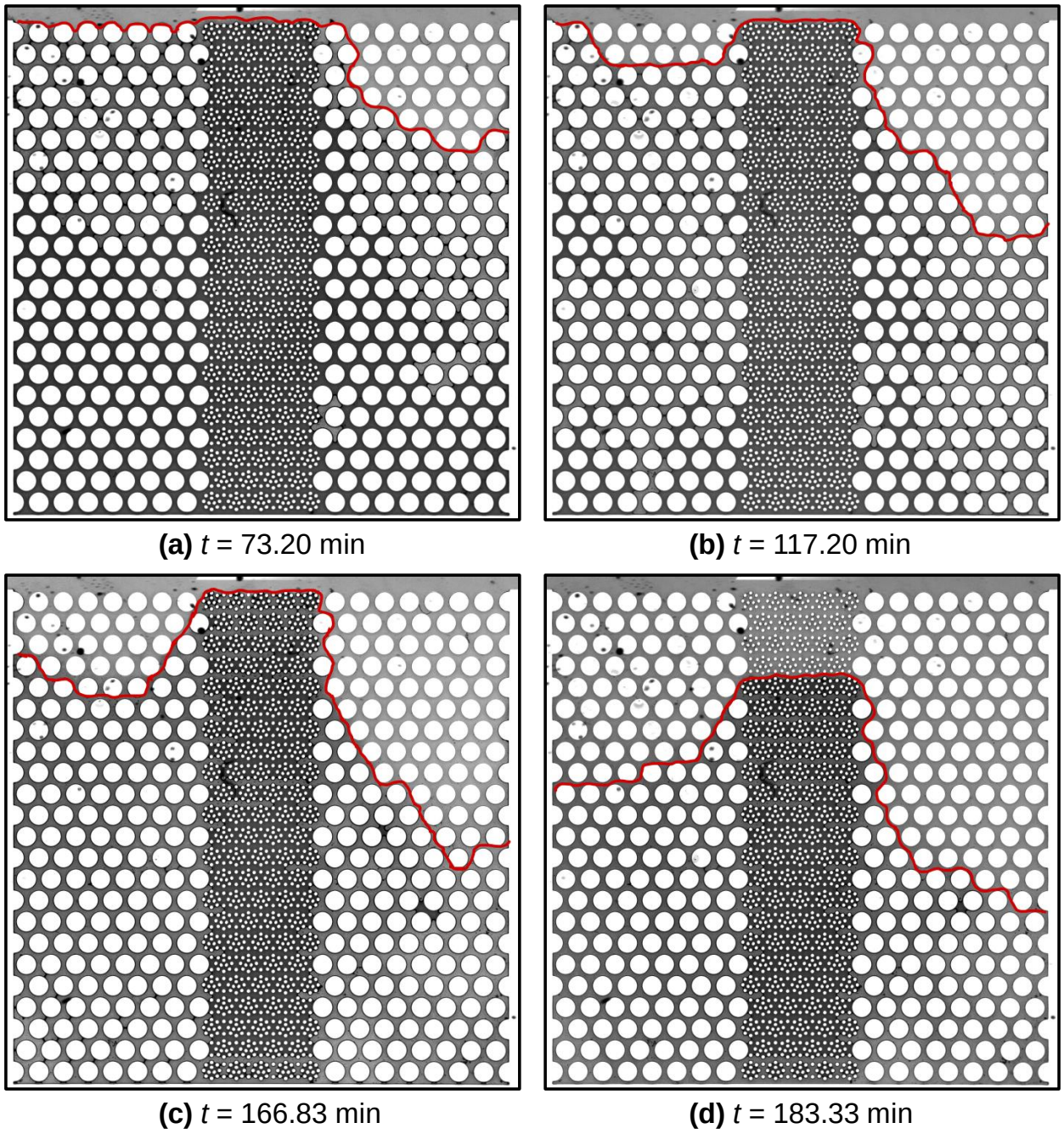


Figure 4.12: Drying front location for Case 2 micromodel during drying at (a) $t = 73.20$ min; (b) $t = 117.20$ min; (c) $t = 166.83$ min; (d) $t = 183.33$ min. The leading front boundaries are marked with red lines. Water and film layers are identified in the figure as deep black and grey respectively.

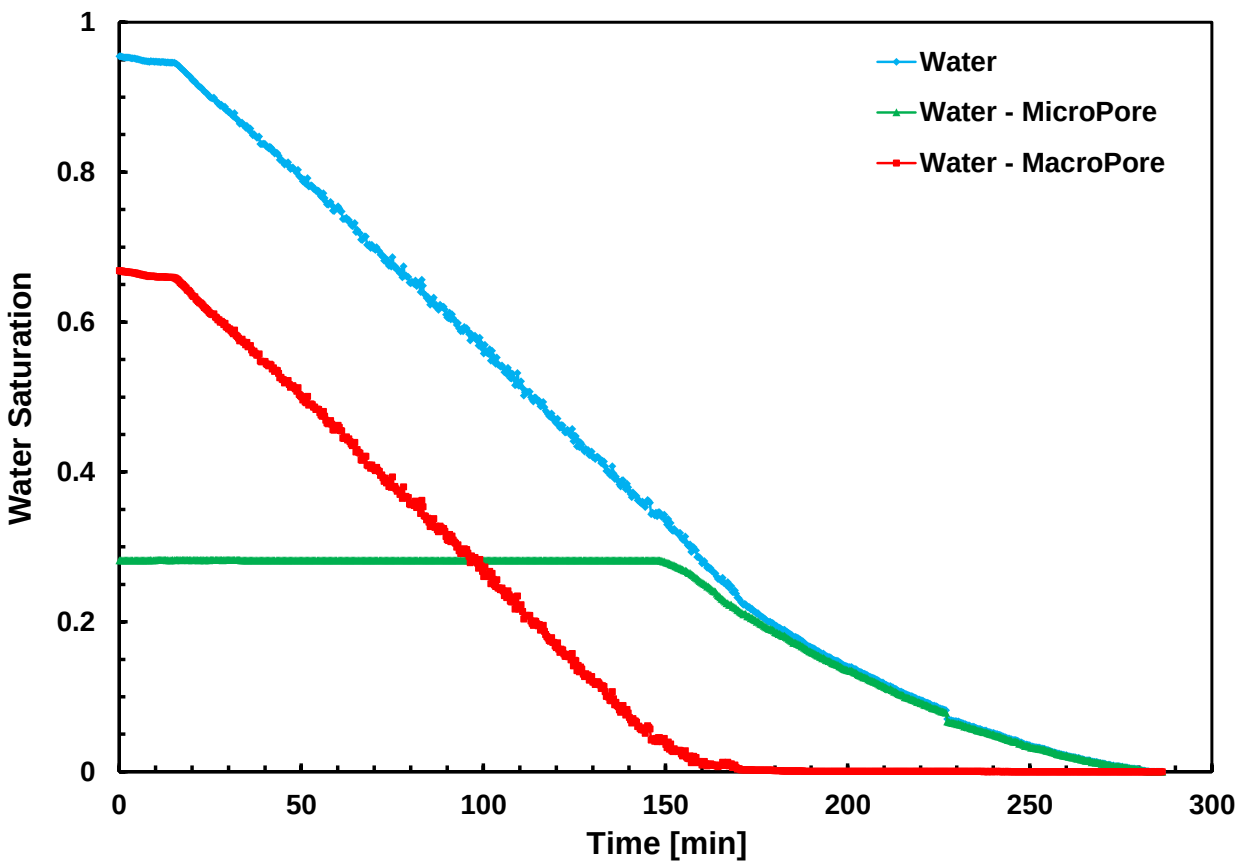


Figure 4.13: Water saturation variation for whole micromodel, micropores, and macropores with time during the drying process of Case 2 dual-porosity micromodel. Time is presented in minutes on the x-axis. Blue, green, and red lines in the plot correspond to water in whole porous region, micropores, and macropores respectively.

first row of micropores, and the film layer starts descending towards the bottom.

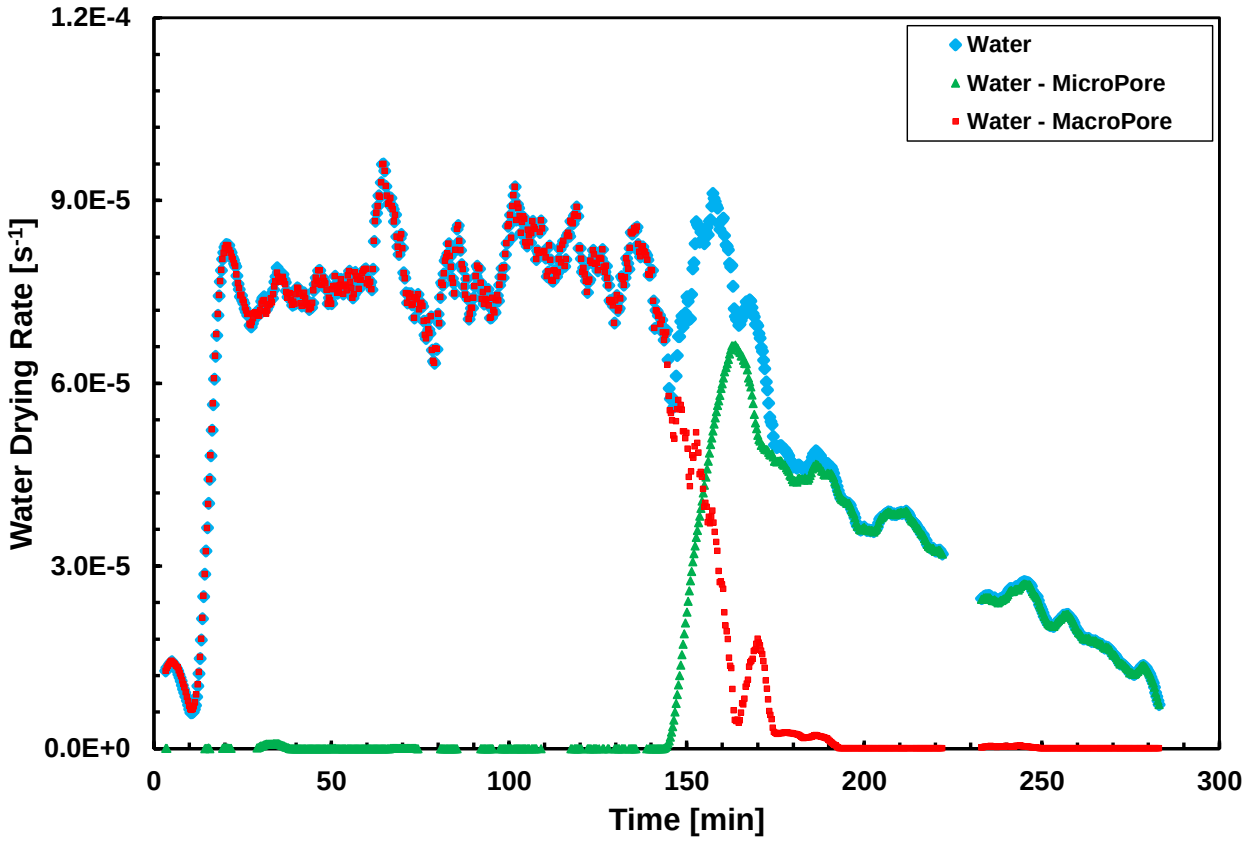


Figure 4.14: Water drying rate variation for the entire micromodel, micropores, and macropores with time during the drying process of Case 2 dual-porosity micromodel. Water drying rate is presented in the unit of s^{-1} and time is presented in minutes. Blue, green, and red lines in the plot correspond to water in the whole porous region, micropores, and macropores respectively.

To confirm our explanation of the capillary pumping effect, PIV measurement was performed at the very top of the porous media covering the entire micropore region and part of the macropore regions. Figure 4.15 shows the velocity field in the micropore region corresponding to t =73 min (Figure 4.7d). As evident in Figure 4.15, there is a flow going from the macropore region in the bottom right corner to the micropore region in the middle, which clearly demonstrates the capillary pumping effect and confirms our hypothesis. Additionally, a strong flow is created from the bottom of the FOV to the top, which supplies water to the drying front and explains why the drying front stays pinned at the top in spite

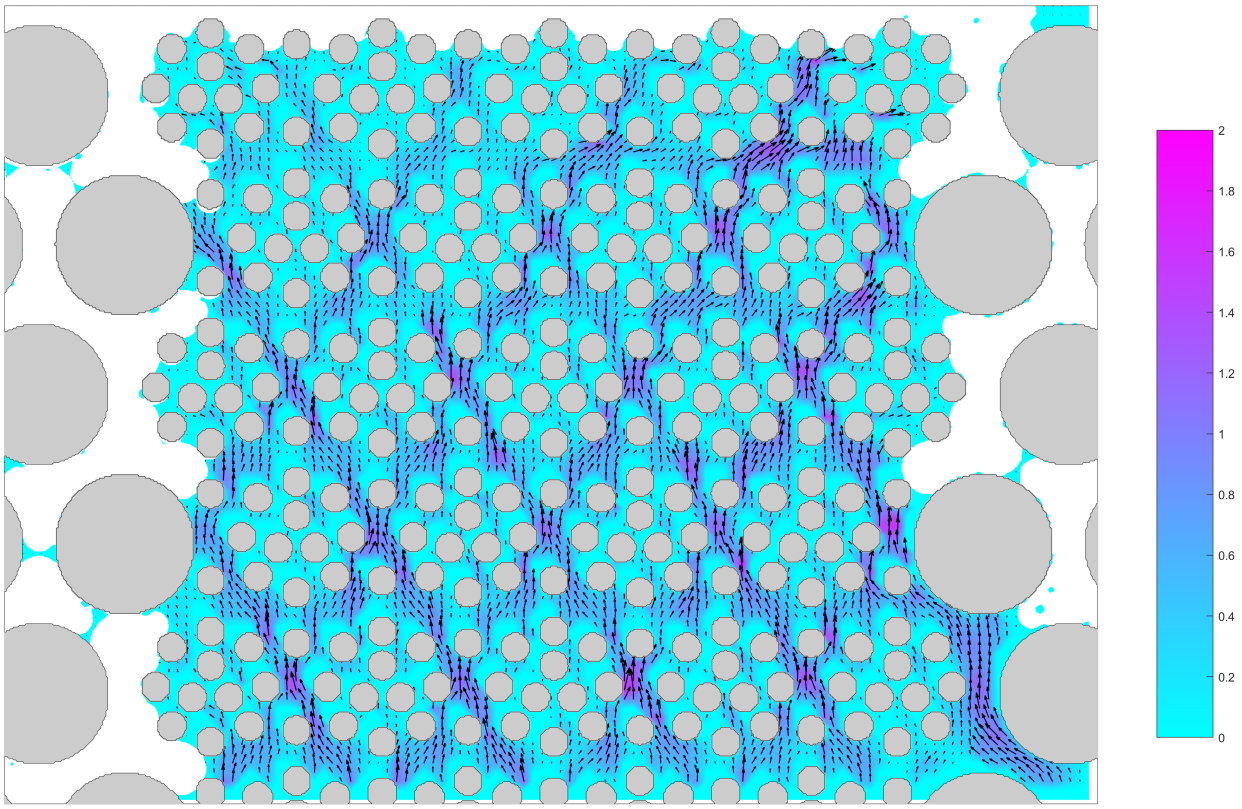


Figure 4.15: Velocity field obtained with PIV illustrating the capillary pumping effect from macropores to micropores, and the continuous water supply to the drying front. Here the FOV is 0.96 mm×0.7 mm, and the velocity scale is in μm/s.

of the strong drying at the air-water interface.

CHAPTER 5 FLOW-THROUGH DRYING IN HETEROGENEOUS POROUS STRUCTURE WITH DUAL POROSITY

This chapter elucidates the outcomes derived from the investigation into drying phenomena, with a particular focus on the characterization of drying incidents in Case 3 heterogeneous dual-porosity involving water and air as the working fluids. This result section emphasizes comprehensive understanding of the drying characteristics across the entire porous region, utilizing a lower magnification camera for image capture. This micromodel had a porous structure thickness of $25\,\mu$m($\pm 2\,\mu$m), which was less than the Case 1 and Case 2 micromodels.

In the conducted experiments, the porous region and channel were initially saturated entirely with the wetting phase, (*i.e.*, DI water). Following this saturation phase, nonwetting phase (*i.e.*, ambient air) was injected through the inlet to displace or drain the water from the porous region to get an equilibrium phase configuration. The flow of air was meticulously controlled using a syringe connected to the inlet with Teflon tubing. The syringe injected air at a constant flow rate set at 0.1 ml/min, facilitated by a syringe pump. Indeed, in the experimental setup, the airflow is directed from the right side of the porous region to the left.

The relative humidity of the air in the syringe was recorded at a range of 18% to 30%, and this condition for injected air was maintained throughout the experiment, as the syringe was not refilled for the second time during the drying process. The drainage process and the drying process were recorded at two different frame rates of 20 and 1 respectively. Between these two stages, no changes or interruption was made with the air flow rate of 0.1 ml/min. Greyscale images were captured with a lower magnification camera and were processed in MATLAB applying dynamic threshold technique.

The results in Figure 5.1 and 5.2 show the formation of saturation distribution for Case 3 heterogeneous dual-porosity micromodel during the drying process at different times and the impact of pore size and its distribution on the overall drying behavior after the drainage.

In the process of draining water from the fully saturated micromodel, air injection was utilized. Fundamentally, air seeks a path of least resistance determined by the size of the pore throat, directly linked to permeability. A wider pore throat indicates higher permeability, facilitating easier displacement of water by air. To initiate water displacement from any pores, air must accumulate pressure to a specific threshold at the throat, initiating drainage.

In scenarios with a higher air flow rate at a given location, pressure builds up more rapidly compared to lower flow rates. Under these higher flow rate conditions, multiple pore throats may experience accelerated pressure increases simultaneously, reaching the critical pressure for drainage. This leads to increased drainage and the emergence of distinct drainage patterns. Maintaining constant wettability of the micromodel and a constant air injection rate of 0.1 ml/min, our experiments demonstrated that air traveled from the inlet to the outlet, seeking paths with higher permeability for water drainage, resulting in a distinct drainage pattern. To achieve this distinct drainage pattern, it was also made sure that there was no bulk water remaining on the inlet side which might cause water supply to the pores.

In the initial drying phase, after the water drainage, the water saturation in the micromodel fell below 50%. At this point, air entering through the inlet displaced water from the outlet portion, creating a film flow at the edges. Larger pores depleted first, followed by the corner film, and ultimately, the smaller pores. For isolated pores, drying started simultaneously in both smaller and larger pores at any given location (Figure 5.1b, c, and d). Furthermore, as air moved towards the outlet through the pores, it experienced compression within the pores and expansion at the outlet portion. Due to this expansion, the initially saturated air from the inlet became unsaturated again, leading to the accumulation of water particles in the form of evaporation. This phenomenon resulted in faster drying

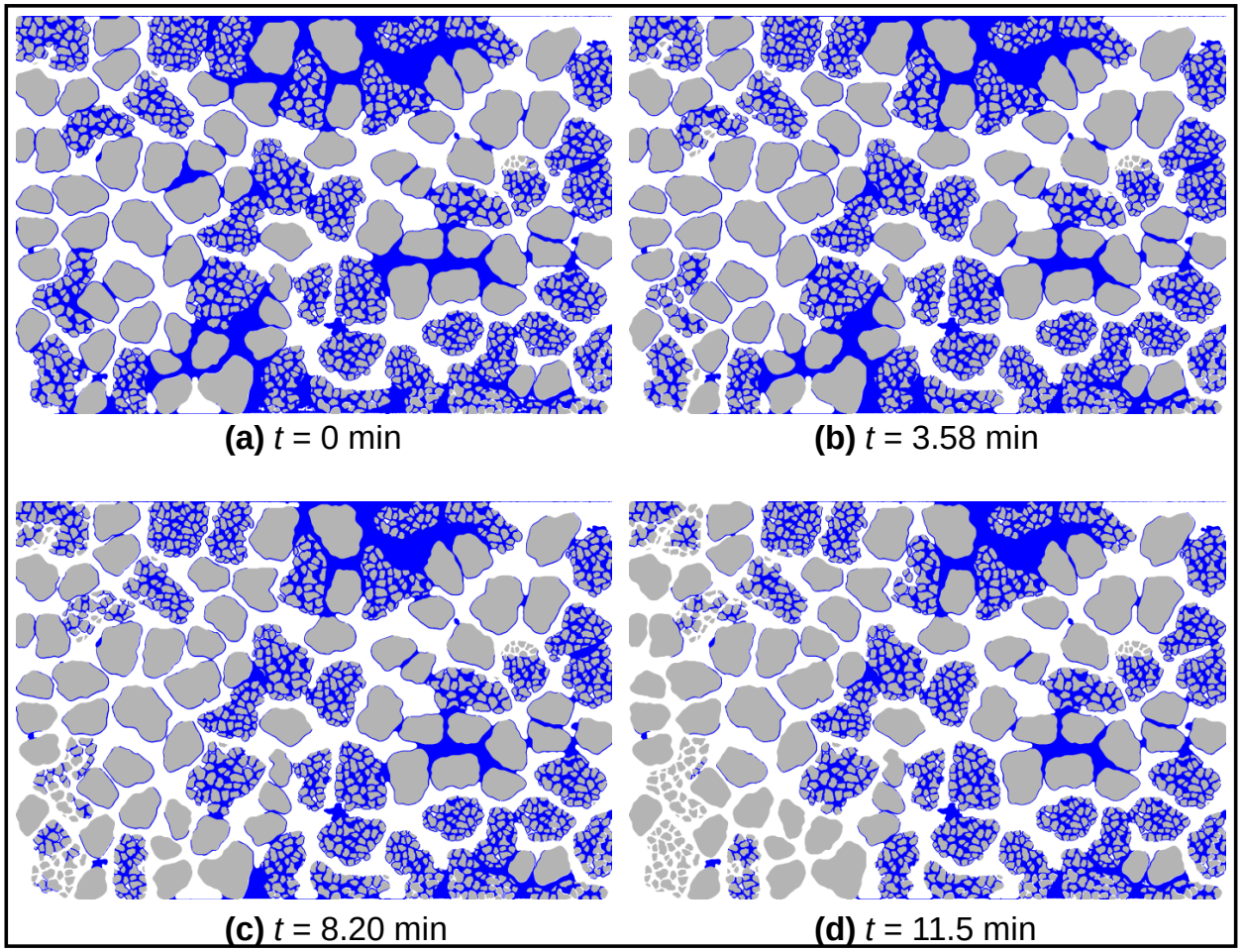


Figure 5.1: Saturation Distribution during drying of Case 3 heterogeneous dual-porosity micromodel at (a) $t = 0$ min; (b) $t = 3.58$ min; (c) $t = 8.20$ min; (d) $t = 11.50$ min. Blue, white, and grey in the figure correspond to the water, air, and grain respectively.

at the outlet portion. Conversely, slower drying occurred at the inlet due to the film flow originating from that portion, contributing to resistance in the drying process. Consequently, the inlet dried later compared to the outlet, despite a continuous supply of unsaturated air from the inlet which can be seen in Figure 5.1 and 5.2 at different times.

During the drying period, larger pores underwent water displacement through film flow due to the injection of air. Between t= 12.28 min and t= 18.41 min, smaller pores at numerous locations began experiencing drying. After a brief interval, these smaller pores

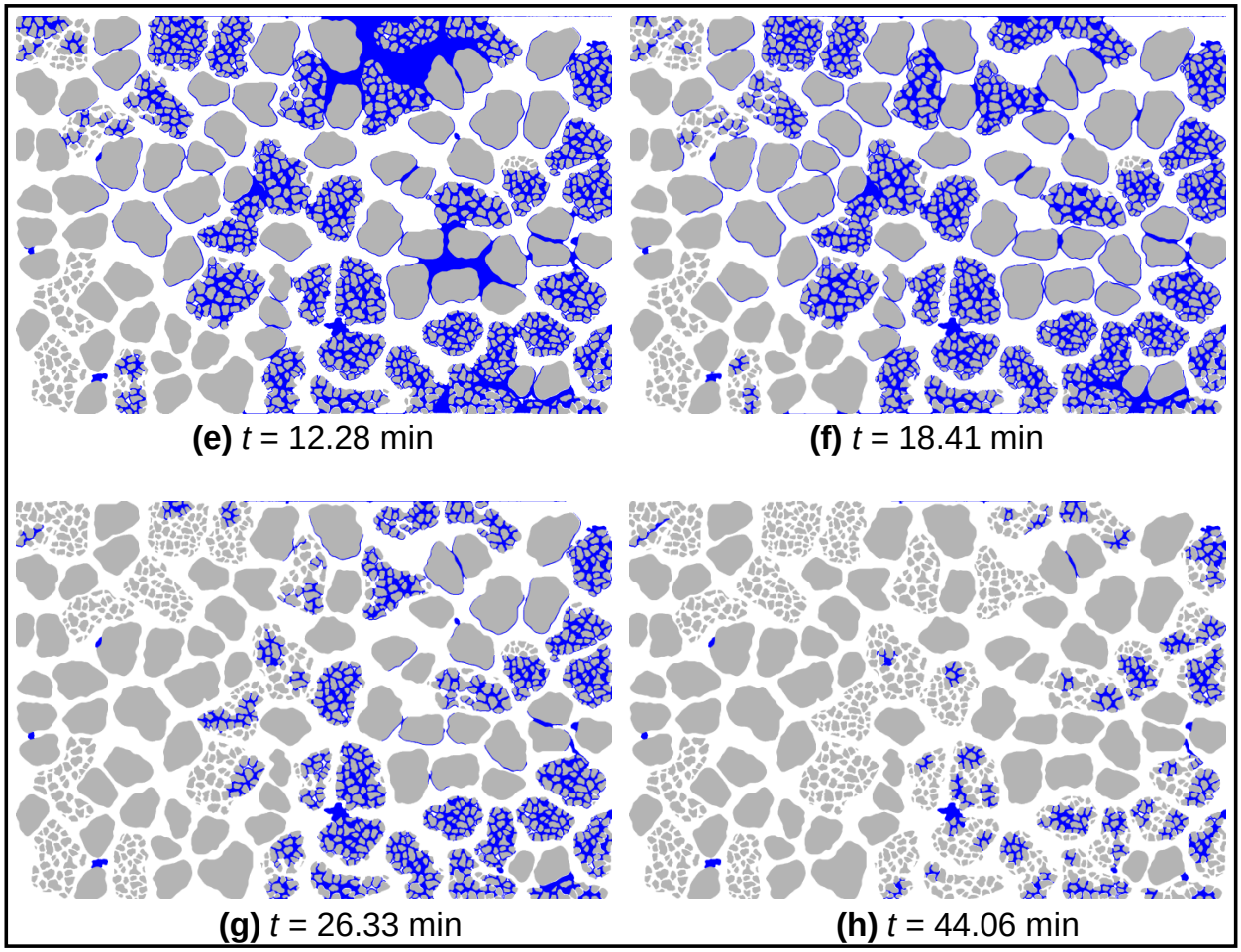


Figure 5.2: (Continued from Figure 5.1) Saturation Distribution during drying of Case 3 heterogeneous dual-porosity micromodel at (e) $t = 12.28$ min; (f) $t = 18.41$ min; (g) $t = 26.33$ min; (h) $t = 44.06$ min. Blue, white, and grey in the figure correspond to the water, air, and grain respectively.

were subsequently refilled with water displaced from the larger pores (Figure 5.2e, f and 5.8). Following the displacement or drying of water from all the macropores, all the micropores became isolated, initiating drying in each of them. At this stage, the corner films of all larger pores dried first, leading to the complete drying of all micropores. After 48 minutes of continuous air flow at a constant rate, the micromodel dried completely.

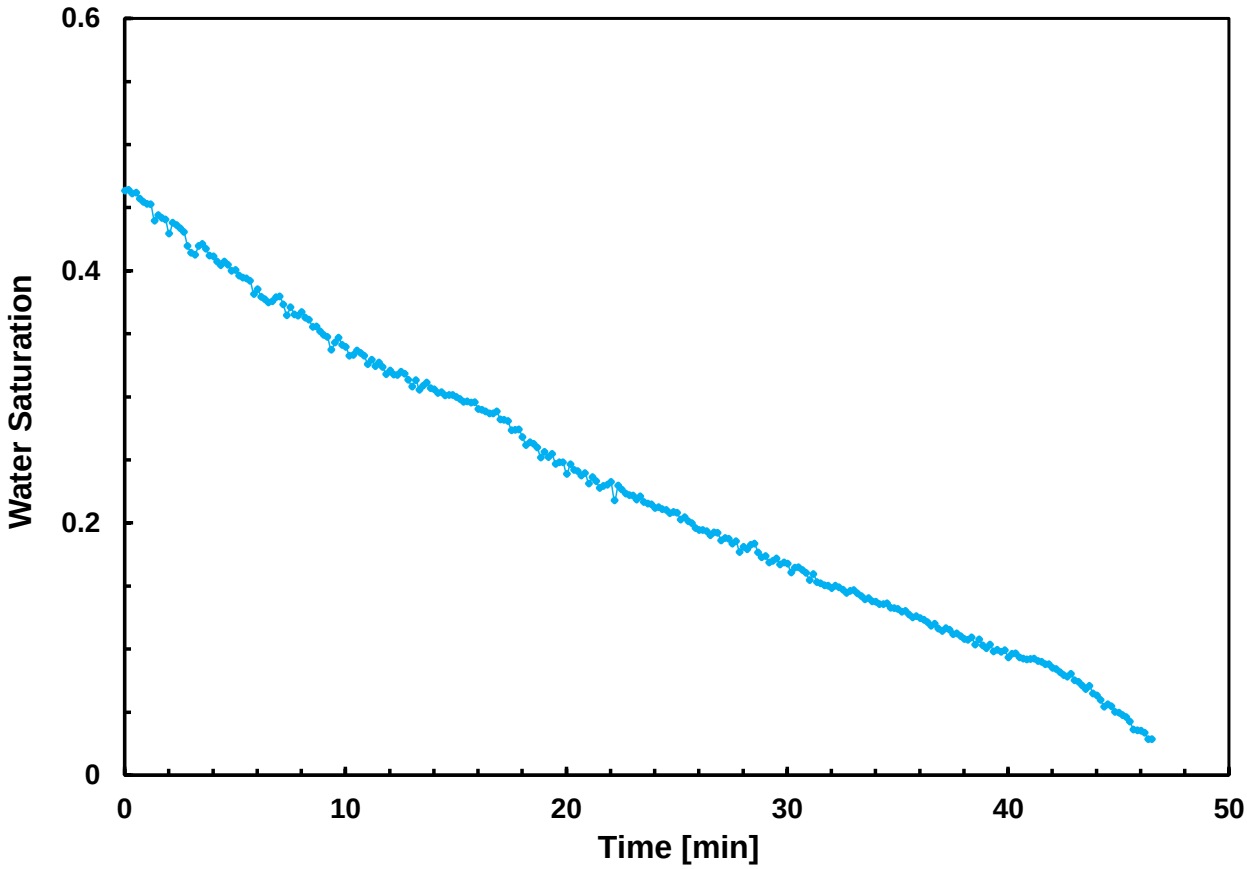


Figure 5.3: Water saturation variation over time in the drying process of Case 3 heterogeneous dual-porosity micromodel. Time is presented in minutes on the x-axis.

Figure 5.3 presents the variation in water saturation over time for the drying Case 3 heterogeneous dual-porosity micromodel under flow-through air flow conditions. The slope of this graph, presented in Figure 5.4, represents the water displacement rate in units of s^{-1} as a function of time. While Figure 5.3 provides insights into the overall saturation decrease over time, Figure 5.4 indicates the factors influencing the entire process in the porous region. Additionally, Figures 5.5 establish a correlation between the interfacial length and drying rate, offering a deeper understanding of the significant changes in drying rate during the process. Furthermore, Figure 5.6 and 5.7 show how different pore sizes impact water saturation distribution and other drying properties for a heterogeneous dual-porosity

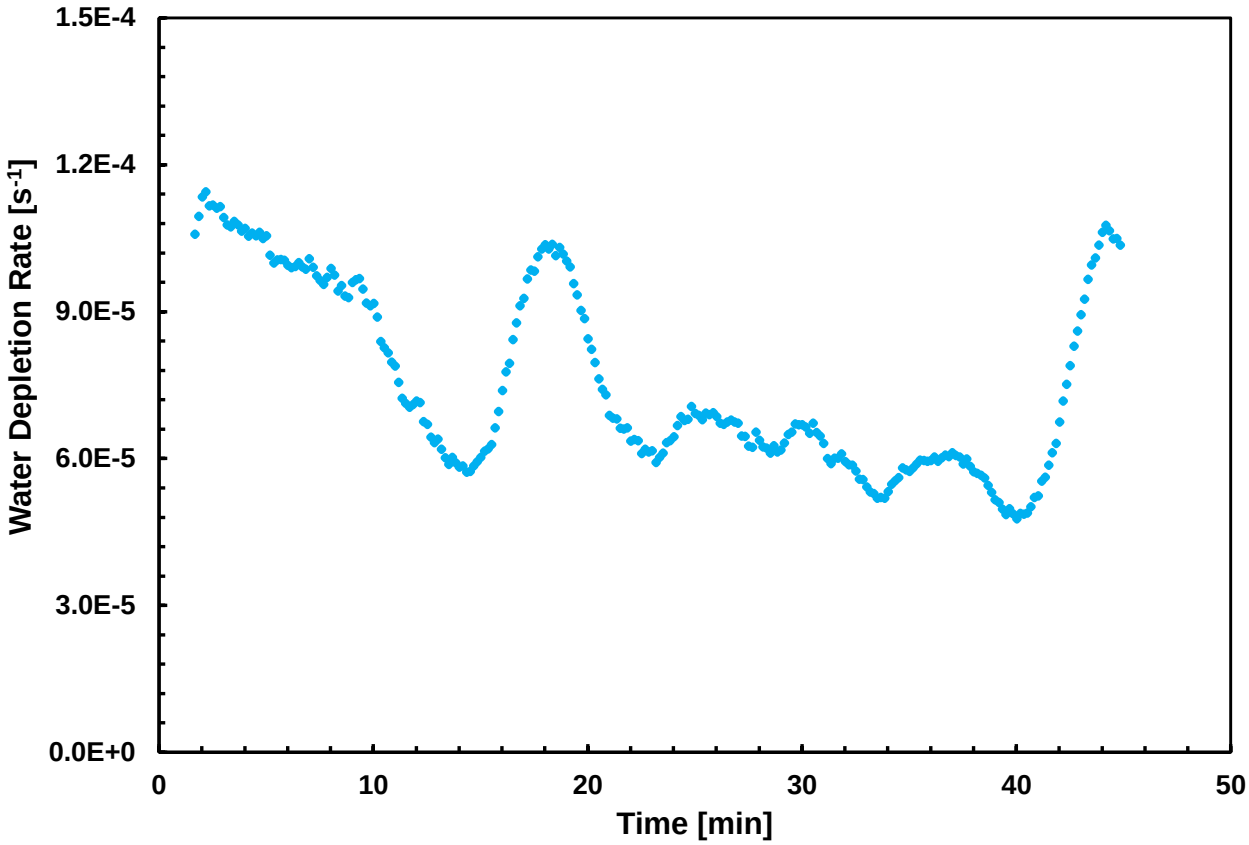


Figure 5.4: Water displacement rate variation over time in the drying process of Case 3 heterogeneous dual-porosity micromodel. Water displacement rate is presented in the unit of s^{-1} and Time is presented in minutes.

system.

In Figure 5.4, the water displacement rate initially decreased, with a notable spike between $t = 14$ min and $t = 22$ min. This incident spike is clarified in Figure 5.8, which illustrates the sudden displacement of bulk water from the macropores through film flow at the edge to the outlet and refill of micropores. Another increase in the water displacement rate is observed at $t = 40$ min, as shown in Figure 5.5. Here, the increase in interfacial length is identified as the cause for the heightened drying rate. Additionally, unlike Case 1 and Case 2, where the water drying rate is strongly correlated with the drying front location, Figure 5.5 shows a strong correlation between the water drying rate and the interfacial length in

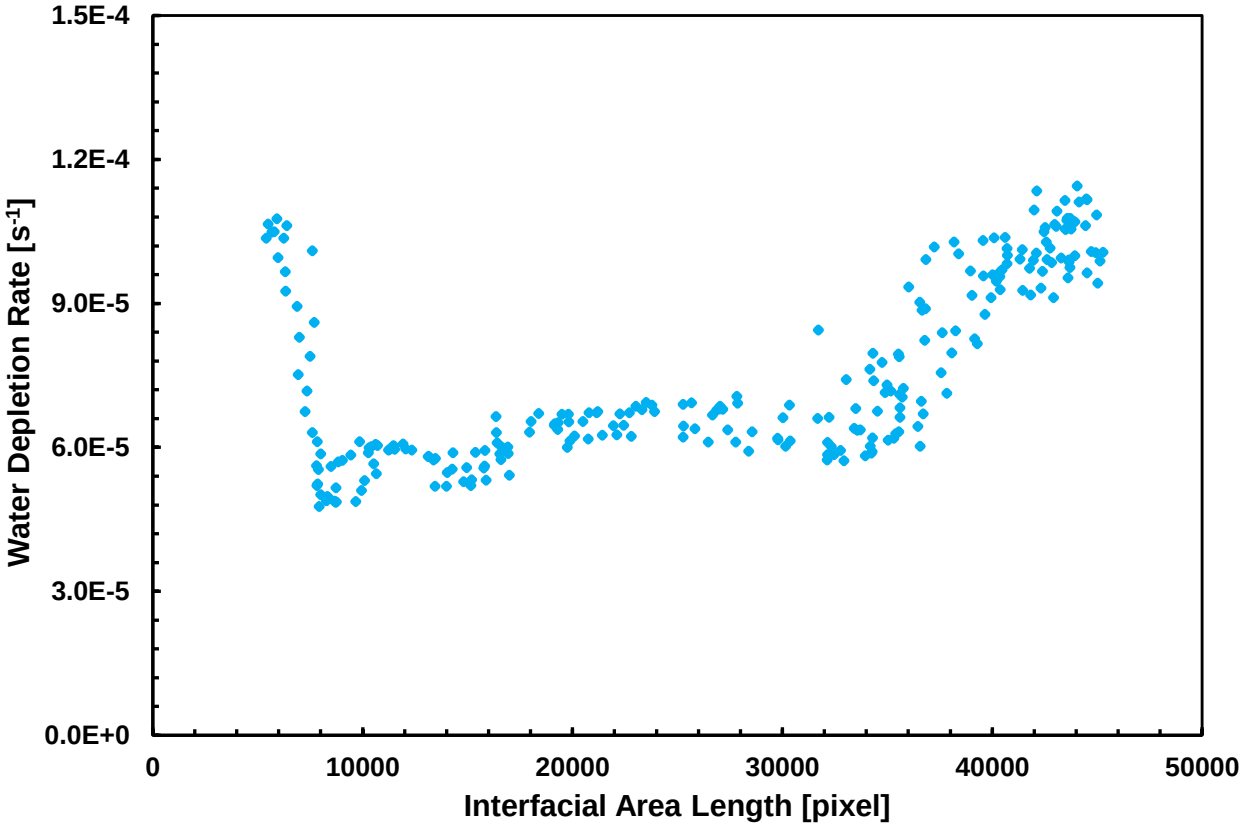


Figure 5.5: Water depletion rate variation with interfacial length during the drying in Case 3 micromodel. Water displacement rate is presented in the unit of s^{-1} and interfacial length is presented in pixels.

Case 3. The correlation coefficient between the two quantities was calculated to be 0.82. This strong correlation suggests that the flow-through drying process is largely limited by the phase-change step rather than the transport in the water or the vapor phase, as expected.

The impact of different pore sizes and distributions is evident in Figure 5.6 and 5.7, where micro- and macro-pore saturation and water displacement rate are plotted alongside the overall saturation and displacement rate. These graphs illustrate how micro- and macro-pore behavior influences the overall drying rate.

In Figure 5.6 and 5.7, the initial stages of drying are depicted in both micro- and macro-pores. Specifically, the micropores that initially dried were those isolated from

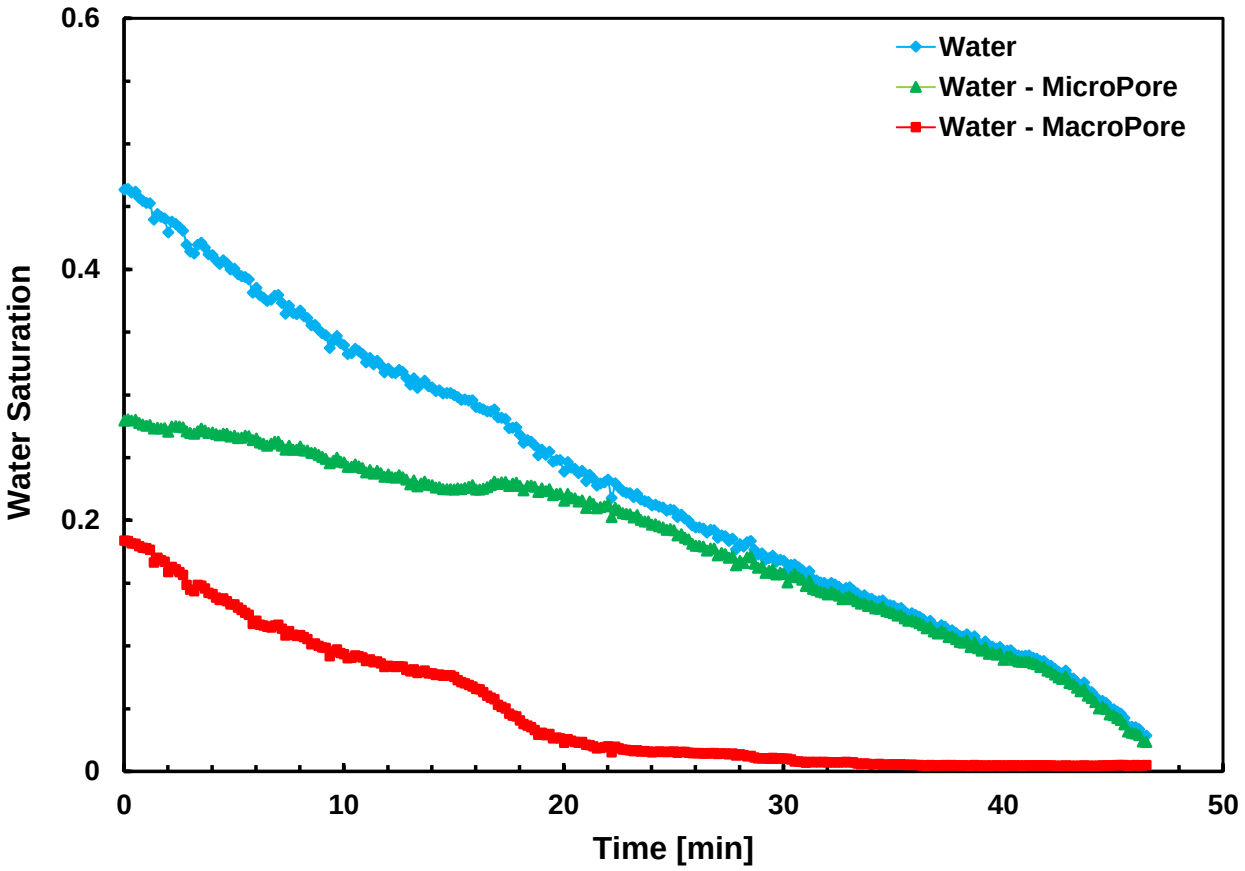


Figure 5.6: Water saturation variation for whole micromodel, micropores, and macropores with time during the drying process of Case 3 heterogeneous dual-porosity micromodel. Time is presented in minutes on the x-axis. Blue, green, and red lines in the plot correspond to water in whole porous region, micropores, and macropores respectively.

the bulk water and exposed to the air-water interface, as illustrated in Figure 5.1. For the isolated micropores, capillary pumping remained inactive, while for the hydraulically connected micropores, capillary pumping was evident, acting as a resistance mechanism against micropore drying. Notably, the negative water displacement rate for micropores in Figure 5.7 indicates the water refilling of the pores. This refilling occurred due to the drainage of bulk water from macropores, leading to the replenishment of surrounding micropores that were previously partially dried, as shown in Figure 5.8. Upon the completion of water displacement from the macropores, the micropores started drying at an accelerated rate,

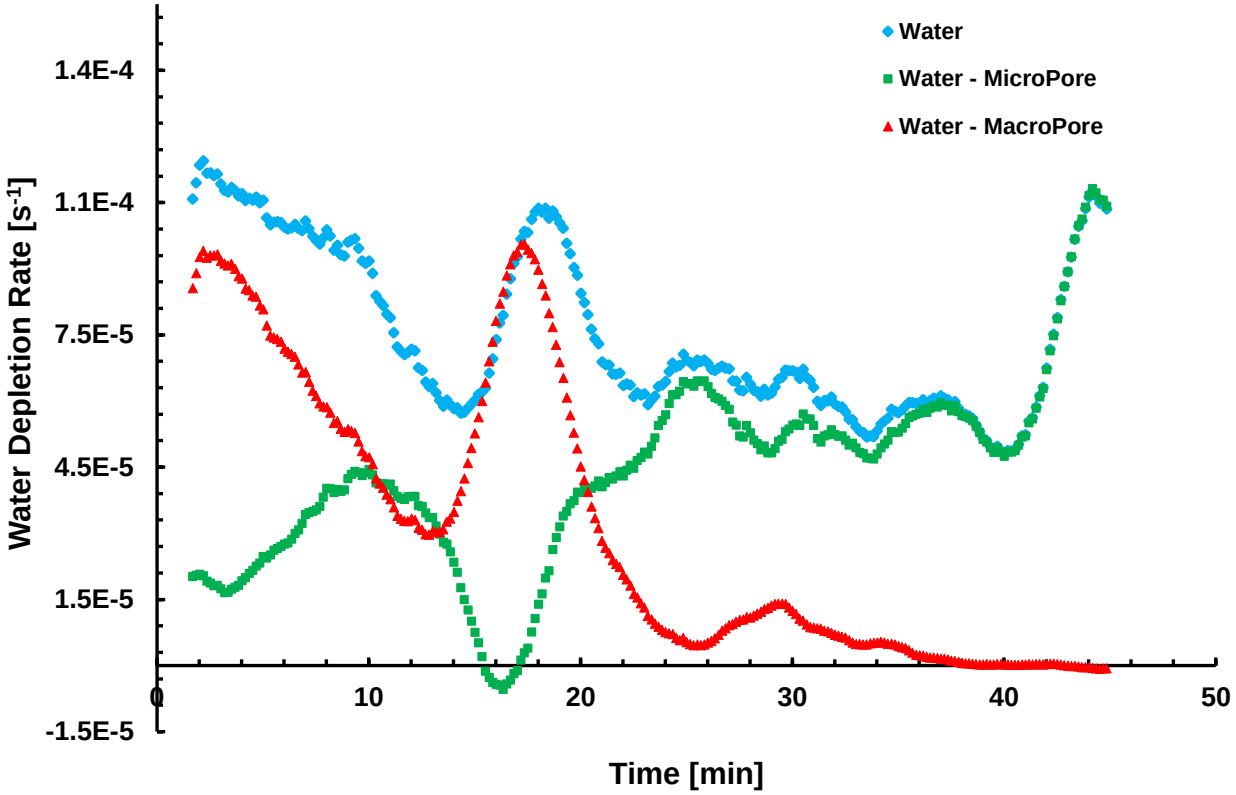


Figure 5.7: Water displacement rate variation for whole micromodel, micropores, and macropores with time during the drying process of Case 3 heterogeneous dual-porosity micromodel. Water displacement rate is presented in the unit of s^{-1} and time is presented in minutes. Blue, green, and red lines in the plot correspond to water in the whole porous region, micropores, and macropores respectively. Negative displacement rate means refill in this graph.

attributed to the increased interfacial length, as demonstrated in Figure 5.5.

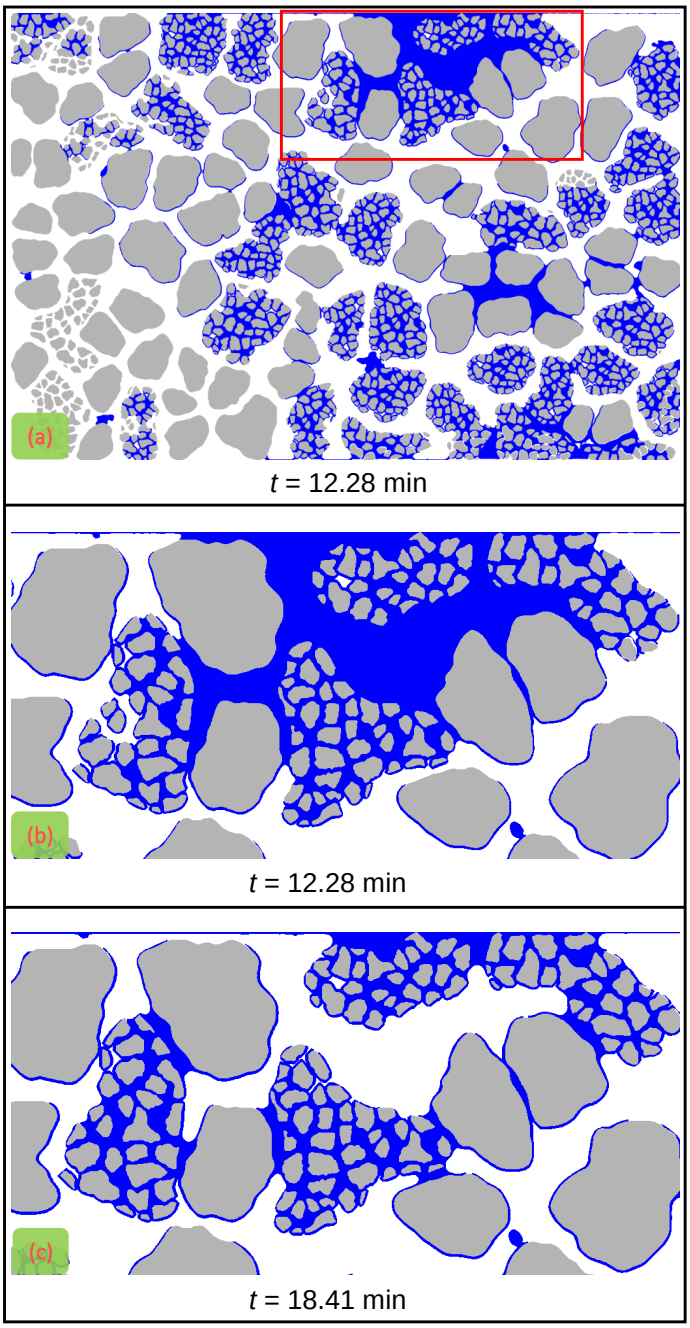


Figure 5.8: Water refilling incident of micropores between the time t = 12.28 min and t = 18.41 min. Blue, white, and grey in the figure correspond to the water, air, and grain respectively. (a) Water saturation distribution of Case 3 micromodel at t = 12.28 min with a red marked box; (b) and (c) Water saturation distribution for the red marked box of Figure 5.8a at t = 12.28 min and t = 18.41 min respectively.

CONCLUSIONS AND FUTURE WORK

In this thesis, a series of experiments were conducted to explore pore-scale physics, focusing on diffusion-driven and flow-through drying. Three distinct types of micromodels were employed to examine different aspects of these phenomena. The obtained results facilitated a comprehensive comparison and understanding of parameters and fundamental principles of multiphase flow. In the following chapter, conclusions drawn from these experiments are presented, along with potential scopes for future research.

Conclusions

1. A novel fabrication technique for creating 2D dual-porosity micromodels with precise porous structures and excellent optical access has been developed. The micromodels fabricated using this technique have been subjected to quality evaluation, demonstrating satisfactory results.

2. To investigate flow dynamics simultaneously at both micro- and macro-scales, an innovative employing the novel micromodels, dual-magnification imaging system, coupled with microscopic particle image velocimetry (micro-PIV) and epi-fluorescent microscopy, has been developed.

3. To investigate the flow dynamics inherent in the drying process of dual-porosity porous structures, three distinct micromodels were created and employed in experiments conducted with a dual-magnification imaging system. The first micromodel (homogeneous micromodel) functioned as a baseline case, the second (dual-porosity micromodel) was utilized for convective drying experiments, and the third (heterogeneous dual-porosity micromodel) was dedicated to flow-through drying experiments.

4. Results obtained from the experiments have unveiled distinct drying stages along with their corresponding driving factors. An examination of the impact of the film layer during the drying process has been carried out. Furthermore, the study delved into the influence of pore structure, sizes, and distribution on the drying process. The effects of hydraulic connectivity, capillary pumping during drying, and film flow were also scrutinized, offering valuable insights for subsequent investigations into the drying dynamics within porous media.

Future Work Outline

The current study has provided significant insights, yet further research is essential to broaden our understanding of capillary pumping, micro-macro flow interactions involving particles, and various drying processes. Modifying the micropore pattern in the Case 2 dual-porosity micromodel by segregating the micropores throughout the entire porous media and adjusting the Case 3 heterogeneous micromodel for studying the diffusion-driven drying process can help significantly to investigate the micro-macro flow interactions due to capillary pumping. Utilizing techniques such as Micro-PIV and Particle Tracking Velocimetry (PTV) extensively can help investigate capillary pumping and geometry effects. Additionally, developing an image processing technique to track the film flow layer would provide valuable insights diffusion-driven drying process. Additionally, fluids with different wettability can be utilized to broaden the knowledge of drying process. Furthermore, exploring drying in 3D porous media remains a promising scope for future investigations.

REFERENCES CITED

[1] P A. Gauglitz, F Friedmann, S I. Kam, and W R. Rossen. Foam generation in homogeneous porous media. *Chemical Engineering Science*, 57(19):4037–4052, 2002.

[2] Ronald J Adrian and Jerry Westerweel. *Particle image velocimetry*. Number 30. Cambridge university press, 2011.

[3] JOSEPH ALLERTON. *THE THOROUGH-DRYING OF POROUS MEDIA*. PhD thesis, University of Michigan, 1948.

[4] Yara Alzahid, Peyman Mostaghimi, Majid Ebrahimi Warkiani, Ryan T Armstrong, Vahid Joekar-Niasar, and Nikolaos Karadimitriou. Alkaline surfactant polymer flooding: what happens at the pore scale? In *SPE Europec featured at EAGE Conference and Exhibition?*, page D022S014R003. SPE, 2017.

[5] Heiko Andrä, Nicolas Combaret, Jack Dvorkin, Erik Glatt, Junehee Han, Matthias Kabel, Youngseuk Keehm, Fabian Krzikalla, Minhui Lee, Claudio Madonna, et al. Digital rock physics benchmarks—part i: Imaging and segmentation. *Computers & Geosciences*, 50:25–32, 2013.

[6] Ryan T Armstrong and Steffen Berg. Interfacial velocities and capillary pressure gradients during haines jumps. *Physical Review E*, 88(4):043010, 2013.

[7] A. Bazylak. Liquid water visualization in pem fuel cells: A review. *International Journal of Hydrogen Energy*, 34(9):3845–3857, 2009.

[8] Jacob Bear. *Dynamics of fluids in porous media*. Courier Corporation, 2013.

[9] RB Bird, WE Stewart, and EN Lightfoot. Transport phenomena, wiley, new york, 1960.

[10] Marco Bittelli, Francesca Ventura, Gaylon S Campbell, Richard L Snyder, Fabia Gallegati, and Paola Rossi Pisa. Coupling of heat, water vapor, and liquid water fluxes to compute evaporation in bare soils. *Journal of Hydrology*, 362(3-4):191–205, 2008.

[11] Martin J Blunt. *Multiphase flow in permeable media: A pore-scale perspective*. Cambridge university press, 2017.

[12] Van Brakel. Mass transfer in convective drying. *(No Title)*, 1:217, 1980.

[13] R. P. Cahn and N. N. Li. Separation of phenol from waste water by the liquid membrane technique. *Separation Science*, 9(6):505–519, 1974.

[14] Andrea Carminati, Anders Kaestner, Olaf Ippisch, Azad Koliji, Peter Lehmann, René Hassanein, Peter Vontobel, E Lehmann, Lyesse Laloui, Laurent Vulliet, et al. Water flow between soil aggregates. *Transport in Porous Media*, 68:219–236, 2007.

[15] EM Chapman, Jianhui Yang, JP Crawshaw, and ES Boek. Pore scale models for imbibition of co2 analogue fluids in etched micro-model—— junctions using microfluidic experiments and direct flow calculations. *Energy Procedia*, 37:3680–3686, 2013.

[16] Alfred Chatenever and John C Calhoun Jr. Visual examinations of fluid behavior in porous media-part i. *Journal of Petroleum Technology*, 4(06):149–156, 1952.

[17] Fabien Chauvet, Paul Duru, Sandrine Geoffroy, and Marc Prat. Three periods of drying of a single square capillary tube. *Physical review letters*, 103(12):124502, 2009.

[18] Fabien Chauvet, Paul Duru, and Marc Prat. Depinning of evaporating liquid films in square capillary tubes: Influence of corners' roundedness. *Physics of Fluids*, 22(11), 2010.

[19] Chen Chen, Pierre Joseph, Sandrine Geoffroy, Marc Prat, and Paul Duru. Evaporation with the formation of chains of liquid bridges. *Journal of Fluid Mechanics*, 837:703–728, 2018.

[20] Xiao Dong Chen and Arun S Mujumdar. *Drying technologies in food processing*. John Wiley & Sons, 2009.

[21] KT Christensen. The influence of peak-locking errors on turbulence statistics computed from piv ensembles. *Experiments in fluids*, 36:484–497, 2004.

[22] N.C Christov, D.N Ganchev, N.D Vassileva, N.D Denkov, K.D Danov, and P.A Kralchevsky. Capillary mechanisms in membrane emulsification: oil-in-water emulsions stabilized by tween 20 and milk proteins. *Colloids and Surfaces A: Physicochemical and Engineering Aspects*, 209(1):83–104, 2002.

[23] Constantinos V Chrysikopoulos, Christina C Plega, and Vasileios E Katzourakis. Non-invasive in situ concentration determination of fluorescent or color tracers and pollutants in a glass pore network model. *Journal of hazardous materials*, 198:299–306, 2011.

[24] V Ciric, M Manojlovic, Lj Nesic, and M Belic. Soil dry aggregate size distribution: effects of soil type and land use. *Journal of soil science and plant nutrition*, 12(4):689–703, 2012.

[25] R. Colombelli, Kartik Srinivasan, Mariano Troccoli, O. Painter, C. Gmachl, Don Tennant, A.M. Sergent, Deborah Sivco, AY Cho, and Federico Capasso. Fabrication technologies for quantum cascade photonic-crystal microlasers. *Nanotechnology*, 12 2004.

[26] Henry Darcy. *Les fontaines publiques de la ville de Dijon: exposition et application des principes à suivre et des formules à employer dans les questions de distribution d'eau*, volume 1. Victor dalmont, 1856.

[27] Sujit S Datta, Harry Chiang, TS Ramakrishnan, and David A Weitz. Spatial fluctuations of fluid velocities in flow through a three-dimensional porous medium. *Physical review letters*, 111(6):064501, 2013.

[28] Rajakumar S Devarapalli, Amina Islam, Titly Farhana Faisal, Mohamed Sassi, and Mustapha Jouiad. Micro-ct and fib–sem imaging and pore structure characterization of dolomite rock at multiple scales. *Arabian Journal of Geosciences*, 10:1–12, 2017.

[29] Teresa Diaz Gonçalves, Leo Pel, and José Rodrigues. Influence of paints on drying and salt distribution processes in porous building materials. *Construction and Building Materials*, pages 1751–1759, 05 2009.

[30] Francis AL Dullien. *Porous media: fluid transport and pore structure*. Academic press, 2012.

[31] Irving Fatt and Waldemar A Klikoff Jr. Effect of fractional wettability on multiphase flow through porous media. *Journal of Petroleum Technology*, 11(10):71–76, 1959.

[32] Linlin Fei, Feifei Qin, Jianlin Zhao, Dominique Derome, and Jan Carmeliet. Pore-scale study on convective drying of porous media. *Langmuir*, 38(19):6023–6035, 2022.

[33] W.J.N. Fernando, A.L. Ahmad, S.R. Abd. Shukor, and Y.H. Lok. A model for constant temperature drying rates of case hardened slices of papaya and garlic. *Journal of Food Engineering*, 88(2):229–238, 2008.

[34] Gina S Fiorini, Gavin DM Jeffries, David SW Lim, Christopher L Kuyper, and Daniel T Chiu. Fabrication of thermoset polyester microfluidic devices and embossing masters using rapid prototyped polydimethylsiloxane molds. *Lab on a Chip*, 3(3):158–163, 2003.

[35] Alireza Gerami, Yara Alzahid, Peyman Mostaghimi, Navid Kashaninejad, Farzan Kazemifar, Tammy Amirian, Nader Mosavat, Majid Ebrahimi Warkiani, and Ryan T Armstrong. Microfluidics for porous systems: fabrication, microscopy and applications. *Transport in Porous Media*, 130:277–304, 2019.

[36] Alireza Gerami, Ryan T Armstrong, Benjamin Johnston, Majid Ebrahimi Warkiani, Nader Mosavat, and Peyman Mostaghimi. Coal-on-a-chip: visualizing flow in coal fractures. *Energy & fuels*, 31(10):10393–10403, 2017.

[37] Adem Gharsallaoui, Gaëlle Roudaut, Odile Chambin, Andrée Voilley, and Rémi Saurel. Applications of spray-drying in microencapsulation of food ingredients: An overview. *Food research international*, 40(9):1107–1121, 2007.

[38] Teamrat A Ghezzehei and Dani Or. Dynamics of soil aggregate coalescence governed by capillary and rheological processes. *Water Resources Research*, 36(2):367–379, 2000.

[39] D. Gilfillan and G. Marland. Cdiac-ff: global and national co_2 emissions from fossil fuel combustion and cement manufacture: 1751–2017. *Earth System Science Data*, 13(4):1667–1680, 2021.

[40] Peter Gravesen, Jens Branebjerg, and O Søndergård Jensen. Microfluidics-a review. *Journal of micromechanics and microengineering*, 3(4):168, 1993.

[41] Siyi Gu, Yongheng Wang, Daofang Zhang, Mengmeng Xiong, He Gu, and Zhihua Xu. Utilization of porous carbon synthesized with textile wastes via calcium acetate template for tetracycline removal: The role of template agent and the formation mechanism. *Chemosphere*, 289:133148, 2022.

[42] Laura Guglielmini, Alexandre Gontcharov, Antonio J Aldykiewicz, and Howard A Stone. Drying of salt solutions in porous materials: Intermediate-time dynamics and efflorescence. *Physics of Fluids*, 20(7), 2008.

[43] Naga Siva Kumar Gunda, Bijoyendra Bera, Nikolaos K Karadimitriou, Sushanta K Mitra, and S Majid Hassanizadeh. Reservoir-on-a-chip (roc): A new paradigm in reservoir engineering. *Lab on a Chip*, 11(22):3785–3792, 2011.

[44] Stefan Haeberle and Roland Zengerle. Microfluidic platforms for lab-on-a-chip applications. *Lab on a Chip*, 7(9):1094–1110, 2007.

[45] Vanessa Hebert, Charlotte Garing, Linda Luquot, PA Pezard, and Philippe Gouze. Multi-scale x-ray tomography analysis of carbonate porosity. *Geological Society, London, Special Publications*, 406(1):61–79, 2015.

[46] H Hematpour, M Mardi, S Edalatkhah, and R Arabjamaloei. Experimental study of polymer flooding in low-viscosity oil using one-quarter five-spot glass micromodel. *Petroleum Science and Technology*, 29(11):1163–1175, 2011.

[47] Anna L Herring, FJ Gilby, Zhe Li, JE McClure, Michael Turner, JP Veldkamp, L Beeching, and AP Sheppard. Observations of nonwetting phase snap-off during drainage. *Advances in Water Resources*, 121:32–43, 2018.

[48] Mohammad Heshmati and Mohammad Piri. Interfacial boundary conditions and residual trapping: A pore-scale investigation of the effects of wetting phase flow rate and viscosity using micro-particle image velocimetry. *Fuel*, 224:560–578, 2018.

[49] Herbert E. Huppert and Jerome A. Neufeld. The fluid mechanics of carbon dioxide sequestration. *Annual Review of Fluid Mechanics*, 46(1):255–272, 2014.

[50] Jumana Hussary, Adel Alowaisy, Noriyuki Yasufuku, Ryohei Ishikura, and Monther Abdelhadi. Pore structure and falling rate stage of evaporation in homogeneous sandy soil profiles. *Soils and Foundations*, 62(2):101108, 2022.

[51] Ciprian Iliescu, Bangtao Chen, and Jianmin Miao. On the wet etching of pyrex glass. *Sensors and actuators A: Physical*, 143(1):154–161, 2008.

[52] Janine Jansen, Ferry PW Melchels, Dirk W Grijpma, and Jan Feijen. Fumaric acid monoethyl ester-functionalized poly (d, l-lactide)/n-vinyl-2-pyrrolidone resins for the preparation of tissue engineering scaffolds by stereolithography. *Biomacromolecules*, 10(2):214–220, 2009.

[53] Zhijian Jia, Qun Fang, and Zhao-Lun Fang. Bonding of glass microfluidic chips at room temperatures. *Analytical chemistry*, 76:5597–602, 09 2004.

[54] Jairam Kamath and Catherine Laroche. Laboratory-based evaluation of gas well deliverability loss caused by water blocking. *SPE Journal*, 8(01):71–80, 2003.

[55] NK Karadimitriou and SM Hassanizadeh. A review of micromodels and their use in two-phase flow studies. *Vadose Zone Journal*, 11(3), 2012.

[56] Md Azharul Karim and M.N.A. Hawlader. Drying characteristics of banana: theoretical modelling and experimental validation. *Journal of Food Engineering*, 70(1):35–45, 2005.

[57] Gabriel G Katul and Marc B Parlange. A penman-brutsaert model for wet surface evaporation. *Water Resources Research*, 28(1):121–126, 1992.

[58] Farzan Kazemifar, Gianluca Blois, Dimitrios C Kyritsis, and Kenneth T Christensen. A methodology for velocity field measurement in multiphase high-pressure flow of co2 and water in micromodels. *Water Resources Research*, 51(4):3017–3029, 2015.

[59] Farzan Kazemifar, Gianluca Blois, Dimitrios C Kyritsis, and Kenneth T Christensen. Quantifying the flow dynamics of supercritical co2–water displacement in a 2d porous micromodel using fluorescent microscopy and microscopic piv. *Advances in Water Resources*, 95:352–368, 2016.

[60] K Khanafer and K Vafai. The role of porous media in biomedical engineering as related to magnetic resonance imaging and drug delivery. *Heat and mass transfer*, 42(10):939–953, 2006.

[61] Mohamed Khayet and Takeshi Matsuura. Pervaporation and vacuum membrane distillation processes: modeling and experiments. *AIChE journal*, 50(8):1697–1712, 2004.

[62] E. Korin, I. Ladizhensky, and E. Korngold. Hydrophilic hollow fiber membranes for water desalination by the pervaporation method. *Chemical Engineering and Processing: Process Intensification*, 35(6):451–457, 1996.

[63] Jacob M LaManna, James V Bothe Jr, Feng Yuan Zhang, and Matthew M Mench. Measurement of capillary pressure in fuel cell diffusion media, micro-porous layers, catalyst layers, and interfaces. *Journal of Power Sources*, 271:180–186, 2014.

[64] Duc Le, Hai Hoang, and Jagannathan Mahadevan. Impact of capillary-driven liquid films on salt crystallization. *Transport in porous media*, 80:229–252, 2009.

[65] Peter Lehmann, Shmuel Assouline, and Dani Or. Characteristic lengths affecting evaporative drying of porous media. *Physical Review E*, 77(5):056309, 2008.

[66] Kin Fong Lei. Materials and fabrication techniques for nano-and microfluidic devices. *Microfluidics in Detection Science: Lab-on-a-Chip Technologies; Labeed, FH, Fatoyinbo, HO, Eds*, pages 1–28, 2014.

[67] Andrew P Leis, Sven Schlicher, Hilmar Franke, and Martin Strathmann. Optically transparent porous medium for nondestructive studies of microbial biofilm architecture and transport dynamics. *Applied and environmental microbiology*, 71(8):4801–4808, 2005.

[68] I. Lesov, S. Tcholakova, and N. Denkov. Drying of particle-loaded foams for production of porous materials: mechanism and theoretical modeling. *RSC Adv.*, 4:811–823, 2014.

[69] Yaofa Li, Gianluca Blois, Farzan Kazemifar, and Kenneth T. Christensen. High-speed quantification of pore-scale multiphase flow of water and supercritical co2 in 2-d heterogeneous porous micromodels: Flow regimes and interface dynamics. *Water Resources Research*, 55(5):3758–3779, 2019.

[70] Yaofa Li, Gianluca Blois, Farzan Kazemifar, Razin S Molla, and Kenneth T Christensen. Pore-scale dynamics of liquid co2–water displacement in 2d axisymmetric porous micromodels under strong drainage and weak imbibition conditions: High-speed μpiv measurements. *Frontiers in Water*, 3:710370, 2021.

[71] Yaofa Li, Gianluca Blois, Farzan Kazemifar, Razin S. Molla, and Kenneth T. Christensen. Pore-scale dynamics of liquid co2–water displacement in 2d axisymmetric porous micromodels under strong drainage and weak imbibition conditions: High-speed piv measurements. *Frontiers in Water*, 3, 2021.

[72] AI Liapis and R Bruttini. A theory for the primary and secondary drying stages of the freeze-drying of pharmaceutical crystalline and amorphous solutes: comparison between experimental data and theory. *Separations Technology*, 4(3):144–155, 1994.

[73] Horst Liebersbach, Bernd Steingrobe, and Norbert Claassen. Roots regulate ion transport in the rhizosphere to counteract reduced mobility in dry soil. *Plant and Soil*, 260:79–88, 2004.

[74] Jagannathan Mahadevan and Mukul M Sharma. Clean-up of water blocks in low permeability formations. In *SPE Annual Technical Conference and Exhibition?*, pages SPE–84216. SPE, 2003.

[75] Jagannathan Mahadevan, Mukul M Sharma, and Yannis C Yortsos. Flow-through drying of porous media. *AIChE journal*, 52(7):2367–2380, 2006.

[76] Jagannathan Mahadevan, Mukul M Sharma, and Yannis C Yortsos. Water removal from porous media by gas injection: experiments and simulation. *Transport in Porous Media*, 66:287–309, 2007.

[77] Franziska Moebius and Dani Or. Interfacial jumps and pressure bursts during fluid displacement in interacting irregular capillaries. *Journal of colloid and interface science*, 377(1):406–415, 2012.

[78] Franziska Moebius and Dani Or. Pore scale dynamics underlying the motion of drainage fronts in porous media. *Water Resources Research*, 50(11):8441–8457, 2014.

[79] Razin Molla and Yaofa Li. Non-hysteretic capillary pressure functional form in two-phase flow in porous media: An experimental investigation using 2d porous micromodels. In *AGU Fall Meeting Abstracts*, volume 2021, pages H22D–02, 2021.

[80] Séverine Thérèse FC Mortier, Thomas De Beer, Krist V Gernaey, Jean Paul Remon, Chris Vervaet, and Ingmar Nopens. Mechanistic modelling of fluidized bed drying processes of wet porous granules: a review. *European journal of pharmaceutics and biopharmaceutics*, 79(2):205–225, 2011.

[81] Mehdi Mosharaf-Dehkordi. A fully coupled porous media and channels flow approach for simulation of blood and bile flow through the liver lobules. *Computer Methods in Biomechanics and Biomedical Engineering*, 22(9):901–915, 2019.

[82] Minh-Hue Nguyen and William E Price. Air-drying of banana: Influence of experimental parameters, slab thickness, banana maturity and harvesting season. *Journal of food engineering*, 79(1):200–207, 2007.

[83] Perley Gilman Nutting. Physical analysis of oil sands. *AAPG Bulletin*, 14(10):1337–1349, 1930.

[84] JM Oades and AG Waters. Aggregate hierarchy in soils. *Soil Research*, 29(6):815–828, 1991.

[85] Zdzislaw Pakowski and Arun S Mujumdar. Drying of pharmaceutical products. *Handbook of Industrial Drying*, 2:743–773, 1995.

[86] HL Penman. Gas and vapour movements in the soil: I. the diffusion of vapours through porous solids. *The Journal of Agricultural Science*, 30(3):437–462, 1940.

[87] Frédéric Plourde and Marc Prat. Pore network simulations of drying of capillary porous media. influence of thermal gradients. *International journal of heat and mass transfer*, 46(7):1293–1307, 2003.

[88] M Prat and F Bouleux. Drying of capillary porous media with a stabilized front in two dimensions. *Physical Review E*, 60(5):5647, 1999.

[89] Marc Prat. Percolation model of drying under isothermal conditions in porous media. *International Journal of Multiphase Flow*, 19(4):691–704, 1993.

[90] Marc Prat. Recent advances in pore-scale models for drying of porous media. *Chemical engineering journal*, 86(1-2):153–164, 2002.

[91] Milivoj Radojčin, Ivan Pavkov, Danijela Bursać Kovačević, Predrag Putnik, Artur Wiktor, Zoran Stamenković, Krstan Kešelj, and Attila Gere. Effect of selected drying methods and emerging drying intensification technologies on the quality of dried fruit: A review. *Processes*, 9(1), 2021.

[92] Nishagar Raventhiran, Razin Sazzad Molla, Kshithij Nandishwara, Erick Johnson, and Yaofa Li. Design and fabrication of a novel on-chip pressure sensor for microchannels. *Lab on a Chip*, 22(22):4306–4316, 2022.

[93] Sylian J Rodríguez and Paul L Bishop. Three-dimensional quantification of soil biofilms using image analysis. *Environmental Engineering Science*, 24(1):96–103, 2007.

[94] J. Rouquerol, D. Avnir, C. W. Fairbridge, D. H. Everett, J. M. Haynes, N. Pernicone, J. D. F. Ramsay, K. S. W. Sing, and K. K. Unger. Recommendations for the characterization of porous solids (technical report). *Pure and Applied Chemistry*, 66(8):1739–1758, 1994.

[95] Guido Daniel Salvucci and Dara Entekhabi. Equivalent steady soil moisture profile and the time compression approximation in water balance modeling. *Water Resources Research*, 30(10):2737–2749, 1994.

[96] Juan G Santiago, Steve T Wereley, Carl D Meinhart, DJ Beebe, and Ronald J Adrian. A particle image velocimetry system for microfluidics. *Experiments in fluids*, 25(4):316–319, 1998.

[97] GC Sarti, C Gostoli, and S Bandini. Extraction of organic components from aqueous streams by vacuum membrane distillation. *Journal of membrane science*, 80(1):21–33, 1993.

[98] George W Scherer. Theory of drying. *Journal of the American Ceramic Society*, 73(1):3–14, 1990.

[99] Steffen Schlüter, S Berg, M Rücker, RT Armstrong, H-J Vogel, R Hilfer, and D Wildenschild. Pore-scale displacement mechanisms as a source of hysteresis for two-phase flow in porous media. *Water Resources Research*, 52(3):2194–2205, 2016.

[100] Th K Sherwood. The drying of solids—i. *Industrial & Engineering Chemistry*, 21(1):12–16, 1929.

[101] Nima Shokri. Pore-scale dynamics of salt transport and distribution in drying porous media. *Physics of Fluids*, 26(1), 2014.

[102] Nima Shokri, Peter Lehmann, and Dani Or. Critical evaluation of enhancement factors for vapor transport through unsaturated porous media. *Water resources research*, 45(10), 2009.

[103] Nima Shokri and Dani Or. What determines drying rates at the onset of diffusion controlled stage-2 evaporation from porous media? *Water Resources Research*, 47(9), 2011.

[104] W James Shuttleworth. Evaporation. 1979.

[105] Rajveer Singh, Mayandi Sivaguru, Glenn A Fried, Bruce W Fouke, Robert A Sanford, Martin Carrera, and Charles J Werth. Real rock-microfluidic flow cell: A test bed for real-time in situ analysis of flow, transport, and reaction in a subsurface reactive transport environment. *Journal of contaminant hydrology*, 204:28–39, 2017.

[106] JAET Six, Edward T Elliott, and Keith Paustian. Soil macroaggregate turnover and microaggregate formation: a mechanism for c sequestration under no-tillage agriculture. *Soil Biology and Biochemistry*, 32(14):2099–2103, 2000.

[107] Johan Six, Heleen Bossuyt, Steven Degryze, and Karolien Denef. A history of research on the link between (micro) aggregates, soil biota, and soil organic matter dynamics. *Soil and tillage research*, 79(1):7–31, 2004.

[108] Krzysztof Sollohub and Krzysztof Cal. Spray drying technique: Ii. current applications in pharmaceutical technology. *Journal of pharmaceutical sciences*, 99(2):587–597, 2010.

[109] Wen Song, Thomas W de Haas, Hossein Fadaei, and David Sinton. Chip-off-the-old-rock: the study of reservoir-relevant geological processes with real-rock micromodels. *Lab on a Chip*, 14(22):4382–4390, 2014.

[110] Mutsumi Suzuki and Siro Maeda. On the mechanism of drying of granular beds mass transfer from discontinuous source. *Journal of chemical engineering of Japan*, 1(1):26–31, 1968.

[111] J. M. TISDALL and J. M. OADES. Organic matter and water-stable aggregates in soils. *Journal of Soil Science*, 33(2):141–163.

[112] J Van Brakel. Advances in drying. *Hemisphere, Chap Mass transfer in convective drying*, pages 217–267, 1980.

[113] M. van der Waarden, A.L.A.M. Bridié, and W.M. Groenewoud. Transport of mineral oil components to groundwater—i: Model experiments on the transfer of hydrocarbons from a residual oil zone to trickling water. *Water Research*, 5(5):213–226, 1971.

[114] CM Van't Land. *Drying in the process industry*. John Wiley & Sons, 2011.

[115] Nicole Vorhauer, QT Tran, Thomas Metzger, Evangelos Tsotsas, and Marc Prat. Experimental investigation of drying in a model porous medium: influence of thermal gradients. *Drying Technology*, 31(8):920–929, 2013.

[116] Nicole Vorhauer, YJ Wang, A Kharaghani, Evangelos Tsotsas, and Marc Prat. Drying with formation of capillary rings in a model porous medium. *Transport in Porous Media*, 110:197–223, 2015.

[117] Robert H Walters, Bakul Bhatnagar, Serguei Tchessalov, Ken-Ichi Izutsu, Kouhei Tsumoto, and Satoshi Ohtake. Next generation drying technologies for pharmaceutical applications. *Journal of pharmaceutical sciences*, 103(9):2673–2695, 2014.

[118] Jingbo Wang, Dian Tanuwidjaja, Subir Bhattacharjee, Arian Edalat, David Jassby, and Eric M. V. Hoek. Produced water desalination via pervaporative distillation. *Water*, 12(12), 2020.

[119] Donna J Webb and Claire M Brown. Epi-fluorescence microscopy. *Cell Imaging Techniques: Methods and Protocols*, pages 29–59, 2013.

[120] J Wei, ZP Wang, H Xie, and Ng Fern Lan. Role of bonding temperature and voltage in silicon-to-glass anodic bonding. In *4th Electronics Packaging Technology Conference, 2002.*, pages 85–90. IEEE, 2002.

[121] Kilian Weishaupt, Timo Koch, and Rainer Helmig. A fully implicit coupled pore-network/free-flow model for the pore-scale simulation of drying processes. *Drying Technology*, 40(4):697–718, 2022.

[122] Jerry Westerweel. Fundamentals of digital particle image velocimetry. *Measurement science and technology*, 8(12):1379, 1997.

[123] David Wilkinson. Percolation model of immiscible displacement in the presence of buoyancy forces. *Physical Review A*, 30(1):520, 1984.

[124] Regina L. Wilpiszeski, Jayde A. Aufrecht, Scott T. Retterer, Matthew B. Sullivan, David E. Graham, Eric M. Pierce, Olivier D. Zablocki, Anthony V. Palumbo, and Dwayne A. Elias. Soil aggregate microbial communities: Towards understanding microbiome interactions at biologically relevant scales. *Applied and Environmental Microbiology*, 85(14):e00324–19, 2019.

[125] RD Wyckoff, HG Botset, Morris Muskat, and DW Reed. The measurement of the permeability of porous media for homogeneous fluids. *Review of Scientific Instruments*, 4(7):394–405, 1933.

[126] Benyamin Yadali Jamaloei and Riyaz Kharrat. Analysis of microscopic displacement mechanisms of dilute surfactant flooding in oil-wet and water-wet porous media. *Transport in porous media*, 81:1–19, 2010.

[127] Yuniati Zevi, Annette Dathe, John F McCarthy, Brian K Richards, and Tammo S Steenhuis. Distribution of colloid particles onto interfaces in partially saturated sand. *Environmental science & technology*, 39(18):7055–7064, 2005.

[128] Qiulan Zhang, NK Karadimitriou, SM Hassanizadeh, PJ Kleingeld, and A Imhof. Study of colloids transport during two-phase flow using a novel polydimethylsiloxane micro-model. *Journal of colloid and interface science*, 401:141–147, 2013.

[129] Xiang Zhou, Qingwang Yuan, Yizhong Zhang, Hanyi Wang, Fanhua Zeng, and Liehui Zhang. Performance evaluation of co2 flooding process in tight oil reservoir via experimental and numerical simulation studies. *Fuel*, 236:730–746, 2019.

APPENDIX

ESSENTIAL CODES

MATLAB code to align the mask pattern to the raw reference frame

```
global rout
global RawIm
global FixedRegions
global MaskSub1
global MaskSub2
global MaskSub3
global MaskSub4
global MaskSub5
global MaskSub6
global MaskSub7
global MaskSub8
global MaskSub9

global FixedRegion1
global FixedRegion2
global FixedRegion3
global FixedRegion4
global FixedRegion5
global FixedRegion6
global FixedRegion7
global FixedRegion8
global FixedRegion9

case_no='Case 1';

%%
[TifLoc, TifPrefix, rout, FrameInfo, FixedRegions, MovingRegions,
   MaskLoc] = CaseAndParameter( case_no );

FrameRef=FrameInfo(2);
PoreMask=imread(MaskLoc);
PoreMask=imbinarize(PoreMask);

FixedRegion1=FixedRegions(1,:);
FixedRegion2=FixedRegions(2,:);
FixedRegion3=FixedRegions(3,:);
FixedRegion4=FixedRegions(4,:);
FixedRegion5=FixedRegions(5,:);
FixedRegion6=FixedRegions(6,:);
FixedRegion7=FixedRegions(7,:);
FixedRegion8=FixedRegions(8,:);
FixedRegion9=FixedRegions(9,:);
```

```
%Prepare 9 reference regions
MaskSub1=PoreMask(FixedRegion1(2)+1:FixedRegion1(2)+FixedRegion1(4),
    FixedRegion1(1)+1:FixedRegion1(1)+FixedRegion1(3));
MaskSub2=PoreMask(FixedRegion2(2)+1:FixedRegion2(2)+FixedRegion2(4),
    FixedRegion2(1)+1:FixedRegion2(1)+FixedRegion2(3));
MaskSub3=PoreMask(FixedRegion3(2)+1:FixedRegion3(2)+FixedRegion3(4),
    FixedRegion3(1)+1:FixedRegion3(1)+FixedRegion3(3));
MaskSub4=PoreMask(FixedRegion4(2)+1:FixedRegion4(2)+FixedRegion4(4),
    FixedRegion4(1)+1:FixedRegion4(1)+FixedRegion4(3));
MaskSub5=PoreMask(FixedRegion5(2)+1:FixedRegion5(2)+FixedRegion5(4),
    FixedRegion5(1)+1:FixedRegion5(1)+FixedRegion5(3));
MaskSub6=PoreMask(FixedRegion6(2)+1:FixedRegion6(2)+FixedRegion6(4),
    FixedRegion6(1)+1:FixedRegion6(1)+FixedRegion6(3));
MaskSub7=PoreMask(FixedRegion7(2)+1:FixedRegion7(2)+FixedRegion7(4),
    FixedRegion7(1)+1:FixedRegion7(1)+FixedRegion7(3));
MaskSub8=PoreMask(FixedRegion8(2)+1:FixedRegion8(2)+FixedRegion8(4),
    FixedRegion8(1)+1:FixedRegion8(1)+FixedRegion8(3));
MaskSub9=PoreMask(FixedRegion9(2)+1:FixedRegion9(2)+FixedRegion9(4),
    FixedRegion9(1)+1:FixedRegion9(1)+FixedRegion9(3));

%Initial postion on the Raw images. These locations are what to be
    adjusted
MovingRegion1=MovingRegions(1,:);
MovingRegion2=MovingRegions(2,:);
MovingRegion3=MovingRegions(3,:);
MovingRegion4=MovingRegions(4,:);
MovingRegion5=MovingRegions(5,:);
MovingRegion6=MovingRegions(6,:);
MovingRegion7=MovingRegions(7,:);
MovingRegion8=MovingRegions(8,:);
MovingRegion9=MovingRegions(9,:);

global x1 y1 w1 h1
global x2 y2 w2 h2
global x3 y3 w3 h3
global x4 y4 w4 h4
global x5 y5 w5 h5
global x6 y6 w6 h6
global x7 y7 w7 h7
global x8 y8 w8 h8
global x9 y9 w9 h9

x1=MovingRegion1(1);
y1=MovingRegion1(2);
w1=MovingRegion1(3);
```

```
h1=MovingRegion1(4);

x2=MovingRegion2(1);
y2=MovingRegion2(2);
w2=MovingRegion2(3);
h2=MovingRegion2(4);

x3=MovingRegion3(1);
y3=MovingRegion3(2);
w3=MovingRegion3(3);
h3=MovingRegion3(4);

x4=MovingRegion4(1);
y4=MovingRegion4(2);
w4=MovingRegion4(3);
h4=MovingRegion4(4);

x5=MovingRegion5(1);
y5=MovingRegion5(2);
w5=MovingRegion5(3);
h5=MovingRegion5(4);

x6=MovingRegion6(1);
y6=MovingRegion6(2);
w6=MovingRegion6(3);
h6=MovingRegion6(4);

x7=MovingRegion7(1);
y7=MovingRegion7(2);
w7=MovingRegion7(3);
h7=MovingRegion7(4);

x8=MovingRegion8(1);
y8=MovingRegion8(2);
w8=MovingRegion8(3);
h8=MovingRegion8(4);

x9=MovingRegion9(1);
y9=MovingRegion9(2);
w9=MovingRegion9(3);
h9=MovingRegion9(4);

%Read in the raw image
[s1]=mkdir(rout,'\GrainAlignment');
[s2]=mkdir(rout);
```

```
[RawIm]=imread([TifLoc,'\',TifPrefix, num2str(FrameRef),'.tif']);

RawIm=double(RawIm);
RawIm(RawIm<500)=1000;
RawIm=RawIm*255/max(max(RawIm));

RawIm=uint8(RawIm);

%%%%%%%%%%%%%%%%%%%%%%%%%%%%%%%%%%%%%%%%%%%%%%%%%%%%%%%%%%%%%%%%%%%%%%%%%%%%
%%%%%%%%%%%%%%%%%%%% Location 1 %%%%%%%%%%%%%%%%%%%%%%%%%%%%%%%%%%%%%%%%%%%
%%%%%%%%%%%%%%%%%%%%%%%%%%%%%%%%%%%%%%%%%%%%%%%%%%%%%%%%%%%%%%%%%%%%%%%%%%%%
%Align the first point
CurrIm=RawIm;
Handle1 = figure(1);
CurrIm(y1+1:y1+h1,x1+1:x1+w1)=uint8(double(CurrIm(y1+1:y1+h1,x1+1:x1+w1
    )).*MaskSub1);
imshow(CurrIm);
title('Use Arrow Buttons to Align the Images. Press Enter When Done!')
% Handle1.Units='normalized';
% Handle1.OuterPosition=[0 0 1 1];
set(Handle1,'KeyPressFcn',@KeyPressCb1) ;

%%%%%%%%%%%%%%%%%%%%%%%%%%%%%%%%%%%%%%%%%%%%%%%%%%%%%%%%%%%%%%%%%%%%%%%%%%%%
%%%%%%%%%%%%%%%%%%%% Location 2 %%%%%%%%%%%%%%%%%%%%%%%%%%%%%%%%%%%%%%%%%%%
%%%%%%%%%%%%%%%%%%%%%%%%%%%%%%%%%%%%%%%%%%%%%%%%%%%%%%%%%%%%%%%%%%%%%%%%%%%%
%Align the first point
CurrIm=RawIm;
Handle2 = figure(2);
CurrIm(y2+1:y2+h2,x2+1:x2+w2)=uint8(double(CurrIm(y2+1:y2+h2,x2+1:x2+w2
    )).*MaskSub2);
imshow(CurrIm);
title('Use Arrow Buttons to Align the Images. Press Enter When Done!')
% Handle2.Units='normalized';
% Handle2.OuterPosition=[0 0 1 1];
set(Handle2,'KeyPressFcn',@KeyPressCb2) ;

%%%%%%%%%%%%%%%%%%%%%%%%%%%%%%%%%%%%%%%%%%%%%%%%%%%%%%%%%%%%%%%%%%%%%%%%%%%%
%%%%%%%%%%%%%%%%%%%% Location 3 %%%%%%%%%%%%%%%%%%%%%%%%%%%%%%%%%%%%%%%%%%%
%%%%%%%%%%%%%%%%%%%%%%%%%%%%%%%%%%%%%%%%%%%%%%%%%%%%%%%%%%%%%%%%%%%%%%%%%%%%
%Align the first point
CurrIm=RawIm;
Handle3 = figure(3);
CurrIm(y3+1:y3+h3,x3+1:x3+w3)=uint8(double(CurrIm(y3+1:y3+h3,x3+1:x3+w3
    )).*MaskSub3);
imshow(CurrIm);
```

```
title('Use␣Arrow␣Buttons␣to␣Align␣the␣Images.␣Press␣Enter␣When␣Done!')
% Handle3.Units='normalized';
% Handle3.OuterPosition=[0 0 1 1];
set(Handle3,'KeyPressFcn',@KeyPressCb3) ;

%%%%%%%%%%%%%%%%%%%%%%%%%%%%%%%%%%%%%%%%%%%%%%%%%%%%%%%%%%%%%%%%%%%%%%%%%%%
%%%%%%%%%%%%%%%%%%%% Location 4 %%%%%%%%%%%%%%%%%%%%%%%%%%%%%%%%%%%%%%%%%%
%%%%%%%%%%%%%%%%%%%%%%%%%%%%%%%%%%%%%%%%%%%%%%%%%%%%%%%%%%%%%%%%%%%%%%%%%%%
%Align the first point
CurrIm=RawIm;
Handle4 = figure(4);
CurrIm(y4+1:y4+h4,x4+1:x4+w4)=uint8(double(CurrIm(y4+1:y4+h4,x4+1:x4+w4
    )).*MaskSub4);
imshow(CurrIm);
title('Use␣Arrow␣Buttons␣to␣Align␣the␣Images.␣Press␣Enter␣When␣Done!')
% Handle4.Units='normalized';
% Handle4.OuterPosition=[0 0 1 1];
set(Handle4,'KeyPressFcn',@KeyPressCb4) ;

%%%%%%%%%%%%%%%%%%%%%%%%%%%%%%%%%%%%%%%%%%%%%%%%%%%%%%%%%%%%%%%%%%%%%%%%%%%
%%%%%%%%%%%%%%%%%%%% Location 5 %%%%%%%%%%%%%%%%%%%%%%%%%%%%%%%%%%%%%%%%%%
%%%%%%%%%%%%%%%%%%%%%%%%%%%%%%%%%%%%%%%%%%%%%%%%%%%%%%%%%%%%%%%%%%%%%%%%%%%
%Align the first point
CurrIm=RawIm;
Handle5 = figure(5);
CurrIm(y5+1:y5+h5,x5+1:x5+w5)=uint8(double(CurrIm(y5+1:y5+h5,x5+1:x5+w5
    )).*MaskSub5);
imshow(CurrIm);
title('Use␣Arrow␣Buttons␣to␣Align␣the␣Images.␣Press␣Enter␣When␣Done!')
% Handle5.Units='normalized';
% Handle5.OuterPosition=[0 0 1 1];
set(Handle5,'KeyPressFcn',@KeyPressCb5) ;

%%%%%%%%%%%%%%%%%%%%%%%%%%%%%%%%%%%%%%%%%%%%%%%%%%%%%%%%%%%%%%%%%%%%%%%%%%%
%%%%%%%%%%%%%%%%%%%% Location 6 %%%%%%%%%%%%%%%%%%%%%%%%%%%%%%%%%%%%%%%%%%
%%%%%%%%%%%%%%%%%%%%%%%%%%%%%%%%%%%%%%%%%%%%%%%%%%%%%%%%%%%%%%%%%%%%%%%%%%%
%Align the first point
CurrIm=RawIm;
Handle6 = figure(6);
CurrIm(y6+1:y6+h6,x6+1:x6+w6)=uint8(double(CurrIm(y6+1:y6+h6,x6+1:x6+w6
    )).*MaskSub6);
imshow(CurrIm);
title('Use␣Arrow␣Buttons␣to␣Align␣the␣Images.␣Press␣Enter␣When␣Done!')
% Handle6.Units='normalized';
% Handle6.OuterPosition=[0 0 1 1];
```

```
set(Handle6,'KeyPressFcn',@KeyPressCb6) ;

%%%%%%%%%%%%%%%%%%%%%%%%%%%%%%%%%%%%%%%%%%%%%%%%%%%%%%%%%%%%%%%%%%%%%%%%%%%%
%%%%%%%%%%%%%%%%%%%% Location 7 %%%%%%%%%%%%%%%%%%%%%%%%%%%%%%%%%%%%%%%%%%%
%%%%%%%%%%%%%%%%%%%%%%%%%%%%%%%%%%%%%%%%%%%%%%%%%%%%%%%%%%%%%%%%%%%%%%%%%%%%
%Align the first point
CurrIm=RawIm;
Handle7 = figure(7);
CurrIm(y7+1:y7+h7,x7+1:x7+w7)=uint8(double(CurrIm(y7+1:y7+h7,x7+1:x7+w7
    )).*MaskSub7);
imshow(CurrIm);
title('Use Arrow Buttons to Align the Images. Press Enter When Done!')
% Handle7.Units='normalized';
% Handle7.OuterPosition=[0 0 1 1];
set(Handle7,'KeyPressFcn',@KeyPressCb7) ;

%%%%%%%%%%%%%%%%%%%%%%%%%%%%%%%%%%%%%%%%%%%%%%%%%%%%%%%%%%%%%%%%%%%%%%%%%%%%
%%%%%%%%%%%%%%%%%%%% Location 8 %%%%%%%%%%%%%%%%%%%%%%%%%%%%%%%%%%%%%%%%%%%
%%%%%%%%%%%%%%%%%%%%%%%%%%%%%%%%%%%%%%%%%%%%%%%%%%%%%%%%%%%%%%%%%%%%%%%%%%%%
%Align the first point
CurrIm=RawIm;
Handle8 = figure(8);
CurrIm(y8+1:y8+h8,x8+1:x8+w8)=uint8(double(CurrIm(y8+1:y8+h8,x8+1:x8+w8
    )).*MaskSub8);
imshow(CurrIm);
title('Use Arrow Buttons to Align the Images. Press Enter When Done!')
% Handle8.Units='normalized';
% Handle8.OuterPosition=[0 0 1 1];
set(Handle8,'KeyPressFcn',@KeyPressCb8) ;

%%%%%%%%%%%%%%%%%%%%%%%%%%%%%%%%%%%%%%%%%%%%%%%%%%%%%%%%%%%%%%%%%%%%%%%%%%%%
%%%%%%%%%%%%%%%%%%%% Location 9 %%%%%%%%%%%%%%%%%%%%%%%%%%%%%%%%%%%%%%%%%%%
%%%%%%%%%%%%%%%%%%%%%%%%%%%%%%%%%%%%%%%%%%%%%%%%%%%%%%%%%%%%%%%%%%%%%%%%%%%%
%Align the first point
CurrIm=RawIm;
Handle9 = figure(9);
CurrIm(y9+1:y9+h9,x9+1:x9+w9)=uint8(double(CurrIm(y9+1:y9+h9,x9+1:x9+w9
    )).*MaskSub9);
imshow(CurrIm);
title('Use Arrow Buttons to Align the Images. Press Enter When Done!')
% Handle9.Units='normalized';
% Handle9.OuterPosition=[0 0 1 1];
set(Handle9,'KeyPressFcn',@KeyPressCb9) ;

function KeyPressCb1(~,evnt1)
```

```
global x1
global y1
global w1
global h1
global rout
global RawIm
global MaskSub1
global FixedRegion1
fprintf('key pressed: %s\n',evnt1.Key);
CurrIm=RawIm;

if strcmpi(evnt1.Key,'leftarrow')
    x1=x1-1;
    CurrIm(y1+1:y1+h1,x1+1:x1+w1)=uint8(double(CurrIm(y1+1:y1+h1,x1+1:
        x1+w1)).*MaskSub1);
    imshow(CurrIm(y1+1:y1+h1,x1+1:x1+w1),'InitialMagnification',200);
    title('Use Arrow Buttons to Align the Images. Press Enter When Done
        !')
    % imshow(CurrIm,'InitialMagnification');

elseif strcmpi(evnt1.Key,'rightarrow')
    x1=x1+1;
    CurrIm(y1+1:y1+h1,x1+1:x1+w1)=uint8(double(CurrIm(y1+1:y1+h1,x1+1:
        x1+w1)).*MaskSub1);
    imshow(CurrIm(y1+1:y1+h1,x1+1:x1+w1),'InitialMagnification',200);
    title('Use Arrow Buttons to Align the Images. Press Enter When Done
        !')
    % imshow(CurrIm,'InitialMagnification');
elseif strcmpi(evnt1.Key,'uparrow')
    y1=y1-1;
    CurrIm(y1+1:y1+h1,x1+1:x1+w1)=uint8(double(CurrIm(y1+1:y1+h1,x1+1:
        x1+w1)).*MaskSub1);
    imshow(CurrIm(y1+1:y1+h1,x1+1:x1+w1),'InitialMagnification',200);
    title('Use Arrow Buttons to Align the Images. Press Enter When Done
        !')
    % imshow(CurrIm,'InitialMagnification');
elseif strcmpi(evnt1.Key,'downarrow')
    y1=y1+1;
    CurrIm(y1+1:y1+h1,x1+1:x1+w1)=uint8(double(CurrIm(y1+1:y1+h1,x1+1:
        x1+w1)).*MaskSub1);
    imshow(CurrIm(y1+1:y1+h1,x1+1:x1+w1),'InitialMagnification',200);
    title('Use Arrow Buttons to Align the Images. Press Enter When Done
        !')
    % imshow(CurrIm,'InitialMagnification');
elseif strcmpi(evnt1.Key,'return')
```

```
    answer = questdlg('Do You Want to Include It (Click No if You
        Cannot Align It)?','Is the Point Useful?','Yes','No','Yes');
    switch answer
        case 'Yes'
            Use1=1;
        case 'No'
            Use1=0;
    end
    xlswrite([rout,'\GrainAlignment','\Location1.xlsx'],[{'ImX';'ImY';'
        ImW';'ImH';'MaskX';'MaskY';'MaskW';'MaskH';'Use'}, num2cell([x1;
         y1; w1; h1;FixedRegion1';Use1;]) ]);
    hh = msgbox('Location 1 Alignment Done. Close the Figure and
        Proceed to the Next!');
end
end

function KeyPressCb2(~,evnt2)
global x2
global y2
global w2
global h2
global rout
global RawIm
global MaskSub2
global FixedRegion2
fprintf('key pressed: %s\n',evnt2.Key);
CurrIm=RawIm;

if strcmpi(evnt2.Key,'leftarrow')
    x2=x2-1;
    CurrIm(y2+1:y2+h2,x2+1:x2+w2)=uint8(double(CurrIm(y2+1:y2+h2,x2+1:
        x2+w2)).*MaskSub2);
    imshow(CurrIm(y2+1:y2+h2,x2+1:x2+w2),'InitialMagnification',200);
    title('Use Arrow Buttons to Align the Images. Press Enter When Done
        !')
    %       imshow(CurrIm);

elseif strcmpi(evnt2.Key,'rightarrow')
    x2=x2+1;
    CurrIm(y2+1:y2+h2,x2+1:x2+w2)=uint8(double(CurrIm(y2+1:y2+h2,x2+1:
        x2+w2)).*MaskSub2);
    imshow(CurrIm(y2+1:y2+h2,x2+1:x2+w2),'InitialMagnification',200);
    title('Use Arrow Buttons to Align the Images. Press Enter When Done
        !')
```

```
    %       imshow(CurrIm);
elseif strcmpi(evnt2.Key,'uparrow')
    y2=y2-1;
    CurrIm(y2+1:y2+h2,x2+1:x2+w2)=uint8(double(CurrIm(y2+1:y2+h2,x2+1:
        x2+w2)).*MaskSub2);
    imshow(CurrIm(y2+1:y2+h2,x2+1:x2+w2),'InitialMagnification',200);
    title('Use Arrow Buttons to Align the Images. Press Enter When Done
        !')
    %       imshow(CurrIm);
elseif strcmpi(evnt2.Key,'downarrow')
    y2=y2+1;
    CurrIm(y2+1:y2+h2,x2+1:x2+w2)=uint8(double(CurrIm(y2+1:y2+h2,x2+1:
        x2+w2)).*MaskSub2);
    imshow(CurrIm(y2+1:y2+h2,x2+1:x2+w2),'InitialMagnification',200);
    title('Use Arrow Buttons to Align the Images. Press Enter When Done
        !')
    %       imshow(CurrIm);
elseif strcmpi(evnt2.Key,'return')

    answer = questdlg('Do You Want to Include It (Click No if You
        Cannot Align It)?','Is the Point Useful?','Yes','No','Yes');
    switch answer
        case 'Yes'
            Use2=1;
        case 'No'
            Use2=0;
    end
    xlswrite([rout,'\GrainAlignment','\Location2.xlsx'],[{'ImX';'ImY';'
        ImW';'ImH';'MaskX';'MaskY';'MaskW';'MaskH';'Use'}, num2cell([x2;
         y2; w2; h2;FixedRegion2';Use2;])]);
    hh = msgbox('Location 2 Alignment Done. Close the Figure and
        Proceed to the Next!');
end
end

function KeyPressCb3(~,evnt3)
global x3
global y3
global w3
global h3
global rout
global RawIm
global MaskSub3
global FixedRegion3
fprintf('key pressed: %s\n',evnt3.Key);
```

```
CurrIm=RawIm;

if strcmpi(evnt3.Key,'leftarrow')
    x3=x3-1;
    CurrIm(y3+1:y3+h3,x3+1:x3+w3)=uint8(double(CurrIm(y3+1:y3+h3,x3+1:
        x3+w3)).*MaskSub3);
    imshow(CurrIm(y3+1:y3+h3,x3+1:x3+w3),'InitialMagnification',200);
    title('Use Arrow Buttons to Align the Images. Press Enter When Done
        !')
    %           imshow(CurrIm);

elseif strcmpi(evnt3.Key,'rightarrow')
    x3=x3+1;
    CurrIm(y3+1:y3+h3,x3+1:x3+w3)=uint8(double(CurrIm(y3+1:y3+h3,x3+1:
        x3+w3)).*MaskSub3);
    imshow(CurrIm(y3+1:y3+h3,x3+1:x3+w3),'InitialMagnification',200);
    title('Use Arrow Buttons to Align the Images. Press Enter When Done
        !')
    %           imshow(CurrIm);
elseif strcmpi(evnt3.Key,'uparrow')
    y3=y3-1;
    CurrIm(y3+1:y3+h3,x3+1:x3+w3)=uint8(double(CurrIm(y3+1:y3+h3,x3+1:
        x3+w3)).*MaskSub3);
    imshow(CurrIm(y3+1:y3+h3,x3+1:x3+w3),'InitialMagnification',200);
    title('Use Arrow Buttons to Align the Images. Press Enter When Done
        !')
    %           imshow(CurrIm);
elseif strcmpi(evnt3.Key,'downarrow')
    y3=y3+1;
    CurrIm(y3+1:y3+h3,x3+1:x3+w3)=uint8(double(CurrIm(y3+1:y3+h3,x3+1:
        x3+w3)).*MaskSub3);
    imshow(CurrIm(y3+1:y3+h3,x3+1:x3+w3),'InitialMagnification',200);
    title('Use Arrow Buttons to Align the Images. Press Enter When Done
        !')
    %           imshow(CurrIm);
elseif strcmpi(evnt3.Key,'return')
    answer = questdlg('Do You Want to Include It (Click No if You
       Cannot Align It)?','Is the Point Useful?','Yes','No','Yes');
    switch answer
        case 'Yes'
            Use3=1;
        case 'No'
            Use3=0;
    end
    xlswrite([rout,'\GrainAlignment','\Location3.xlsx'],[{'ImX';'ImY';'
```

```
        ImW';'ImH';'MaskX';'MaskY';'MaskW';'MaskH';'Use'}, num2cell([x3;
         y3; w3; h3;FixedRegion3';Use3;])]);
    hh = msgbox('Location 3 Alignment Done. Close the Figure and
        Proceed to the Next!');
end
end

function KeyPressCb4(~,evnt4)
global x4
global y4
global w4
global h4
global rout
global RawIm
global MaskSub4
global FixedRegion4
fprintf('key pressed: %s\n',evnt4.Key);
CurrIm=RawIm;

if strcmpi(evnt4.Key,'leftarrow')
    x4=x4-1;
    CurrIm(y4+1:y4+h4,x4+1:x4+w4)=uint8(double(CurrIm(y4+1:y4+h4,x4+1:
        x4+w4)).*MaskSub4);
    imshow(CurrIm(y4+1:y4+h4,x4+1:x4+w4),'InitialMagnification',200);
    title('Use Arrow Buttons to Align the Images. Press Enter When Done
        !')
    %           imshow(CurrIm);
elseif strcmpi(evnt4.Key,'rightarrow')
    x4=x4+1;
    CurrIm(y4+1:y4+h4,x4+1:x4+w4)=uint8(double(CurrIm(y4+1:y4+h4,x4+1:
        x4+w4)).*MaskSub4);
    imshow(CurrIm(y4+1:y4+h4,x4+1:x4+w4),'InitialMagnification',200);
    title('Use Arrow Buttons to Align the Images. Press Enter When Done
        !')
    %           imshow(CurrIm);
elseif strcmpi(evnt4.Key,'uparrow')
    y4=y4-1;
    CurrIm(y4+1:y4+h4,x4+1:x4+w4)=uint8(double(CurrIm(y4+1:y4+h4,x4+1:
        x4+w4)).*MaskSub4);
    imshow(CurrIm(y4+1:y4+h4,x4+1:x4+w4),'InitialMagnification',200);
    title('Use Arrow Buttons to Align the Images. Press Enter When Done
        !')
    %           imshow(CurrIm);
elseif strcmpi(evnt4.Key,'downarrow')
    y4=y4+1;
```

```
    CurrIm(y4+1:y4+h4,x4+1:x4+w4)=uint8(double(CurrIm(y4+1:y4+h4,x4+1:
        x4+w4)).*MaskSub4);
    imshow(CurrIm(y4+1:y4+h4,x4+1:x4+w4),'InitialMagnification',200);
    title('Use Arrow Buttons to Align the Images. Press Enter When Done
        !')
    %           imshow(CurrIm);
elseif strcmpi(evnt4.Key,'return')
    answer = questdlg('Do You Want to Include It (Click No if You
        Cannot Align It)?','Is the Point Useful?','Yes','No','Yes');
    switch answer
        case 'Yes'
            Use4=1;
        case 'No'
            Use4=0;
    end
    xlswrite([rout,'\GrainAlignment','\Location4.xlsx'],[{'ImX';'ImY';'
        ImW';'ImH';'MaskX';'MaskY';'MaskW';'MaskH';'Use'}, num2cell([x4;
         y4; w4; h4;FixedRegion4'; Use4])]);
    hh = msgbox('Location 4 Alignment Done. Close the Figure and
        Proceed to the Next!');
end
end

function KeyPressCb5(~,evnt5)
global x5
global y5
global w5
global h5
global rout
global RawIm
global MaskSub5
global FixedRegion5
fprintf('key pressed: %s\n',evnt5.Key);
CurrIm=RawIm;

if strcmpi(evnt5.Key,'leftarrow')
    x5=x5-1;
    CurrIm(y5+1:y5+h5,x5+1:x5+w5)=uint8(double(CurrIm(y5+1:y5+h5,x5+1:
        x5+w5)).*MaskSub5);
    imshow(CurrIm(y5+1:y5+h5,x5+1:x5+w5),'InitialMagnification',200);
    title('Use Arrow Buttons to Align the Images. Press Enter When Done
        !')
    %           imshow(CurrIm);
elseif strcmpi(evnt5.Key,'rightarrow')
    x5=x5+1;
```

```
    CurrIm(y5+1:y5+h5,x5+1:x5+w5)=uint8(double(CurrIm(y5+1:y5+h5,x5+1:
        x5+w5)).*MaskSub5);
    imshow(CurrIm(y5+1:y5+h5,x5+1:x5+w5),'InitialMagnification',200);
    title('Use Arrow Buttons to Align the Images. Press Enter When Done
        !')
    %           imshow(CurrIm);
elseif strcmpi(evnt5.Key,'uparrow')
    y5=y5-1;
    CurrIm(y5+1:y5+h5,x5+1:x5+w5)=uint8(double(CurrIm(y5+1:y5+h5,x5+1:
        x5+w5)).*MaskSub5);
    imshow(CurrIm(y5+1:y5+h5,x5+1:x5+w5),'InitialMagnification',200);
    title('Use Arrow Buttons to Align the Images. Press Enter When Done
        !')
    %           imshow(CurrIm);
elseif strcmpi(evnt5.Key,'downarrow')
    y5=y5+1;
    CurrIm(y5+1:y5+h5,x5+1:x5+w5)=uint8(double(CurrIm(y5+1:y5+h5,x5+1:
        x5+w5)).*MaskSub5);
    imshow(CurrIm(y5+1:y5+h5,x5+1:x5+w5),'InitialMagnification',200);
    title('Use Arrow Buttons to Align the Images. Press Enter When Done
        !')
    %           imshow(CurrIm);
elseif strcmpi(evnt5.Key,'return')
    answer = questdlg('Do You Want to Include It (Click No if You
        Cannot Align It)?','Is the Point Useful?','Yes','No','Yes');
    switch answer
        case 'Yes'
            Use5=1;
        case 'No'
            Use5=0;
    end
    xlswrite([rout,'\GrainAlignment','\Location5.xlsx'],[{'ImX';'ImY';'
        ImW';'ImH';'MaskX';'MaskY';'MaskW';'MaskH';'Use'}, num2cell([x5;
         y5; w5; h5;FixedRegion5';Use5])]);
    hh = msgbox('Location 5 Alignment Done. Close the Figure and
        Proceed to the Next!');
end
end

function KeyPressCb6(~,evnt6)
global x6
global y6
global w6
global h6
global rout
```

```
global RawIm
global MaskSub6
global FixedRegion6

fprintf('key pressed: %s\n',evnt6.Key);
CurrIm=RawIm;

if strcmpi(evnt6.Key,'leftarrow')
    x6=x6-1;
    CurrIm(y6+1:y6+h6,x6+1:x6+w6)=uint8(double(CurrIm(y6+1:y6+h6,x6+1:
        x6+w6)).*MaskSub6);
    imshow(CurrIm(y6+1:y6+h6,x6+1:x6+w6),'InitialMagnification',200);
    title('Use Arrow Buttons to Align the Images. Press Enter When Done
        !')
    %           imshow(CurrIm);
elseif strcmpi(evnt6.Key,'rightarrow')
    x6=x6+1;
    CurrIm(y6+1:y6+h6,x6+1:x6+w6)=uint8(double(CurrIm(y6+1:y6+h6,x6+1:
        x6+w6)).*MaskSub6);
    imshow(CurrIm(y6+1:y6+h6,x6+1:x6+w6),'InitialMagnification',200);
    title('Use Arrow Buttons to Align the Images. Press Enter When Done
        !')
    %           imshow(CurrIm);
elseif strcmpi(evnt6.Key,'uparrow')
    y6=y6-1;
    CurrIm(y6+1:y6+h6,x6+1:x6+w6)=uint8(double(CurrIm(y6+1:y6+h6,x6+1:
        x6+w6)).*MaskSub6);
    imshow(CurrIm(y6+1:y6+h6,x6+1:x6+w6),'InitialMagnification',200);
    title('Use Arrow Buttons to Align the Images. Press Enter When Done
        !')
    %           imshow(CurrIm);
elseif strcmpi(evnt6.Key,'downarrow')
    y6=y6+1;
    CurrIm(y6+1:y6+h6,x6+1:x6+w6)=uint8(double(CurrIm(y6+1:y6+h6,x6+1:
        x6+w6)).*MaskSub6);
    imshow(CurrIm(y6+1:y6+h6,x6+1:x6+w6),'InitialMagnification',200);
    title('Use Arrow Buttons to Align the Images. Press Enter When Done
        !')
    %           imshow(CurrIm);
elseif strcmpi(evnt6.Key,'return')
    answer = questdlg('Do You Want to Include It (Click No if You
        Cannot Align It)?','Is the Point Useful?','Yes','No','Yes');
    switch answer
        case 'Yes'
            Use6=1;
```

```
        case 'No'
            Use6=0;
    end
    xlswrite([rout,'\GrainAlignment','\Location6.xlsx'],[{'ImX';'ImY';'
        ImW';'ImH';'MaskX';'MaskY';'MaskW';'MaskH';'Use'}, num2cell([x6;
         y6; w6; h6;FixedRegion6';Use6])]);
    hh = msgbox('Location 6 Alignment Done. Close the Figure and
        Proceed to the Next!');
end
end

function KeyPressCb7(~,evnt7)
global x7
global y7
global w7
global h7
global rout
global RawIm
global MaskSub7
global FixedRegion7
fprintf('key pressed: %s\n',evnt7.Key);
CurrIm=RawIm;

if strcmpi(evnt7.Key,'leftarrow')
    x7=x7-1;
    CurrIm(y7+1:y7+h7,x7+1:x7+w7)=uint8(double(CurrIm(y7+1:y7+h7,x7+1:
        x7+w7)).*MaskSub7);
    imshow(CurrIm(y7+1:y7+h7,x7+1:x7+w7),'InitialMagnification',200);
    title('Use Arrow Buttons to Align the Images. Press Enter When Done
        !')
    %           imshow(CurrIm);
elseif strcmpi(evnt7.Key,'rightarrow')
    x7=x7+1;
    CurrIm(y7+1:y7+h7,x7+1:x7+w7)=uint8(double(CurrIm(y7+1:y7+h7,x7+1:
        x7+w7)).*MaskSub7);
    imshow(CurrIm(y7+1:y7+h7,x7+1:x7+w7),'InitialMagnification',200);
    title('Use Arrow Buttons to Align the Images. Press Enter When Done
        !')
    %           imshow(CurrIm);
elseif strcmpi(evnt7.Key,'uparrow')
    y7=y7-1;
    CurrIm(y7+1:y7+h7,x7+1:x7+w7)=uint8(double(CurrIm(y7+1:y7+h7,x7+1:
        x7+w7)).*MaskSub7);
    imshow(CurrIm(y7+1:y7+h7,x7+1:x7+w7),'InitialMagnification',200);
    title('Use Arrow Buttons to Align the Images. Press Enter When Done
```

```
        !')
    %           imshow(CurrIm);
elseif strcmpi(evnt7.Key,'downarrow')
    y7=y7+1;
    CurrIm(y7+1:y7+h7,x7+1:x7+w7)=uint8(double(CurrIm(y7+1:y7+h7,x7+1:
        x7+w7)).*MaskSub7);
    imshow(CurrIm(y7+1:y7+h7,x7+1:x7+w7),'InitialMagnification',200);
    title('Use␣Arrow␣Buttons␣to␣Align␣the␣Images.␣Press␣Enter␣When␣Done
        !')
    %           imshow(CurrIm);
elseif strcmpi(evnt7.Key,'return')
    answer = questdlg('Do␣You␣Want␣to␣Include␣It␣(Click␣No␣if␣You␣
        Cannot␣Align␣It)?','Is␣the␣Point␣Useful?','Yes','No','Yes');
    switch answer
        case 'Yes'
            Use7=1;
        case 'No'
            Use7=0;
    end
    xlswrite([rout,'\GrainAlignment','\Location7.xlsx'],[{'ImX';'ImY';'
        ImW';'ImH';'MaskX';'MaskY';'MaskW';'MaskH';'Use'}, num2cell([x7;
         y7; w7; h7;FixedRegion7';Use7])]);
    hh = msgbox('Location␣7␣Alignment␣Done.␣Close␣the␣Figure␣and␣
        Proceed␣to␣the␣Next!');
end
end

function KeyPressCb8(~,evnt8)
global x8
global y8
global w8
global h8
global rout
global RawIm
global MaskSub8
global FixedRegion8
fprintf('key␣pressed:␣%s\n',evnt8.Key);
CurrIm=RawIm;

if strcmpi(evnt8.Key,'leftarrow')
    x8=x8-1;
    CurrIm(y8+1:y8+h8,x8+1:x8+w8)=uint8(double(CurrIm(y8+1:y8+h8,x8+1:
        x8+w8)).*MaskSub8);
    imshow(CurrIm(y8+1:y8+h8,x8+1:x8+w8),'InitialMagnification',200);
    title('Use␣Arrow␣Buttons␣to␣Align␣the␣Images.␣Press␣Enter␣When␣Done
```

```
        !')
    %           imshow(CurrIm);
elseif strcmpi(evnt8.Key,'rightarrow')
    x8=x8+1;
    CurrIm(y8+1:y8+h8,x8+1:x8+w8)=uint8(double(CurrIm(y8+1:y8+h8,x8+1:
        x8+w8)).*MaskSub8);
    imshow(CurrIm(y8+1:y8+h8,x8+1:x8+w8),'InitialMagnification',200);
    title('Use Arrow Buttons to Align the Images. Press Enter When Done
        !')
    %           imshow(CurrIm);
elseif strcmpi(evnt8.Key,'uparrow')
    y8=y8-1;
    CurrIm(y8+1:y8+h8,x8+1:x8+w8)=uint8(double(CurrIm(y8+1:y8+h8,x8+1:
        x8+w8)).*MaskSub8);
    imshow(CurrIm(y8+1:y8+h8,x8+1:x8+w8),'InitialMagnification',200);
    title('Use Arrow Buttons to Align the Images. Press Enter When Done
        !')
    %           imshow(CurrIm);
elseif strcmpi(evnt8.Key,'downarrow')
    y8=y8+1;
    CurrIm(y8+1:y8+h8,x8+1:x8+w8)=uint8(double(CurrIm(y8+1:y8+h8,x8+1:
        x8+w8)).*MaskSub8);
    imshow(CurrIm(y8+1:y8+h8,x8+1:x8+w8),'InitialMagnification',200);
    title('Use Arrow Buttons to Align the Images. Press Enter When Done
        !')
    %           imshow(CurrIm);
elseif strcmpi(evnt8.Key,'return')
    answer = questdlg('Do You Want to Include It (Click No if You
        Cannot Align It)?','Is the Point Useful?','Yes','No','Yes');
    switch answer
        case 'Yes'
            Use8=1;
        case 'No'
            Use8=0;
    end
    xlswrite([rout,'\GrainAlignment','\Location8.xlsx'],[{'ImX';'ImY';'
        ImW';'ImH';'MaskX';'MaskY';'MaskW';'MaskH';'Use'}, num2cell([x8;
         y8; w8; h8;FixedRegion8';Use8])]);
    hh = msgbox('Location 8 Alignment Done. Close the Figure and
        Proceed to the Next!');
end
end

function KeyPressCb9(~,evnt9)
global x9
```

```
global y9
global w9
global h9
global rout
global RawIm
global MaskSub9
global FixedRegion9
fprintf('key pressed: %s\n',evnt9.Key);
CurrIm=RawIm;

if strcmpi(evnt9.Key,'leftarrow')
    x9=x9-1;
    CurrIm(y9+1:y9+h9,x9+1:x9+w9)=uint8(double(CurrIm(y9+1:y9+h9,x9+1:
        x9+w9)).*MaskSub9);
    imshow(CurrIm(y9+1:y9+h9,x9+1:x9+w9),'InitialMagnification',200);
    title('Use Arrow Buttons to Align the Images. Press Enter When Done
        !')
    %           imshow(CurrIm);
elseif strcmpi(evnt9.Key,'rightarrow')
    x9=x9+1;
    CurrIm(y9+1:y9+h9,x9+1:x9+w9)=uint8(double(CurrIm(y9+1:y9+h9,x9+1:
        x9+w9)).*MaskSub9);
    imshow(CurrIm(y9+1:y9+h9,x9+1:x9+w9),'InitialMagnification',200);
    title('Use Arrow Buttons to Align the Images. Press Enter When Done
        !')
    %           imshow(CurrIm);
elseif strcmpi(evnt9.Key,'uparrow')
    y9=y9-1;
    CurrIm(y9+1:y9+h9,x9+1:x9+w9)=uint8(double(CurrIm(y9+1:y9+h9,x9+1:
        x9+w9)).*MaskSub9);
    imshow(CurrIm(y9+1:y9+h9,x9+1:x9+w9),'InitialMagnification',200);
    title('Use Arrow Buttons to Align the Images. Press Enter When Done
        !')
    %           imshow(CurrIm);
elseif strcmpi(evnt9.Key,'downarrow')
    y9=y9+1;
    CurrIm(y9+1:y9+h9,x9+1:x9+w9)=uint8(double(CurrIm(y9+1:y9+h9,x9+1:
        x9+w9)).*MaskSub9);
    imshow(CurrIm(y9+1:y9+h9,x9+1:x9+w9),'InitialMagnification',200);
    title('Use Arrow Buttons to Align the Images. Press Enter When Done
        !')
    %           imshow(CurrIm);
elseif strcmpi(evnt9.Key,'return')
    answer = questdlg('Do You Want to Include It (Click No if You
        Cannot Align It)?','Is the Point Useful?','Yes','No','Yes');
```

```
    switch answer
        case 'Yes'
            Use9=1;
        case 'No'
            Use9=0;
    end
    xlswrite([rout,'\GrainAlignment','\Location9.xlsx'],[{'ImX';'ImY';'
        ImW';'ImH';'MaskX';'MaskY';'MaskW';'MaskH';'Use'}, num2cell([x9;
         y9; w9; h9;FixedRegion9';Use9])]);
    hh = msgbox('Location 9 Alignment Done. Close the Figure and
        Proceed to the Next!');
end
end
```

MATLAB code to determine illuminaion profile frame

```
[case_num,cases]=xlsread('file Path\Cases.xlsx');
CaseTot=length(cases);
CaseStart=1;
CaseEnd=CaseTot;

PreFactor1=0.7;
PreFactor=0.25;

for CaseNum=1:3

    case_no=cases{CaseNum};
    [TifLoc, TifPrefix, Rout, FrameInfo, FixedRegions, MovingRegions,
        MaskLoc] = CaseAndParameter( case_no );


    N_0=FrameInfo(1);
    FrameRef=FrameInfo(2);
    N_end=FrameInfo(3);

    %%
    [s]=mkdir(Rout,'\Intensity-Noise');
    [CurrIm]=imread([TifLoc,'\',TifPrefix, num2str(FrameRef),'.tif']);

    [SizeY,SizeX]=size(CurrIm);

    X=1:SizeX;
    Y=1:SizeY;

    ImgMin=min(min(double(CurrIm)));
```

```
ImgMax=max(max(double(CurrIm)));

figure(1), imshow(uint8(double(CurrIm)*255/mean(max(CurrIm))));

title('Original Image');
pause(0.1);

CurrIm=double(CurrIm);
CurrIm=medfilt2(CurrIm,[5,5]);
disp(case_no);

MinThresh=mean(min(double(CurrIm)));
MaxThresh=mean(max(double(CurrIm)));

PreThresh1=floor(MinThresh+(MaxThresh-MinThresh)*PreFactor1);
CurrIm=medfilt2(CurrIm,[5,5]);
Grain=find(CurrIm>(PreThresh1));
CurrIm(Grain)=NaN;

MinThresh=mean(min(double(CurrIm)));
MaxThresh=mean(max(double(CurrIm)));
PreThresh=floor(MinThresh+(MaxThresh-MinThresh)*PreFactor);
bkg=find(CurrIm<(PreThresh));

CurrBkg=zeros(size(CurrIm))*NaN;
CurrBkg(bkg)=CurrIm(bkg);

CurrIm(bkg)=NaN;
figure(2), imshow(uint8(CurrIm*255/mean(max(CurrIm))));

title([case_no,': Thresholded, prethresh=', num2str(PreThresh)]);
pause(0.1);

imwrite(uint8(CurrIm),[Rout,'\Intensity-Noise\',num2str(case_no),'_
    ',num2str(FrameRef),'_PreThresh=',num2str(PreThresh),'
    _thresholded.tif']);

figure(3), imshow(uint8(CurrBkg));
title([case_no,': Background']);
pause(0.1);
imwrite(uint8(CurrBkg),[Rout,'\Intensity-Noise\',num2str(case_no),'
    _',num2str(FrameRef),'_PreThresh=',num2str(PreThresh),'
    _background.tif']);

%get local maximum
```

```
%%
win_x_init=100;
win_y_init=100;

n_x=floor(SizeX/win_x_init);
n_y=floor(SizeY/win_y_init);

int_z=zeros(n_y,n_x);
int_bkg=zeros(n_y,n_x);

xx=linspace(1,SizeX,n_x);
yy=linspace(1,SizeY,n_y);
[int_x,int_y]=meshgrid(xx,yy);

xx_ext=zeros(1,n_x+2);
yy_ext=zeros(1,n_y+2);

xx_ext(2:end-1)=xx;
yy_ext(2:end-1)=yy;
xx_ext(1)=1;
xx_ext(end)=xx_ext(end-1);
yy_ext(1)=1;
yy_ext(end)=yy_ext(end-1);

%%
for i=1:n_x
    for j=1:n_y
        win_bkg=double(CurrBkg(round((yy_ext(j+1)+yy_ext(j))/2):
            round((yy_ext(j+1)+yy_ext(j+2))/2),round((xx_ext(i+1)+
            xx_ext(i))/2):round((xx_ext(i+1)+xx_ext(i+2))/2)));
        int_bkg(j,i)=mean(win_bkg(:),'omitnan');
    end
end

Nzero=find(int_bkg==0);
int_bkg(Nzero)=NaN;

ImgBkg=mean(int_bkg(:),'omitnan');

for i=1:n_x
    for j=1:n_y
        win=double(CurrIm(round((yy_ext(j+1)+yy_ext(j))/2):round((
            yy_ext(j+1)+yy_ext(j+2))/2),round((xx_ext(i+1)+xx_ext(i)
            )/2):round((xx_ext(i+1)+xx_ext(i+2))/2)));
        win_max=max(max(win));
```

```
            int_z(j,i)=win_max

            if win_max<PreThresh
                int_z(j,i)=NaN;
            end

        end
    end

    figure(4),surf(int_x,int_y,int_z,'EdgeColor','none');
    title([case_no,': Intensity Profile Original']);
    pause(3);

    [int_bkg,int_bkg]=naninterp2(int_bkg,int_bkg);
    [int_z,int_z]=naninterp2(int_z,int_z);

    %%
    npass=5;
    for i=1:npass
        int_z=medfilt2(int_z,[5,5],'symmetric');
        int_bkg=medfilt2(int_bkg,[5,5],'symmetric');
    end
    figure(5),surf(int_x,int_y,int_z,'EdgeColor','none');
    title([case_no,': Intensity Profile Smoothed']);
    pause(3);

    [X,Y] = meshgrid(X,Y);
    int_pro=interp2(int_x,int_y,int_z,X,Y,'cubic');

    bkg_pro=interp2(int_x,int_y,int_bkg,X,Y,'cubic');

    figure(6),surf(X,Y,int_pro,'EdgeColor','none');
    title([case_no,': Intensity Profile Interpolated']);
    pause(3);

    figure(7),surf(X,Y,bkg_pro,'EdgeColor','none');
    title([case_no,': Background Profile Interpolated']);

    imwrite(uint16(int_pro),[Rout,'\Intensity-Noise\',num2str(case_no),
        '_',num2str(FrameRef),'_PreThresh=',num2str(PreThresh),'
        _intensity.tif']);
    imwrite(uint16(bkg_pro),[Rout,'\Intensity-Noise\',num2str(case_no),
        '_',num2str(FrameRef),'_PreThresh=',num2str(PreThresh),'_noise.
        tif']);
```

```
    xlswrite([Rout,'\Intensity-Noise\Note.xlsx',],{[TifLoc,'\',
        TifPrefix,'.tif']; Rout; PreFactor; MinThresh; MaxThresh;
        PreThresh});

    close all;
end
```

MATLAB code to determine optimal illumination

```
Rin='file path\Raw Data';
[case_num,cases]=xlsread([Rin,'\Cases.xlsx']);
CaseTot=length(cases);
CaseStart=1;
CaseEnd=CaseTot;

for CaseNum=1:3
    case_no=cases{CaseNum};
    [TifLoc, TifPrefix, Rout, FrameInfo, FixedRegions, MovingRegions,
        MaskLoc] = CaseAndParameter( case_no );
    %%
    N_0=FrameInfo(1);
    FrameRef=FrameInfo(2);
    N_end=FrameInfo(3);

    PoreMask=imread(MaskLoc);
    PoreMask=imbinarize(PoreMask);


    GrainIndexOriginal=find(~PoreMask); %indices of grains
    PoreMask=ImEro(PoreMask,'cross',5); %make the mask 5 pixels large,
        corresponding roughly to the thickness of the film


    PoreIndex=find(PoreMask); %indices of pore spaces
    GrainIndex=find(~PoreMask); %indices of grains
    MaskEdge=bwmorph(~PoreMask,'remove'); %edge of grains
   [SizeY, SizeX]=size(PoreMask);


    [NoteNum,NoteText]=xlsread([Rout,'\Intensity-Noise\Note.xlsx',]);
    PreThresh=NoteNum(4);

    InterpMethod='linear';
    [Reference1,Reference1Text]=xlsread([Rout,'\GrainAlignment','\
        Location1.xlsx']);
```

```
[Reference2,Reference2Text]=xlsread([Rout,'\GrainAlignment','\
    Location2.xlsx']);
[Reference3,Reference3Text]=xlsread([Rout,'\GrainAlignment','\
    Location3.xlsx']);
[Reference4,Reference4Text]=xlsread([Rout,'\GrainAlignment','\
    Location4.xlsx']);
[Reference5,Reference5Text]=xlsread([Rout,'\GrainAlignment','\
    Location5.xlsx']);
[Reference6,Reference6Text]=xlsread([Rout,'\GrainAlignment','\
    Location6.xlsx']);
[Reference7,Reference7Text]=xlsread([Rout,'\GrainAlignment','\
    Location7.xlsx']);
[Reference8,Reference8Text]=xlsread([Rout,'\GrainAlignment','\
    Location8.xlsx']);
[Reference9,Reference9Text]=xlsread([Rout,'\GrainAlignment','\
    Location9.xlsx']);

Intensity=imread([Rout,'\Intensity-Noise\',num2str(case_no),'_',
    num2str(FrameRef),'_PreThresh=',num2str(PreThresh),'_intensity.
    tif']);
Background=imread([Rout,'\Intensity-Noise\',num2str(case_no),'_',
    num2str(FrameRef),'_PreThresh=',num2str(PreThresh),'_noise.tif'
    ]);

%apply image transformation to correct Intensity image
IntensityCorrected = AlignGrainsTransform(Intensity,PoreMask,
    InterpMethod, Reference1, Reference2, Reference3, Reference4,
    Reference5, Reference6, Reference7, Reference8, Reference9);
%apply image transformation to correct Background image
BackgroundCorrected = AlignGrainsTransform(Background,PoreMask,
    InterpMethod, Reference1, Reference2, Reference3, Reference4,
    Reference5, Reference6, Reference7, Reference8, Reference9);

[CurrIm]=imread([TifLoc,'\',TifPrefix, num2str(FrameRef),'.tif']);
CurrIm = AlignGrainsTransform(CurrIm,PoreMask,InterpMethod,
    Reference1, Reference2, Reference3, Reference4, Reference5,
    Reference6, Reference7, Reference8, Reference9);

CurrIm = medfilt2(CurrIm,[3,3]);
CurrIm(GrainIndexOriginal)=0;
[s]=mkdir(Rout,'\OptimalLevel');

LevelFlag=1;
Level=0; %Initial guess of Level
Count=0;
```

```
while LevelFlag
    Threshold=(double(IntensityCorrected)-double(
        BackgroundCorrected))*Level+double(BackgroundCorrected);
    Threshold(913,1189)
    %%%%%%%%%%%%%%%%%%%%%%%%%%%%%%%%%%%%%%%%%%%%%%%%%%%%%%%%%%%%%%%%%%%%%%%%
    Count=Count+1;
    ImDiff=double(CurrIm)-Threshold;
    NegativeIndex=find(ImDiff<0);
    ImDiff(NegativeIndex)=NaN;
    NWPhase=~isnan(ImDiff);

    NWPhaseEdge=bwmorph(NWPhase,'remove'); %edge of grains

    NWPhaseIndex=find(NWPhase);
    Sat(Count)=length(NWPhaseIndex)/length(PoreIndex);
    AllLevel(Count)=Level;

    %%%%%%%%%%%%%%%%%%%%%%%%%%%%%%%%%%%%
    red=false(SizeY, SizeX);
    blue=false(SizeY, SizeX);

    blue(GrainIndex)=true;
    red(PoreIndex)=true;
    green=NWPhase;

    yellow_index=find(red.*green);
    cyan_index=find(blue.*green);

    blue(cyan_index)=false; % blue is grain, green is air, red is
        water
    red(yellow_index)=false;
    green(yellow_index)=false;

    GreenIndex=find(green);
    NWIndex=find(NWPhase);

    CG_overlap(Count)=length(GreenIndex)/length(NWIndex);
    rgbImage = cat(3, uint8(double(red)*255), uint8(double(green)
        *255), uint8(double(blue)*255));

    figure(1);
    subplot(1,1,1);
    imshow(rgbImage);
    title([case_no,': ','Frame = ',num2str(FrameRef), ', Level=',
```

```
            num2str(Level), ', CG=', num2str(CG_overlap(Count)), ', Sat=
            ', num2str(Sat(Count))]);
        clear ImDiff;

        pause(0.01);

%         if CG_overlap(Count)>0.1
              if CG_overlap(Count)>0.05
            Level=Level+0.005;
        else
            LevelFlag=0;
        end
    end

    red_write=NWPhase;
    green_write=NWPhase;
    blue_write=NWPhase;

    N_edge=find(MaskEdge);
    red_write(N_edge)=true;
    green_write(N_edge)=false;
    blue_write(N_edge)=false;

    rgbImage_write = cat(3, uint8(double(red_write)*255), uint8(double(
        green_write)*255), uint8(double(blue_write)*255));
    rgbImage_write(:,1:end,:)=rgbImage_write(:,end:-1:1,:);

    imwrite(rgbImage_write,[Rout,'\OptimalLevel\Frame_',num2str(
        FrameRef),'_Level_',num2str(Level*1000),'_1.tif']);
    imwrite(rgbImage,[Rout,'\OptimalLevel\Frame_',num2str(FrameRef),'
        _Level_',num2str(Level*1000),'_2.tif']);


    CASENUM(CaseNum)=CaseNum;
    LEVEL(CaseNum)=Level;
    SAT(CaseNum)=Sat(Count);
    CGOVERLAP(CaseNum)=CG_overlap(Count);
    FRAMENO(CaseNum)=FrameRef;
    PRETHRESH(CaseNum)=PreThresh;
    clear Level CG_overlap Sat;
end

xlswrite([Rin,'\','Level.xlsx'],[CASENUM',FRAMENO',LEVEL',SAT',
    CGOVERLAP',PRETHRESH']);
```

MATLAB code to differentiate wetting and non-wetting phase

```
Rin='Ffile path\Raw Data';
[case_num,cases]=xlsread([Rin,'\Cases.xlsx']);
CaseTot=length(cases);
CaseStart=1;
CaseEnd=CaseTot;

[AllLevel,Level_text]=xlsread([Rin,'\Level.xlsx']);
AllLevel=AllLevel(:,3);

answer = questdlg('Do you want to average the sequence before
    segmentation?','Average or Individual?','Average','Individual','
    Individual');
%perform image segmentation for the average of the image sequence, only
     one binary image will be output.
%set to 0 to perform image segmentation for indivdial images

Show=1; %set Show to 1 to show intermediate images. Turn it off for
    fast processing.

for CaseNum=1:3
    case_no=cases{CaseNum};
    disp(['================ ',case_no,' ================']);
    [TifLoc, TifPrefix, Rout, FrameInfo, FixedRegions, MovingRegions,
        MaskLoc] = CaseAndParameter( case_no );

    N0=FrameInfo(1);
    FrameRef=FrameInfo(2);
    NEnd=FrameInfo(3);
    Level=AllLevel(CaseNum);
    PoreMask=imread(MaskLoc);
    PoreMask=imbinarize(PoreMask);
    PoreIndex=find(PoreMask); %indices of pore spaces
    GrainIndex=find(~PoreMask); %indices of grains
    MaskEdge=bwmorph(~PoreMask,'remove'); %edge of grains
    [SizeY, SizeX]=size(PoreMask);

    [NoteNum,NoteText]=xlsread([Rout,'\Intensity-Noise\Note.xlsx',]);
    PreThresh=NoteNum(4);

    InterpMethod='linear';
    [Reference1,Reference1Text]=xlsread([Rout,'\GrainAlignment','\
        Location1.xlsx']);
    [Reference2,Reference2Text]=xlsread([Rout,'\GrainAlignment','\
        Location2.xlsx']);
    [Reference3,Reference3Text]=xlsread([Rout,'\GrainAlignment','\
```

```
    Location3.xlsx']);
[Reference4,Reference4Text]=xlsread([Rout,'\GrainAlignment','\
    Location4.xlsx']);
[Reference5,Reference5Text]=xlsread([Rout,'\GrainAlignment','\
    Location5.xlsx']);
[Reference6,Reference6Text]=xlsread([Rout,'\GrainAlignment','\
    Location6.xlsx']);
[Reference7,Reference7Text]=xlsread([Rout,'\GrainAlignment','\
    Location7.xlsx']);
[Reference8,Reference8Text]=xlsread([Rout,'\GrainAlignment','\
    Location8.xlsx']);
[Reference9,Reference9Text]=xlsread([Rout,'\GrainAlignment','\
    Location9.xlsx']);

Intensity=imread([Rout,'\Intensity-Noise\',num2str(case_no),'_',
    num2str(FrameRef),'_PreThresh=',num2str(PreThresh),'_intensity.
    tif']);
Background=imread([Rout,'\Intensity-Noise\',num2str(case_no),'_',
    num2str(FrameRef),'_PreThresh=',num2str(PreThresh),'_noise.tif'
    ]);

%apply image transformation to correct Intensity image
IntensityCorrected = AlignGrainsTransform(Intensity,PoreMask,
    InterpMethod, Reference1, Reference2, Reference3, Reference4,
    Reference5, Reference6, Reference7, Reference8, Reference9);
%apply image transformation to correct Background image
BackgroundCorrected = AlignGrainsTransform(Background,PoreMask,
    InterpMethod, Reference1, Reference2, Reference3, Reference4,
    Reference5, Reference6, Reference7, Reference8, Reference9);

Threshold=(double(IntensityCorrected)-double(BackgroundCorrected))*
    Level+double(BackgroundCorrected);
[s]=mkdir([Rout,'\NWPhase_',num2str(N0),'-',num2str(NEnd)]);

switch answer
    case 'Average'
        [s]=mkdir([Rout,'\NWPhase_',num2str(N0),'-',num2str(NEnd),'
            \Average']);
        Count=0;
        ImSum=zeros(size(Intensity));
        for i=N0:1:NEnd
            Count=Count+1;
            CurrIm=imread([TifLoc,'\',TifPrefix, num2str(i),'.tif'
                ]);
            ImSum=ImSum+double(CurrIm);
```

```
            disp(['Image#', num2str(i),'/',num2str(NEnd)]);
        end
        ImAverage = ImSum/Count;
        ImAverage = AlignGrainsTransform(ImAverage,PoreMask,
            InterpMethod, Reference1, Reference2, Reference3,
            Reference4, Reference5, Reference6, Reference7,
            Reference8, Reference9);
        ImAverage = medfilt2(ImAverage,[5,5]);
        ImDiff = double(ImAverage)-Threshold;

        NegativeIndex=find(ImDiff<0);
        ImDiff(NegativeIndex)=NaN;
        WaterPhase=~isnan(ImDiff);
        WaterGrain=WaterPhase;
        WaterGrain(GrainIndex)=true;
        NWPhase=~WaterGrain;
        NWPhase=bwareaopen(NWPhase,5000);
        WaterGrain=~NWPhase;
        [WaterGrain]=ImDia(WaterGrain,'cross',3);
        NWPhase=~WaterGrain;
        NWPhase=bwareaopen(NWPhase,5000);

        WaterGrain=~NWPhase;
        WaterGrain=ImEro(WaterGrain,'cross',3);

        WaterPhase=WaterGrain;
        WaterPhase(GrainIndex)=false;


        WaterPhase=bwareaopen(WaterPhase,400); %remove anything
            that is smaller than 400 pixels
        NWPhase=~WaterPhase;
        NWPhase(GrainIndex)=false;

        imwrite(NWPhase,[Rout,'\NWPhaseHT_',num2str(N0),'-',num2str
            (NEnd),'\Average\Average_',num2str(N0),'_',num2str(N0),'
            _Level_',num2str(Level*1000),'.tif']);

    case 'Individual'
        [s]=mkdir([Rout,'\NWPhase_',num2str(N0),'-',num2str(NEnd),'
            \Individual']);
        Count=0;
        for i=N0:1:NEnd
            Count=Count+1;
            CurrIm=imread([TifLoc,'\',TifPrefix, num2str(i),'.tif'
```

```
    ]);
if Show
    figure(1),imshow(uint8(double(CurrIm)*255/mean(max(
        CurrIm)))));
end
CurrIm = AlignGrainsTransform(CurrIm,PoreMask,
    InterpMethod, Reference1, Reference2, Reference3,
    Reference4, Reference5, Reference6, Reference7,
    Reference8, Reference9);
for ii=1:1
    CurrIm = medfilt2(CurrIm,[5,5]);
    if Show
        figure(ii+10), imshow(uint8(double(CurrIm)*255/
            mean(max(CurrIm)))));
    end
end

if Show
    figure(2), imshow(uint8(double(CurrIm)*255/mean(max
        (CurrIm)))));
end

ImDiff = double(CurrIm)-Threshold;

NegativeIndex=find(ImDiff<0);
ImDiff(NegativeIndex)=NaN;
WaterPhase=isnan(ImDiff);
if Show
    figure(3), imshow(WaterPhase)
end

WaterGrain=WaterPhase;
WaterGrain(GrainIndex)=true;
NWPhase=~WaterGrain;

if Show
    figure(4), imshow(NWPhase)
end

NWPhase=bwareaopen(NWPhase,100);
%                   WaterGrain=~NWPhase;
%                   [WaterGrain]=ImDia(WaterGrain,'cross
    ',3);
%                   NWPhase=~WaterGrain;
%                   NWPhase=bwareaopen(NWPhase,100);
```

```
                %
                %                       WaterGrain=~NWPhase;
                %                       WaterGrain=ImEro(WaterGrain,'cross
                    ',3);

                WaterPhase=~NWPhase;
                WaterPhase(GrainIndex)=false;
                WaterPhase=bwareaopen(WaterPhase,400); %remove anything
                     that is smaller than 400 pixels
                NWPhase=~WaterPhase;
                NWPhase(GrainIndex)=false;
                if Show
                    figure(5), imshow(NWPhase)

                    hold on
                    b = bwboundaries(PoreMask);
                    for k = 1:numel(b)
                        plot(b{k}(:,2), b{k}(:,1), 'r', 'Linewidth',
                            0.3)
                    end
                end
                if Show
                    hold off
                end
                %                       pause(1);
                imwrite(NWPhase,[Rout,'\NWPhase_',num2str(N0),'-',
                    num2str(NEnd),'\Individual\Frame_',num2str(i),'
                    _Level_',num2str(Level*1000),'.tif']);
                disp(['Image#', num2str(i),'/',num2str(NEnd)]);

                NWPhaseMask=NWPhase;
                NWPhaseMask(MaskEdge)=true;
            end
        end
    end
```

MATLAB code to determine saturation and saturation distribution

```
Rin='file path\Raw Data';
[case_num,cases]=xlsread([Rin,'\Cases.xlsx']);
CaseTot=length(cases);
case_start=1;
CaseEnd=CaseTot;
[AllLevel,Level_text]=xlsread([Rin,'\Level.xlsx']);
AllLevel=AllLevel(:,3);
```

```
answer = questdlg('Do you want to average the sequence before
    segmentation?','Average or Individual?','Average','Individual','
    Individual');
%perform image segmentation for the average of the image sequence, only
     one binary image will be output.
%set to 0 to perform image segmentation for indivdial images

Show=1; %whether or not display some intemediate results

for CaseNum=1:3
    case_no=cases{CaseNum};
    disp(['================ ',case_no,' ================']);
    [TifLoc, TifPrefix, Rout, FrameInfo, FixedRegions, MovingRegions,
        MaskLoc] = CaseAndParameter( case_no );

    N0=FrameInfo(1);
    FrameRef=FrameInfo(2);
    NEnd=FrameInfo(3);
    FrameRate=FrameInfo(4);
    Level=AllLevel(CaseNum);

    PoreMask=imread(MaskLoc);
    PoreMask=imbinarize(PoreMask);
    GrainMask=~PoreMask;
    PoreIndex=find(PoreMask); %indices of pore spaces
    GrainIndex=find(GrainMask); %indices of grains
    MaskEdge=bwmorph(~PoreMask,'remove'); %edge of grains
    [SizeY, SizeX]=size(PoreMask);
    Porosity=sum(sum(double(PoreMask)))/(SizeX*SizeY);
    %%
    switch answer
        case 'Average'
            [s1]=mkdir(Rout,'\Sat-Anw-An-LeadPos');
            [s2]=mkdir(Rout,'\Sat-Anw-An-LeadPos\Average');
            [s3]=mkdir(Rout,'\Sat-Anw-An-LeadPos\Average\Meni-
                Coordinates');
            NWPhase=imread([Rout,'\NWPhase_',num2str(N0),'-',num2str(
                NEnd),'\Average\Average_',num2str(N0),'_',num2str(N0),'
                _Level_',num2str(Level*1000),'.tif']);
            %%%%%%%%%%%%%%%%%%%%%%%%%%%%%%%%%%%%%%%%%%%%%%%%%%%%%%%%%%%%
            %%Find AnPixel%%%%%%%%%%%%%%%%%%%%%%%%%%%%%%%%%%%%%%%%%%%%%%
            %%%%%%%%%%%%%%%%%%%%%%%%%%%%%%%%%%%%%%%%%%%%%%%%%%%%%%%%%%%%
            NWEdge=bwmorph(NWPhase,'remove');
            AnPixel=sum(sum(double(NWEdge)));
```

```
%%%%%%%%%%%%%%%%%%%%%%%%%%%%%%%%%%%%%%%%%%%%%%%%%%%%%%%%%%%%%%%%%%%%%%%%%%%%
%%Leading Figure Position%%%%%%%%%%%%%%%%%%%%%%%%%%%%%%%%%%%%%%%%%%%%%%%%%%%
%%%%%%%%%%%%%%%%%%%%%%%%%%%%%%%%%%%%%%%%%%%%%%%%%%%%%%%%%%%%%%%%%%%%%%%%%%%%
NWIndex=find(NWPhase);
NWAvgV=sum(double(NWPhase),1);
[NWRow, NWCol]=find(NWAvgV>3);

if ~isempty(NWCol)
    LeadPosN=max(NWCol)/SizeX; %normalized by the width
end

if Show==1
    figure(1), imshow(uint8(NWPhase*255));
    title(['Averaged: ',num2str(N0),'-',num2str(NEnd)]);
    hold on;
    plot([LeadPosN, LeadPosN]*SizeX, [1, SizeY], 'y--');
    hold off;
end

%%%%%%%%%%%%%%%%%%%%%%%%%%%%%%%%%%%%%%%%%%%%%%%%%%%%%%%%%%%%%%%%%%%%%%%%%%%%
%%Saturation Calculation %%%%%%%%%%%%%%%%%%%%%%%%%%%%%%%%%%%%%%%%%%%%%%%%%%%
%%%%%%%%%%%%%%%%%%%%%%%%%%%%%%%%%%%%%%%%%%%%%%%%%%%%%%%%%%%%%%%%%%%%%%%%%%%%
Sat=sum(sum(double(NWPhase)))/sum(sum(double(PoreMask)));
Frame=0;%time and frame not defined for average case
Time=0;
pause(0.001);
%%%%%%%%%%%%%%%%%%%%%%%%%%%%%%%%%%%%%%%%%%%%%%%%%%%%%%%%%%%%%%%%%%%%%%%%%%%%
%%Anw Calculation %%%%%%%%%%%%%%%%%%%%%%%%%%%%%%%%%%%%%%%%%%%%%%%%%%%%%%%%%%
%%%%%%%%%%%%%%%%%%%%%%%%%%%%%%%%%%%%%%%%%%%%%%%%%%%%%%%%%%%%%%%%%%%%%%%%%%%%
[NWPhase]=ImDiaEro(PoreMask,NWPhase,6);
SegImg=int8(NWPhase); %CO2=1; %water = 0
SegImg(GrainIndex) = 3; %grains = 3
[FFInterf] = FindEdge(SegImg);

InterfIndex=find(FFInterf);
AnwPixel=length(InterfIndex);

[MeniLoc, MeniL] = CurveLength(FFInterf);
AnwFitted=sum(MeniL);

disp(['Case: ', case_no, ', Averaged: ',num2str(N0),'-',
    num2str(NEnd), ', Sat = ', num2str(round(Sat*1000)/1000)
    , ', LeadPos = ', num2str(LeadPosN), ', Anw = ', num2str
    (AnwFitted), ', An = ', num2str(AnPixel)]);
```

```
        red_show=double(NWPhase)*0.5;
        green_show=double(NWPhase)*0.5;
        blue_show=double(NWPhase)*0.5;

        green_show(GrainIndex)=0.2;
        red_show(GrainIndex)=0.2;
        blue_show(GrainIndex)=0.2;

        green_show(InterfIndex)=1;

        rgbImage_show = cat(3, uint8(double(red_show)*255), uint8(
            double(green_show)*255), uint8(double(blue_show)*255));

        figure(2);
        imshow(rgbImage_show);
        title(['Case:␣', case_no,':␣','Average']);

        hold on
        for k = 1:numel(MeniLoc)
            plot(MeniLoc{k}(:,3), MeniLoc{k}(:,4), 'r-', 'Linewidth
                ', 1)
        end
        pause(0.1);
        hold off
        %           saveas(gcf,[rout,'\InterLength-LeadingFinger\
            Case_',case_no,'_MaxSat_Frame-',num2str(i),'_Level_pt',
            num2str(level*1000),'_Pre-thr_',num2str(pre_thresh),'.
            fig']);
        %           print([rout,'\Sat-Anw-An-LeadPos\Case_',case_no,'
            _Check50_Frame-',num2str(Frame(count))],'-dtiff','-r600
            ');
        save([Rout,'\Sat-Anw-An-LeadPos\Average\Meni-Coordinates\
            Case_',case_no,'_',num2str(N0),'_',num2str(NEnd),'.mat'
            ],'MeniLoc');
        %       imwrite(rgbImage_show,[rout,'\Level_check=',num2str(
            level*1000),'\',num2str(i),'.tif']);
        %       imwrite(rgbImage_show_2,[rout,'\Level_check_2=',
            num2str(level*1000),'\',num2str(i),'.tif']);

    case 'Individual'
        Frame=(1:1:NEnd-N0+1)*0;
        Time=zeros(size(Frame));
        Sat=zeros(size(Frame));
        LeadPosN=zeros(size(Frame));
        AnwFitted=zeros(size(Frame));
```

```
AnwPixel=zeros(size(Frame));
AnPixel=zeros(size(Frame));

[s1]=mkdir(Rout,'\Sat-Anw-An-LeadPos');
[s2]=mkdir(Rout,'\Sat-Anw-An-LeadPos\Individual');
[s2]=mkdir(Rout,'\Sat-Anw-An-LeadPos\Individual\Meni-
    Coordinates');

DispFreq=1;
check50=1;
%%
Count=0;
for i=N0:1:N0
    Count=Count+1;
    NWPhase=imread([Rout,'\NWPhase_',num2str(N0),'-',
        num2str(NEnd),'\Individual\Frame_',num2str(i),'
        _Level_',num2str(Level*1000),'.tif']);

    %%%%%%%%%%%%%%%%%%%%%%%%%%%%%%%%%%%%%%%%%%%%%%%%%%%%%%%%%%%%
    %%Find AnPixel%%%%%%%%%%%%%%%%%%%%%%%%%%%%%%%%%%%%%%%%%%%%%
    %%%%%%%%%%%%%%%%%%%%%%%%%%%%%%%%%%%%%%%%%%%%%%%%%%%%%%%%%%%%
    NWEdge=bwmorph(NWPhase,'remove');
    AnPixel(Count)=sum(sum(double(NWEdge)));

    %%%%%%%%%%%%%%%%%%%%%%%%%%%%%%%%%%%%%%%%%%%%%%%%%%%%%%%%%%%%
    %%Leading Figure Position%%%%%%%%%%%%%%%%%%%%%%%%%%%%%%%%%%%
    %%%%%%%%%%%%%%%%%%%%%%%%%%%%%%%%%%%%%%%%%%%%%%%%%%%%%%%%%%%%
    NWIndex=find(NWPhase);
    NWAvgV=sum(double(NWPhase),1);
    [NWRow, NWCol]=find(NWAvgV>3);

    if ~isempty(NWCol)
        LeadPosN(Count)=max(NWCol)/SizeX; %normalized by
            the width
    end

    if Show==1
        figure(1), imshow(uint8(NWPhase*255));
        title(['Frame␣=␣',num2str(i)]);
        hold on;
        plot([LeadPosN(Count), LeadPosN(Count)]*SizeX, [1,
            SizeY], 'y--');
        hold off;
    end
```

```
%%%
```

```
                    green_show(InterfIndex)=1;
                    rgbImage_show = cat(3, uint8(double(red_show)*255),
                        uint8(double(green_show)*255), uint8(double(
                        blue_show)*255));

                    figure(2);
                    imshow(rgbImage_show);
                    title(['Case: ', case_no,': ','Frame = ',num2str(
                        Frame(Count)), ', Sat=', num2str(round(Sat(Count
                        )*1000)/1000), ', Anw = ', num2str(AnwFitted(
                        Count))]);

                    hold on
                    for k = 1:numel(MeniLoc)
                        plot(MeniLoc{k}(:,3), MeniLoc{k}(:,4), 'r-', '
                            Linewidth', 1)
                    end
                    pause(0.001);
                    hold off
                end

                save([Rout,'\Sat-Anw-An-LeadPos\Individual\Meni-
                    Coordinates\Case_',case_no,'Frame-',num2str(Frame(
                    Count)),'.mat'],'MeniLoc');
            end
        end
    end

Mag=2.5;
PixelSize=6.5; %um
LengthConversion=PixelSize/1000/Mag;
Q=100;% ul/min, flowrate

PoreVolume=(sum(sum(double(PoreMask))))*LengthConversion^2)*0.031; %[mm
    ^3];
PV=Time*(Q/60)/PoreVolume;
%       AnwFittedMM=AnwFitted*LengthConversion/(sum(sum(double(PoreROI)))
    *LengthConversion^2);%normalized by the total pore area and convert
    to physical unit [mm^(-1)]
%       imwrite(rgbImage_max,[rout,'\Sat_Temporal\Frame_',num2str(
    frame_max),'_Level_',num2str(level*1000),'_Sat_',num2str(round(
    Sat_max*100)),'_2.tif']);
%       imwrite(rgbImage_max_2,[rout,'\Sat_Temporal\Frame_',num2str(
    frame_max),'_Level_',num2str(level*1000),'_Sat_',num2str(round(
    Sat_max*100)),'_1.tif']);
```

```
switch answer
    case 'Average'
        xlswrite([Rout,'\Sat-Anw-An-LeadPos\Average\Case_',case_no,'
           _Average(',num2str(N0),'-',num2str(NEnd),').xlsx'],[{'Frame'
           ,'Time','PV','Sat','LeadPosN','An[Pixel]','Anw[Pixel]','
           AnwFitted[Pixel]'}; num2cell([Frame, Time,PV, Sat, LeadPosN,
            AnPixel, AnwPixel,AnwFitted])]);
    case 'Individual'
        xlswrite([Rout,'\Sat-Anw-An-LeadPos\Individual\Case_',case_no,'
           _Frame(',num2str(N0),'-',num2str(NEnd),').xlsx'],[{'Frame','
           Time','PV','Sat','LeadPosN','An[Pixel]','Anw[Pixel]','
           AnwFitted[Pixel]'}; num2cell([Frame', Time',PV', Sat',
           LeadPosN', AnPixel', AnwPixel',AnwFitted'])]);
end
```